DEVELOPMENT OF A COUPLED C-N-P-O-S MODEL OF MARINE BIOGEOCHEMISTRY FOR PALEOCEANOGRAPHIC APPLICATIONS

A Thesis

Presented to the Faculty of the Graduate School

of Cornell University

In Partial Fulfillment of the Requirements for the Degree of

Master of Science

by

Stephen Justin Romaniello

May 2008

ABSTRACT

A model of marine carbon, nitrogen, phosphorus, oxygen, and sulfur biogeochemistry is developed for use on one-thousand year to multi-million year time scales. It includes simple plankton population dynamics and explicit representation of nitrogen fixation, nitrification, denitrification, anammox, and thiodenitrification. The biogeochemistry module is coupled to a new intermediate-complexity box model representation of global ocean circulation, which includes representation of high-latitude, gyre, and coastal upwelling regions. A separate version of the circulation model is developed for the Black Sea, allowing the same biogeochemistry model to be tested under anoxic conditions.

Careful validation of the of the simulated circulation and biogeochemistry for the modern Global Ocean and Black Sea was carried out using temperature, salinity, natural and bomb radiocarbon, chlorofluorocarbon, and a wide variety of tracer profiles and major biogeochemical fluxes. When coupled to an appropriate circulation model, the same biogeochemical model is capable of accurately simulating observed component profiles and fluxes in both the modern Global Ocean and Black Sea. For the Global Ocean, it is demonstrated that the new box model is capable of avoiding many of the artifacts found in simpler box model representations of ocean circulation, including excessive high-latitude sensitivity and the need to assign component-dependent eddy diffusivities.

It is anticipated that this new model will have many applications for problems linking coupled nutrient cycling and changes ocean redox. Efficient numerical integration (1 My/hour) and modular program design make it relatively easy to modify existing processes or add entirely new processes and components. A copy of model source code (in MATLAB®) is available from the author upon request.

BIOGRAPHICAL SKETCH

Stephen Romaniello was born in Hartford, Connecticut on June 5, 1983. He grew up and attended public school in Enfield, Connecticut. Stephen completed his undergraduate work at Cornell University in May 2005, earning a B.A. *magna cum laude* in the Science of Earth Systems major with a focus on biogeochemistry and chemical oceanography. At Cornell, Stephen was a graduate of the College of Arts and Sciences' College Scholar program, which allowed him additional flexibility to design a broad and intensive curriculum in the Earth Sciences.

The topic of this Master's thesis began as a discussion about the role of molybdenum in regulating rates of nitrogen fixation with Professor Robert Howarth during the fall of 2003. Professor Louis Derry recalled that the strong redox dependence of molybdenum solubility might have contributed to large changes in the nitrogen cycle over the course of Earth's biogeochemical evolution. It soon became clear that any process-based model for this theory would first require a model of ocean circulation and major element biogeochemistry applicable over long geological periods. In particular, the model would need to represent the feedbacks between ocean redox state and the biogeochemical cycles of carbon, nitrogen, phosphorus, and sulfur in especial detail. Stephen began developing such a model as undergraduate thesis project with the support Professor Derry that summer in work that would continue to grow and evolve to present.

Stephen has broad interests in the environment, earth sciences and science education. His experiences as student and teaching assistant at Cornell have highlighted the tremendous difference that a teacher's commitment to excellence can make in the classroom. Stephen is committed to propagating and disseminating this vision of academic excellence in his own career.

This work is dedicated to my parents, Ray and Laurie; my sister, Lisa; my uncle, Rick; and Helen, who have all supported my efforts, and shaped and enriched my life,

And

To my dedicated teachers, without whom, none of my efforts would have found hold.

ACKNOWLEDGMENTS

I would first like to thank Lou Derry and Andy Pershing for advising my work over the years. Lou saw the merit in this project from the outset and provided the funding and support needed to get it and me off the ground, for which I am very grateful.

This project would not have been possible without the discussion and data provided by many people. Jim Murray's group at U. Washington was instrumental in educating me about the Black Sea. John Kirkpatrick not only hosted me during a three week stay at UW and but also taught me to lay slate tile. Sergey Konovalov at the Marine Hydrophysical Institute, National Academy of Sciences of Ukraine, provided models, data, and years of experience in a system initially foreign to me.

I would like to thank L.A. Codispoti, L. Gordon, J. Morrsion, H. W. Ducklow, F. Azam, D. C. Smith and the US JGOFS Arabian Sea, AESOPS, HOT, BATS, WOCE, and the 2001 and 2003 Black Sea hydrographic teams for kindly making their hydrographic data available online. J. A. Morgan provided additional heterotrophic cell counts and microbial production data from the Black Sea. The Pacific Fisheries Environmental Laboratory provided data from which to derive Eastern Pacific coastal upwelling rates.

Finally, I would once again like to thank my family, friends, and especially Helen for providing support, motivation, understanding, companionship, and more throughout my life.

This work was partially funded by NSF grant EAR-0720192.

TABLE OF CONTENTS

LIST OF FIGURES

LIST OF TABLES

SECTION 1

OVERVIEW AND MOTIVATION

1.1 *Scientific Motivation*

Understanding the evolution of coupled biogeochemical cycles through geologic time is one of the overarching problems in the earth sciences. Since the rise of atmospheric oxygen to very low but detectable levels in earliest Proterozoic [*Canfield*, 2005; *Catling and Claire*, 2005; *Holland*, 2006], interactions between the familiar "major" biogeochemical-active elements (C, N, O, P, S) have governed marine redox cycling. In most modern environments, the basic nature of the coupling between these element cycles is now understood, although many of the details remain unclear, particularly in the nitrogen and sulfur cycles. Within the last decade, there has also been mounting progress toward determining the interactions of these major element cycles with trace metal cycles (Fe, Mn, Mo, Cu, etc.) [*Konovalov et al.*, 2005; *Moore and Doney*, 2007a; *Morel and Price*, 2003]. Given then our knowledge of modern biogeochemical processes, how can one use quantitative dynamical models to better understand their coupled evolution over Earth's past?

The primary motivation for this study is the dramatic increase in the number and quality of the new data sets from the geologic record. Many high quality records of chemical and isotopic variations in marine sediments now extend well into the Proterozoic and even the Archean [*Canfield*, 2005; *Halverson et al.*, 2005; *Hayes et al.*, 1999; *Holland*, 2006; *Isley and Abbott*, 1999; *Papineau et al.*, 2005; *Rouxel et al.*, 2005; *Scott et al.*, 2008; *Shields and Veizer*, 2002; *Strauss and Moore*, 1992]. These new datasets have prompted a large number of novel and interesting hypotheses about the nature of the processes that drive the isotopic variations observed in these ancient sediments alongside striking sedimentological features such as widespread glacial deposits, phosphorites, and iron formations [*Bartley and Kah*, 2004; *Brasier and Lindsay*,

1998; *Canfield*, 1998; *Derry et al.*, 1992; *Frank et al.*, 2003; *Hoffman et al.*, 1998; *Knoll et al.*, 1996; *Kump et al.*, 2005; *Logan et al.*, 1995; *Montanez et al.*, 2000; *Rothman et al.*, 2003; *Saltzman*, 2005; among others]. A very brief summary of some of the salient points with respect to the Proterozoic (although some apply in the Paleozoic) is:

- Atmospheric oxygen appears to have been present in sufficient quantities to maintain an oxidizing surface environment, but probably was insufficient to penetrate into the deep ocean (Stage II of [*Kasting*, 1987]). While no truly quantitative estimates are available, a range from 1 to 20% of the present atmospheric level (PAL) seems plausible. Oxygen levels are believed to have increased significantly in the late Neoproterozoic [*Canfield and Teske*, 1996; *Canfield*, 2005; *Canfield et al.*, 2007; *Catling and Claire*, 2005; *Derry et al.*, 1992; *Fike et al.*, 2006; *Holland*, 2006; *Hurtgen et al.*, 2005; *Runnegar*, 1982].
- The oceans appear to have been sulfidic at depth through at least some of this interval [*Brocks et al.*, 2005; *Canfield*, 1998; *Canfield and Raiswell*, 1999; *Canfield et al.*, 2000; *Hurtgen et al.*, 2002; *Shen et al.*, 2003]. The presence of high levels of sulfide should have limited the availability of dissolved Fe, Mo, and some other transition metals [*Arnold et al.*, 2004].
- With large areas of the ocean dys- or anoxic, high relative rates of denitrification and/or trace metal limitation of nitrogen fixation may have conspired to impose strong N limitation on marine productivity [*Falkowski*, 1997; *Fennel et al.*, 2005], with possible implications for eukaryotic diversification [*Anbar and Knoll*, 2002].
- Prior to the evolution of metazoans, particulate carbon export from the surface ocean might have been much less efficient. The oceans may have been characterized by large pools of dissolved organic carbon with less cycling via

particulate organic carbon (POC) [*Logan et al.*, 1995; *Rothman et al.*, 2003; *Shields et al.*, 1999]. The large Shuram-Wonaka $\delta^{13}C$ excursion in the Neoproterozoic has been interpreted by some workers to be evidence for a large-scale reorganization of the carbon cycle involving the oxidation of a large pool of marine DOM [*Fike et al.*, 2006]. One suggestion is that was possibly the consequence of a switch from predominantly dissolved to predominantly particulate carbon export from the surface ocean.

Each of the above hypotheses involves a potentially large number of feedbacks between the marine C, N, P, O, and S element cycles, but there remains an incomplete picture of exactly how these major biogeochemical cycles may have functioned through the Proterozoic and early Phanerozoic. We lack good integrated biogeochemical models for this interval. A number of models have been developed to address specific hypotheses, but these have typically involved either highly simplified representations of the oceans or only selected aspects of the biogeochemistry, or both [*Bartley and Kah*, 2004; *Bjerrum and Canfield*, 2004; *Canfield*, 1998; *Lenton and Watson*, 2000b; *Rothman et al.*, 2003; *Van Cappellen and Ingall*, 1996]. Nevertheless, these models have been very valuable in helping to frame questions and test hypotheses in a quantitative way.

To date, there has been relatively little work on constructing more "realistic" biogeochemical models applicable prior to the Mesozoic. Clearly one reason for this has been a fear that the lack of constraints threatens to undermine the validity of any but the simplest representations. While this remains a concern, there are now good reasons to investigate how another level of model sophistication could bring new insight into Deep Time problems. The rapidly improving quality and increasing diversity of Deep Time data sets and the increasing sophistication of hypotheses generated from them require more sophisticated tools for evaluation.

1.2 *The Need for a New Class of Models*

Biogeochemical models for paleoceanographic applications range from simple zero-dimensional models of a well-mixed ocean to fully-coupled atmosphere-ocean general circulation models (GCMs). Model complexity is governed by the tradeoffs between conceptual simplicity, computational cost, and realistic detail (Table 1.1). Simple box models that represent the ocean with only a few boxes are advantageous because they are relatively easy to assemble and explain. It is often possible to obtain analytical solutions for these models, and they can be readily integrated numerically for millions of years. Because they are intuitively accessible, simple box models have been extremely influential in shaping our understanding of more complex processes. However, the major disadvantage of these simple models is that they can fail to adequately resolve spatial and depth gradients and related processes, resulting in severe model biases. A well-known example from the literature serves as an illustration. An early generation of ocean box models showed that enhanced nutrient utilization efficiency in the Southern ocean could drive much or all of the glacial-interglacial change in pCO_2 [*Knox and McElroy*, 1984; *Sarmiento and Toggweiler*, 1984b; *Siegenthaler and Wenk*, 1984b]. These results shaped the thinking of an entire generation of scientists and aspects of their predictions are still being tested today. However, these same models also predicted that the high nutrient utilization efficiency would result in anoxia of the deep ocean [*Sarmiento et al.*, 1988a], a prediction has not been supported by observations from marine sediment cores. Since then, it has been shown that limitations inherent in the simple model structure resulted in excessive sensitivity to high-latitude nutrient utilization, resulting in some predictions that were not correct.

Problems with the high-latitude oversensitivity of 3-box models, coupled with rapid advances in computational power led the majority of the oceanography community to favor ocean general circulation models over box models by the mid-1990's. Modern

Table 1.1. Continuum of model sophistication available to the scientific community for paleoceanographic simulations emphasizing the role of the new ICBM models proposed in this work.

Class	Number of Boxes (# Dim)	CPU time/ Model kyr [1]	Primary Advantages	Primary Disadvantages
1 Box Model	1 (0 D)	< 5 sec	Simplicity, Analytic Solutions	Unable to Represent Surface Ocean
2 Box Model	2 (0 D)	< 5 sec	Analytic, Represents Surface Ocean	Simulates Anoxic Modern Deep Ocean
3 Box Model	3 (0 D)	< 5 sec	Analytic, Represents Low/High Latitude Surface Ocean	High-Latitude Oversensitivity
Multiple Box Model	3-10 (0,1-D)	5 sec -1 min	'Realistic' Circulation and Sensitivity	Poor Resolution of Redox Gradients
ICBMs	10-100's (1,2-D)	10 sec-15 min	'Realistic' Circulation and Sensitivity, Good Resolution of Redox Gradients, Computational Fast	No Analytic Solutions, Circulation Imposed
2-D OGCMs	100-10000 (2 D)	1.5-100 min	Dynamic Circulation, Good Resolution of Redox Gradients	Biogeochemistry Restricted by Computational Cost
3-D EMICs	$1000\text{-}10^6$ (3 D)	30 min – >100 hrs	Coupled Atmosphere-Ice-Ocean-Land; Scalable Resolution and Complexity	Restricted Biogeochemistry; Geostrophic Physics
3-D GCMs	$10^6\text{-}10^8$ (3 D)	>1000 hrs	Improved Resolution, 'Complete' Physics	Computational Cost/Complexity
High Res. 3-D GCMs	$\geq 10^8$ (3 D)	>10000 hrs	Km-Scale Resolution; Resolves Second-Moment Statistics	Computational and Hardware Cost/Complexity

[1] Normalized by processor speed to 1 Ghz for comparison purposes. CPU time is a complex function of many variables and thus is only a rough approximation. Actual run times can vary 10-100X depending on the details of the simulation.

global GCM codes typically employ hundreds of thousands or millions of "boxes". The circulation is computed dynamically by solving the primitive dynamical equations or a close approximation, typically driven by observations of surface wind stress, heat flux, and freshwater flux. However, GCMs are poorly suited to pre-Mesozoic problems because the appropriate bathymetry and boundary conditions are poorly known. Moreover, GCMs are computational expensive, making it difficult to carry out long (100ky) integrations, implement detailed biogeochemistry, or run multiple sensitivity tests.

Because of this, a more efficient approach has been adopted by part of the biogeochemical modeling community working on Mesozoic, Cenozoic, and modern oceans. Recognizing the limitations of existing coupled atmosphere-ocean GCMs, a new class of models known as Earth Models of Intermediate Complexity (EMICs) has been developed [*Claussen et al.*, 2002]. EMICs are simplified GCMs that run at lower spatial resolution and with more highly parameterized dynamics compared with traditional GCMs. These simplifications dramatically reduce the computational costs, allowing for inclusion of alternative processes such as detailed biogeochemistry [*Ridgwell et al.*, 2007], coupled climate dynamics [*Petoukhov et al.*, 2005], and weathering processes [*Arens and Kleidon*, 2007], while remaining orders of magnitude faster than full, coupled GCMs. For example, the first generation of the GENIE EMIC coupled a 3-D geostrophic ocean model to a 2-D atmosphere model, and was thus capable of simulating 1000 model years per hour on a desktop PC [*Ridgwell et al.*, 2007] (adding a 3-D atmosphere slows down the computation by 100X however [*Lenton et al.*, 2007]). Although still in their infancy, it seems that EMICs will prove extremely useful for studying earth system processes since the Mesozoic or even Paleozoic. However, EMICs still face three major challenges. First, long integrations and parameter sweeps of ocean biogeochemistry will still require thousands of hours of CPU time, especially when coupled to a 3-D

atmosphere model. Second, for palaeoceanographic application, the models are limited by their sensitive dependence on accurate paleographic maps. For example, the Isthmus of Panama, Greenland-Scotland Ridge, and Drake Passage are critical in controlling contemporary circulation, but equivalent features would be difficult to map accurately prior to the Mesozoic or even the Cenozoic. Finally, EMICs are still relatively complex, thus it seems likely that most of their use will be by groups dedicated to their use and development, while box models are more accessible to a more diverse group of earth scientists.

1.3 *Utility and Limitations of Box Models*

As described above, simple box models of ocean circulation and chemistry, involving just two or three boxes, have been used for decades to illustrate import concepts in marine biogeochemistry with considerable success. The primary advantage of these models is that they permit concise analytical solutions, which illuminate key variables and behaviors, and are easy to implement and explain. The most often cited disadvantage of box models is that they impose a simple, steady, and idealized circulation. For pre-Cenozoic paleoceanographic models however, this disadvantage is small and may actually be beneficial to the investigator. The reason is that the accuracy of paleogeographic maps decreases with time, and by the Mesozoic decreased bathymetric and topographic resolution make it difficult to construct meaningful 3-D dimensional models. Simple box models which can represent the first-order processes of modern ocean circulation—deepwater formation, isopycnal transport, and regional upwelling—provide the paleoceanographic modeler with direct access to the relevant, if idealized, circulation parameters and the ability to quickly conduct numerous sensitivity tests. The general structure of the meridional overturning circulation, with high-latitude ventilation of the deepwater and ventilation of the thermocline by outcropping isopycnals, seems likely to be the dominant circulation mode on any rotating planet with an equator-to-pole

temperature gradient. Nevertheless, as work progresses on haline circulation modes [*Brass et al.*, 1982] and other physically-based alternative circulation patterns [*Winguth and Maier-Reimer*, 2005], intermediate-complexity box models can be easily modified to represent these circulation patterns if desired. The main advantage of box models for the biogeochemist is not that they eliminate the need to consider realistic ocean circulation, but that, given a general pattern of overturning circulation, they allow rapid biogeochemical simulation at reduced computational cost, facilitating exploration of both the biogeochemical and circulation parameter space.

A second important disadvantage of box models is that, by only coarsely-approximating depth and spatial gradients, they can produce compelling results which turn out to be model artifacts under more careful scrutiny. There are many examples of this type of limitation in the literature and it is useful to review the some of these box models and their known limitations before continuing. A schematic illustration of some of the models discussed here is provided in Figure 1.1.

The simplest ocean models are 1-reservoir, 0-dimensional representations of a well-mixed ocean. These models are commonly used when modeling the long-term geological cycling of elements between the ocean/atmosphere, continents, and upper mantle [*Derry et al.*, 1992]. Their simplicity makes them especially easy to invert when solving for unknown mass fluxes and the assumption of a single well-mixed ocean box is easily justified when the residence time of the simulated components greatly exceeds the ocean mixing time (~1000 yr). While these calculations provide important constraints on global biogeochemical cycling, the point-like geometry of these models makes it difficult to understand the internal, mechanistic controls on such processes. Without added resolution, they cannot represent primary production and other processes at the ocean surface.

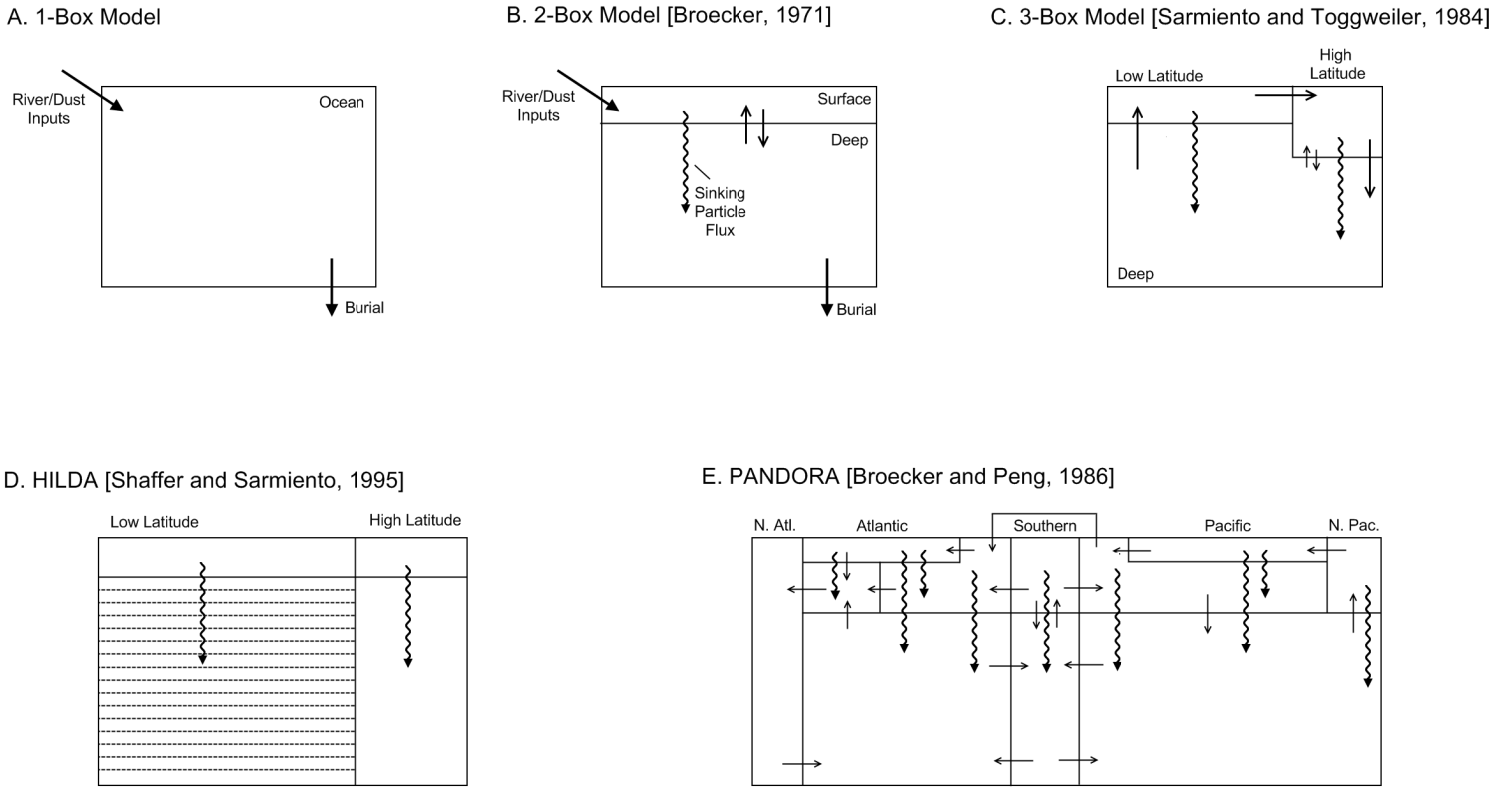

Figure 1.1. Schematic depiction of several generations of box models discussed in the text. Straight arrows represent inputs, outputs, and internal mixing. Sinusoidal arrows represent fluxes of sinking particulate matter. Dashed lines in the HILDA model approximately represent >40 vertical layers.

As an improvement, two-box models represent both the surface and deep ocean, allowing the representation of photosynthesis and drawdown of nutrients in the mixed layer. These models are useful for simulating the vertical distribution of phosphorus [*Broecker*, 1971; *Tyrrell*, 1999] and scavenged elements such as barium and thorium. However, a two-box scheme does not work for oxygen in the modern ocean [*Sarmiento et al.*, 1988a]. Taking the global mean surface $[O_2]_s \approx 250$ μmol/kg, mean surface $[PO_4^{3-}]_s \approx 0.57$ μmol/kg, mean deepwater $[PO_4^{3-}]_d \approx 2.15$ μmol/kg, and using the Redfield ratio of O_2:PO_4^{3-}: = -138:1, one can easily calculate the simulated deepwater oxygen to be 32 μmol/kg ($[O_2]_d = [O_2]_s - R \cdot ([PO_4^{3-}]_d - [PO_4^{3-}]_s$ [*Sarmiento et al.*, 1988a]). This is much lower than the observed mean deepwater $[O_2]_d$ =182 μmol/kg. The primary reason for this is that deep ocean ventilation mostly occurs at high latitudes where colder temperatures and incomplete phosphorus drawdown by phytoplankton results in high surface oxygen concentrations and low respiration demand [*Sarmiento et al.*, 1988a].

Realizing that high latitude ventilation was the key to ocean circulation, a variety of 3-box models were developed and studied extensively during the 1980's [*Knox and McElroy*, 1984; *Sarmiento and Toggweiler*, 1984b; *Sarmiento et al.*, 1988a; *Siegenthaler and Wenk*, 1984b]. This class of models shows extreme sensitivity to changes in high latitude nutrient utilization, capable of driving wide changes in P_{CO2} and ocean anoxia. Initially, this was seen as a breakthrough for explaining glacial/interglacial P_{CO2} [*Knox and McElroy*, 1984; *Sarmiento and Toggweiler*, 1984b; *Siegenthaler and Wenk*, 1984b] and ocean anoxic events [*Sarmiento et al.*, 1988a]. However, a major problem with this theory was that was no independent evidence for wide-spread anoxia during the last glacial cycle. A comparison of 3-box models with early 3-D general circulation models showed that the 3-box models greatly overestimated the drawdown of atmospheric P_{CO2} and water column anoxia produced by consumption of high-latitude nutrient consumption [*Sarmiento and Orr*, 1991]. Whereas the 3-box model responded to increased high-

latitude export production by driving the entire deep ocean anoxic, GCM simulations show that the O_2 depletion is actually restricted to only a small region of the water column below the high-latitude surface. The geometry of the 3-box model did not allow for a mid-water column oxygen minimum. Another problem with the simple 3-box model was that it did not include realistic inputs and burial of phosphorus. By including these process in the model, [*Hotinski et al.*, 2000] showed the deepwater anoxia in the 3-box model is transient. Increase nutrient utilization and primary production leads to increased phosphorus burial, thus reducing the oceanic phosphorus inventory and returning the deepwater to an oxic state.

Since the 1990's, a third generation of box models has developed based around two primary designs. The first design is based on the HILDA model [*Shaffer and Sarmiento*, 1995], which is a box-diffusion variant of the 3-box model (Figure 1.1). The second design is based on the PANDORA model [*Broecker and Peng*, 1986], which explicitly represents processes occurring in the North Atlantic, Atlantic, Southern Ocean, and Indo-Pacific. While several recent studies have successfully built upon the PANDORA design [*Kahana et al.*, 2004; *Keir*, 1988; *Lane et al.*, 2006; *Michel et al.*, 1995; *Popova et al.*, 2000], the main limitations of the PANDORA design for this study are its coarse vertical resolution and explicit dependence the existence of two large meridionally-oriented oceans, which cannot be guaranteed for all continental configurations. On the other hand, while the HILDA-type model is more applicable to this study, it has difficultly simultaneously representing the transport of circulation tracers due to its course meridional resolution [*Siegenthaler and Joos*, 1992], an issue which will be addressed below.

1.4 *Intermediate Complexity Box Models*

Consideration of the advantages and limitations of available box models, EMICs, and GCMs suggests that the development of an intermediate class of models which avoids

the known limitations of low-order box models and which is computationally faster and conceptually simpler than EMICs might be advantageous for some problems. This class of models is referred to here as intermediate complexity box models (ICBMs). The fundamental challenge for ICBMs is to make an effective simulation tool at the lowest complexity and computational cost.

For paleoceanographic problems, the first step in this process requires making an assumption about the pattern of meridional overturning circulation. For lack of other information, the working assumption used here is that the qualitative features of ocean circulation in the geological past were similar to the present: deepwater formation at one or both poles, the presence of well-stratified mid-latitude gyres, ventilation of the main thermocline via isopycnal outcrops, and prominent coastal upwelling along east boundary currents. On a rotating planet with a significant equator-to-pole temperature gradient, this assumption seems likely to be the rule rather than the exception. It is important to point out that the assumption is testable. Model predictions can be compared to observations from the geologic record, and if significant discrepancies are apparent, the model circulation can be readily modified in an attempt to reconcile the differences between simulation and observation. The advantage of using the modern circulation as a starting point is that the biogeochemical dynamics are easiest to interpret in a familiar circulation field.

Barring exotic circulation regimes, significant challenges remain in developing a box model that can simulate the modern meridional overturning circulation without excessive high-latitude sensitivity. In addition, the ICBM it should be able to simultaneously simulate modern potential temperature, background $\Delta^{14}C$, and bomb $\Delta^{14}C$ with the same diffusion parameterization, which was not possible in earlier models [*Siegenthaler and Joos*, 1992], and represent coastal upwelling zones with sufficient resolution to mechanistically simulate local anoxia and water column denitrification

[*Deutsch et al.*, 2004; *Knox and McElroy*, 1984]. Finally, the model should be open to inputs and burial of nutrients [*Hotinski et al.*, 2000], which requires realistic representation of hypsometry and burial of organic matter on the continental shelves [*Slomp and Van Cappellen*, 2007]. To meet these requirements, a box model with three defining features is proposed:

- The global ocean is divided into 3 geographic regions, representing high-latitude ventilation, ocean gyres, and coasting upwelling zones. This combines features of box-diffusion models (e.g. HILDA, [*Shaffer and Sarmiento*, 1995]) with the upwelling zone model of [*Deutsch et al.*, 2004], to divide the modern ocean into high, intermediate, and low-oxygen regions, each with distinctive and generalizable circulation processes.
- The model subdivides each region vertically into a number of depth layers which will prevent the high-latitude oversensitivity originally described by [*Sarmiento and Orr*, 1991]. A sufficient number of layers are chosen to represent the shelf bathymetry and resolve redox-depth gradients in the water column.
- The gyre region's thermocline layers are ventilated by direct mixing with the gyre and high-latitude surface boxes to represent ventilation along outcropping isopycnals at increasing latitude [*Sarmiento*, 1983a]. Ventilation along mid-latitude outcrops in the real ocean will be represented as a linear combination of fluxes from the high-latitude and low-latitude surface boxes in the ICBM model.

A model with these features is developed in Section 2. In Section 5, sensitivity experiments demonstrate that this new model avoids many of the known deficiencies of previous box models for simulating the modern circulation. The new model is capable of simultaneously simulating the modern observed distribution of potential temperature, background $\Delta^{14}C$, bomb $\Delta^{14}C$, and CFC-11; and avoids the high-latitude sensitivity to ocean anoxia described previously.

1.5 *Biogeochemistry Overview*

The second goal of this thesis is to develop a general, mechanistic model of marine biogeochemistry applicable to Earth history at different intervals, potentially as far back as the early Proterozoic. The model includes representations of the carbon, nitrogen, phosphorus, oxygen, and sulfur cycles, with the idea that the proper interpretation of the isotopic trends and other geologic records must also produce plausible consequences for the coupled C-N-P-O-S system. Nitrogen cycling is modeled in particular detail. Because this biogeochemical system is thought to equilibrate rapidly in a geologic sense (<100ky), the interpretation of longer events can often be viewed as a series of quasi-equilibrium states. The utility of such a model is that it explicitly combines our theoretical understanding of various biogeochemical processes when examining proxy constraints from the geologic record. For example, apparently high rates of organic carbon burial (say, inferred from $\delta^{13}C$ records) cannot be sustained for long periods without substantial implications for the cycles of the other elements which are highly coupled to carbon, such as phosphorus and oxygen. Similarly, hypotheses that try to explain variations in "observables" such as $\delta^{13}C$ and $\delta^{34}S$ records must, at the least, also produce plausible consequences for the elemental cycles of C, O, N and P.

A complete description of the biogeochemical model is presented in Section 3, so only brief synopsis is provided here. The biogeochemical submodel is one-dimensional and is applied to each spatial region (gridpoint) of the model in series. Allochthonous nutrients inputs and gas exchange take place across the ocean surface. Two classes of phytoplankton, conventional phytoplankton and diazotrophs (nitrogen-fixers), compete in the surface box for phosphorus [*Tyrrell*, 1999]. Conventional phytoplankton are additionally restricted by the availability of nitrogen, while diazotrophs are geographically restricted to the gyre surface reservoir. Limitation of primary production by light and iron are not explicitly simulated at present, although a flag for limiting

nutrient drawdown is provided and utilized for limiting high-latitude nutrient drawdown to present observed levels. Phytoplankton mortality results in the export of a fraction of particulate organic matter, with the remaining organic matter going into labile and semi-labile dissolved organic matter pools. All organic matter pools are assumed to have a Redfield composition [*Redfield*, 1958]. In each vertical level a fraction of the export production is hydrolyzed to DOM [*Martin et al.*, 1987] and another fraction is intercepted by the sediment surface as determined by the model hypsometry. In the water column, labile DOM is subject to remineralization by an explicit population of microbial heterotrophs, which utilize O_2, NO_3^-, NO_2^-, and SO_4^{2-} as oxidants in order of free energy yield. Remineralization products can be utilized by secondary chemolithoautotrophic functional groups, including ammonium-oxidizers, nitrite oxidizers, and anaerobic ammonium oxidizers (anammox), the populations of which are also explicitly modeled. Finally, organic matter which rains out onto the sea floor is passed to the benthic submodel—a series of parameterizations which simulate organic matter and nutrient burial, benthic denitrification, and return of remineralization products to the water column.

1.6 *Model Validation*

The last step of developing any new model for paleography is to first test it against the modern ocean. Since the goal to simulate a very wide range of paleoceanographic redox conditions, the model is tested against both the modern Global Ocean and the Black Sea in Sections 5 and 6 respectively. The Global Ocean case tests the model's performance under relatively oxidizing conditions. It is also intended to demonstrate the consequences of simulating several broad ocean basins as a single large basin. The Black Sea is the world's largest anoxic basin, and is characterized by a well-stratified estuarine circulation. Can the same biogeochemical model be used to simulate both regions, simply by changing the model geometry and circulation? Simulation of the Black Sea in Section

6 shows that it can. The ability to use a single, relatively simple and versatile model to quickly explore a large number of fundamental hypotheses in palaeoceanography will have important ramifications for future work.

SECTION 2

CIRCULATION SUBMODEL

2.1 *Circulation Overview*

Conceptually, the ICBM ocean is divided into several spatial regions defining different regimes of physical mixing, for example “high-latitude,” “gyre”, and “upwelling” regions. Each spatial region (i.e. gridpoint) is then divided into separate vertical levels to resolve depth profiles. As will be shown, this 1.5-dimensional approach avoids many of the artifacts of low-resolution models while retaining the simplicity and computational speed of box models. In addition, it allows ICBMs produce well-resolved depth profiles of components and benthic fluxes to facilitate comparison with observations.

Complete specification of the model circulation requires specifying the model geometry, advective circulation, vertical and horizontal diffusivity, and “subgrid-scale” ventilation. Here, the terms vertical and horizontal diffusivity are used interchangeably with diapycnal and isopycnal diffusivity to denote mixing within and between vertical columns. Non-local mixing refers to transport between nonadjacent vertical levels of a model region due to unresolved advective processes; for example, seasonal ventilation of the gyre thermocline by isopycnal shoaling and geostrophic subduction.

Section 2.2-2.5 describe the simulation of each circulation processes in detail, accompanied by estimates of parameter values from the modern global ocean. Section 2.6 describes a compact and efficient transport matrix approach to implementing the combined advective and diffusive circulation. The concepts and parameter values provided below are used to construct a model of the modern global ocean in Section 5.

2.2 *Advection*

The meridional circulation of the modern ocean is dominated by high-latitude ventilation of the deep ocean, intermediate water production in the Antarctic Polar Front

Zone and North Pacific, and ventilation of the main thermocline along shallow isopycnals which outcrop equatorward of 50° latitude and upwell at the equator (Figure 2.1). These main components are essential to a first order representation of the modern meridional overturning circulation (MOC). Table 2.1 presents a summary of modern transport estimates for each of the major pathways illustrated in Figure 2.1. At present, North Atlantic Deep Water (NADW) and Antarctic Bottom Water (AABW) form the major inputs to the bathypelagic ocean contributing about 18 Sv each (Table 2.1). No deep water is formed in the North Pacific; however about 8 Sv of North Pacific Intermediate Water (NPIW) circulates through the main thermocline [*Fine et al.*, 2001]. In the southern hemisphere, the lower thermocline is ventilated by the injection of 10-13 Sv of Antarctic Intermediate Water (AAIW) just north of the Subantarctic Front [*Meijers et al.*, 2007; *Sloyan and Rintoul*, 2001]. AAIW is formed by the modification of upwelling NADW and AABW and is thought to close the Atlantic circulation by supplying a return flow compensating NADW formation [*Sloyan and Rintoul*, 2001]. In the upper thermocline, relatively well-isolated subtropical/tropical cells (STC) circulate in both the Atlantic and Pacific, driven by equatorial upwelling (Ekman divergence) along the equator and subduction and equatorward flow of subtropical gyre water in the mid-latitudes [*Hazeleger and Drijfhout*, 2006].

In addition to the gyres and high-latitude regions, to simulate the biogeochemistry of nitrogen in the modern ocean it is also necessary to explicitly resolve small regions of intense coastal upwelling that are associated with the existence of suboxic zones below the mixed layer. In these regions, high rates of primary production at the surface and the subsequent decomposition of organic matter in the water column can deplete dissolved

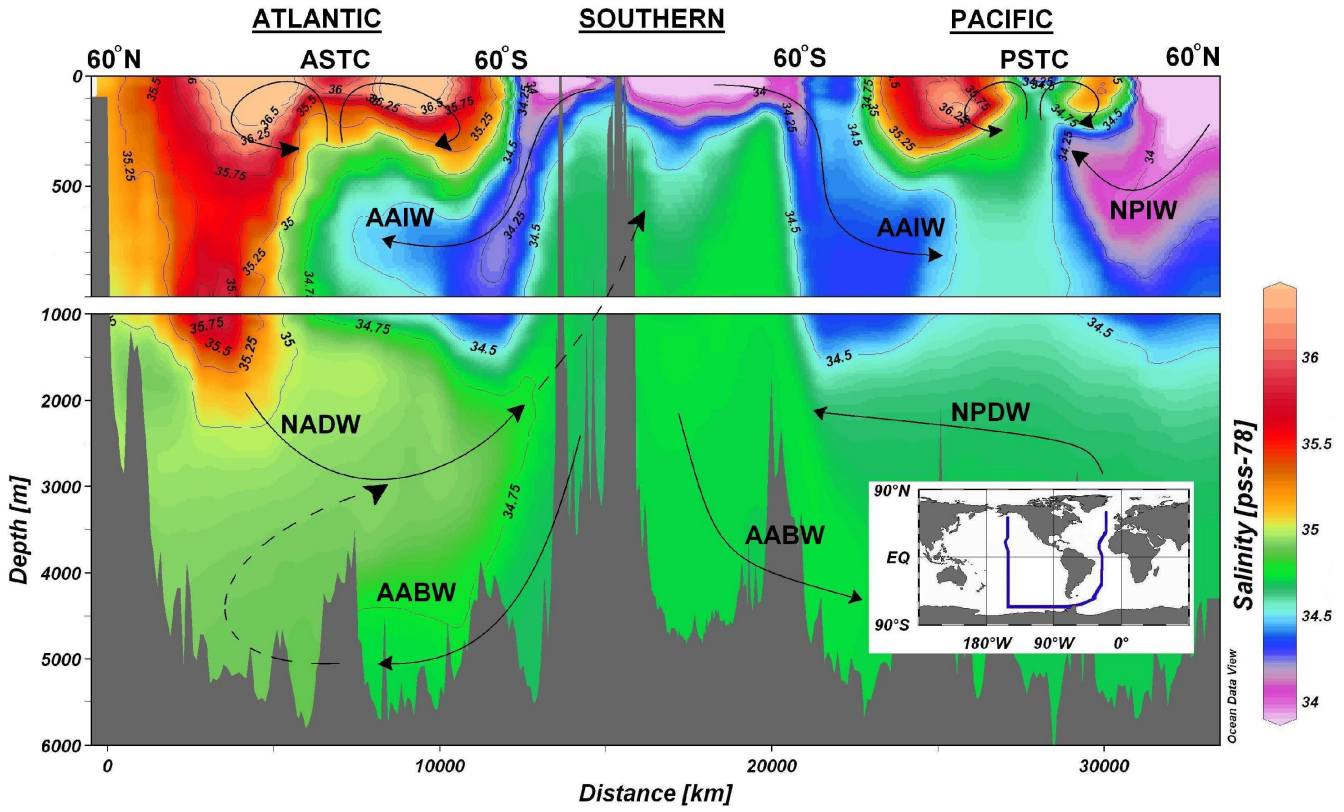

Figure 2.1. Present day meridional overturning circulation as illustrated along a section extending from the North Atlantic to North Pacific via the Drake Passage. Coloring corresponds to salinity. NADW: North Atlantic Deep Water; AABW: Antarctic Bottom Water AAIW; AAIW: Antarctic Intermediate Water; NPDW: North Pacific Deep Water; NPIW: North Pacific Intermediate Water; ASTC: Atlantic Subtropical-Tropical Cells; PSTC: Pacific Subtropical-Topical Cells. Figure after [Sarmiento and Gruber, 2006].

Table 2.1. Meridional Overturning Transport Fluxes (Sverdrups, 1 Sv=10^6 m^3 s^{-1})

North Atlantic Deep Water (NADW) Formation:		
[*Schmitz and McCartney*, 1993]	13	Literature Review
[*Broecker et al.*, 1998]	15	Radiocarbon
[*Smethie and Fine*, 2001]	17.2 ± 5.1	CFC intrusion rates
[*Orsi et al.*, 2001]	17.2	CFC intrusion rates
[*Lumpkin and Speer*, 2003]	15.6 ± 1.2	Box Inverse Model
[*Ganachaud*, 2003]	16 ± 2	Box Inverse Model
[*Luo and Ku*, 2003]	18	^{10}Be
[*Schlitzer*, 2007]	16.8	Global inverse of nutrients, radiocarbon, and CFCs
Antarctic Bottom Water (AABW) Formation:		
[*Broecker et al.*, 1998]	15	Radiocarbon
[*Orsi et al.*, 2002]	21	CFC intrusion rates
[*Ganachaud*, 2003]	21 ± 6	Box Inverse Model
[*Luo and Ku*, 2003]	21	^{10}Be
[*Schlitzer*, 2007]	16.8-17.9	Global OCGM inverse of nutrients, radiocarbon, and CFCs
Antarctic Intermediate Water (AAIW) Formation:		
[*Sloyan and Rintoul*, 2001]	13±2.5	Inverse box model
[*Meijers et al.*, 2007]	10	1/8 degree OGCM
North Pacific Intermediate Water (NPIW) Formation:		
[*Fine et al.*, 2001]	8	CFC intrusion rate
Equatorial Upwelling:		
Atlantic:		
[*Broecker et al.*, 1978]	17	Bomb radiocarbon
[*Blanke et al.*, 1999]	11.7	OGCM model
[*Zhang et al.*, 2003]	21 ± 2.1	J. Phys Oceanog. 33(8):1783-1797
[*Hazeleger and Drijfhout*, 2006]	7.5	1/4 degree GCM model
Pacific:		
[*Wyrtki*, 1981]	50	Ekman Divergence, Geostrophic Convergence
[*Fine et al.*, 2001]	65	CFCs
[*Johnson et al.*, 2001]	62	Analysis of repeat CTD and ADCP transects
[*McPhaden and Zhang*, 2002]	35.4-46.8	Windstress reanalysis
[*Kessler*, 2006]	30-50	Literature Review

Table 2.2. Coastal Upwelling Transport Fluxes (Sverdrups, 1 Sv=10^6 m^3 s^{-1})

Arabian Sea:		
[*Schott et al.*, 2002]	5.2	Geostrophic analysis of WOCE hydrographic sections
West Australia:		
[*Godfrey and Mansbridge*, 2000]	1.4	Geostrophic analysis of expendable bathythermograph sections
Benguela:		
[*Lutjeharms et al.*, 1991]	1.5	Observations of Upwelling Filaments
[*Skogen*, 2004]	2.2	1/5° Numerical Model
Peru/Chile:		
[*Wyrtki*, 1963]	3.3	Geostrophic analysis
[*Chavez et al.*, 1989]	2.2	
This work	4.3	Annual average of monthly PFEG upwelling index data (1981-2001)
Costa Rice Dome:		
[*Kessler*, 2002]	3	Geostrophic analysis of expendable bathythermograph sections
California:		
this work	2.8	Annual average of monthly PFEG upwelling index data (1946-1999)
Global Coastal Upwelling:		
[*Chavez and Toggweiler*, 1995]	15	Literature review
[*Walsh*, 1991]	21.5	Literature review
[*Brink et al.*, 1995]	12	Literature review
this work	17.7	Literature review

oxygen concentrations below 10 μmol/kg at mid-depths. Under these conditions, the oxidation of organic matter (denitrification) or ammonium (anammox) via the reduction of nitrate or nitrite to diatomic nitrogen is a biologically favorable process and a significant global sink of biologically-available nitrate in the ocean. Table 2.2 provides estimates of the annually-averaged upwelling rate for each of the major coastal upwelling zones as well as the Costa Rica Dome and West Australia. The sum of these contributions total 18±2 Sv, which compares well with previous estimates of 12-22 Sv [*Brink et al.*, 1995; *Chavez and Toggweiler*, 1995; *Walsh*, 1991], considering the large spatial and temporal variations in upwelling rates. Suboxic zones, defined here as regions with <10

μmol/kg O_2 in the WOA05 database[*Garcia et al.*, 2006a], underlie 2.4% of the ocean surface which is used here as the global coastal upwelling area (see Figure 5.1).

2.3 *Vertical Mixing*

Over the last decade, there has been increasing acceptance that the density-driven thermohaline circulation (THC) discussed by [*Broecker*, 1991] is at best an incomplete model. As summarized in a review by [*Wunsch and Ferrari*, 2004], the basic issue can be summarized using the analogy of "filling box" dynamics [*Baines et al.*, 1993; *Bloomfield and Kerr*, 1999]. The deep ocean can be thought of as a well-stratified box which is being constantly filled with dense (cold and salty) water from the high-latitudes. If this model were complete, the deep ocean would "fill" with cold dense water on a timescale of a few thousand years and then, in the absence of an ever-denser stream of high-latitude water, ventilation would cease. To avoid this inevitability, a source of energy is required to lift the center of mass of the deep water back to the surface again. In this interpretation, cold, dense water at the poles determines the regions of deep water formation, but it is the supply of thermal and mixing energy that ultimately determines the rate of deep water ventilation.

This understanding has led to an ongoing effort to construct a budget of the various sources of energy (tidal, wind, sensible heat flux, latent heat flux, geothermal, and buoyancy forcing) and detailed estimates of ocean mixing rates at a variety of scales. The estimates of mixing rates will be reviewed here briefly here to give some justification for the estimates of eddy diffusivity used in the model. Eddy diffusion is the mixing which occurs in a fluid due to turbulent convective motion (i.e. eddies). By analogy with random molecular diffusion, eddy diffusivity is a parameter which characterizes the rate of tracer transport due to the circulation of eddies which are too small to be explicitly resolved by the model grid spacing. One of the earliest estimates of abyssal vertical turbulent diffusivity and vertical velocity was derived by [*Munk*, 1966] by fitting the vertical

advective-diffusive balance relationship to temperature and salinity to find κ_z/w, the ratio of the vertical eddy diffusivity to the vertical velocity, and independently determining w by introducing radiocarbon data. This resulted in the canonical values κ_z = 1.3 $cm^2\ s^{-1}$ and $w = 1.4 \times 10^{-5}$ cm s^{-1}. Based on Munk's [1966] approach, a series of updated geochemical inverse estimates have been produced at increasing spatial and vertical resolution which have demonstrated significant spatial and depth variability of κ_z ranging between 0.1 – 10 $cm^2\ s^{-1}$, with higher values typically in the bottom 1000m of the water column or associated with regions of complex topography [*Ganachaud and Wunsch*, 2000; *Ganachaud*, 2003; *Munk and Wunsch*, 1998].

Beginning in the 1970's, a new direct method of measuring turbulent mixing in the ocean was pioneered [*Osborn and Cox*, 1972]. It is based on the recognition that all macroscale turbulence must be eventually dissipated at the molecular level. In turn, molecular dissipation requires a certain amount of fine-scale spatial structure in the temperature and salinity fields on the order of centimeters or less. By measuring this "microstructure" variance, it is possible to calculate the amount of supported macro-scale eddy turbulence. As reviewed by [*Gregg*, 1987] and [*Kunze et al.*, 2006], direct estimates of mixing away from the continental shelf and other irregular topographic features produced estimates of κ_z = O(0.1 $cm^2\ s^{-1}$), an order of magnitude smaller than the canonical value of [*Munk*, 1966]. Deliberate SF_6 tracer injection experiments conducted to resolve the discrepancy between geochemical inverse and microstructure measurements also resulted in estimates of κ_z = O(0.1 $cm^2\ s^{-1}$) [*Ledwell et al.*, 1998; *Polzin et al.*, 1997], vindicating the microstructure measurements. Yet, microscructure measurements in small regions near rough topographic features, such as midocean ridges and shelves, demonstrate values more than two orders of magnitude greater than this [*Polzin et al.*, 1997]. Thus overall, the general picture that has emerged is of generally low background mixing, O(0.1 $cm^2\ s^{-1}$), from thermocline to the bottom in regions of little

topography, with much higher rates of mixing, O(1-100 $cm^2\ s^{-1}$), along the shelf/slope and over complex topographic features such as ridges and seamounts. Wunsch has argued that the geochemical estimates represent a volume-averaged estimate of vertical mixing [*Ganachaud and Wunsch*, 2000; *Munk and Wunsch*, 1998; *Wunsch and Ferrari*, 2004].

To reconcile the microstructure and "volume-averaged" inversion results, it is common for numerical models to assume a depth-dependent κ_z which smoothly increases from O(0.1 $cm^2\ s^{-1}$) in the thermocline to O(1 $cm^2\ s^{-1}$) at depth as modeled by the inverse or hyperbolic tangent function [*Bryan and Lewis*, 1979]. This produces enough mixing in the deep ocean to allow for the use of realistic advective circulation, but prevents excessive mixing from fueling spurious primary production due to mixing of nutrients across the gyre thermocline. The thermocline and abyssal eddy diffusivities in the ICBM are set at $\kappa_z^s = 0.15\ cm^2\ s^{-1}$ and $\kappa_z^d = 1\ cm^2\ s^{-1}$, where the superscripts refer to shallow and deep respectively. The depth dependence of κ_z is then modeled as:

$$\kappa_z = \kappa_z^s + \frac{(\kappa_z^d - \kappa_z^s)}{2}\left(1 + \tanh\left(\frac{z - z^t}{z^\ell}\right)\right) \qquad 2\text{-}1$$

where $z^t = z^\ell = 1000$ m are the transition depth and transition length scale respectively.

Recently, a number of papers have pointed to very high vertical diffusivities around Greenland and in the Southern Ocean. Based on velocity fine structure, [*Garabato et al.*, 2004a] estimate diapycnals diffusivities approaching 100 $cm^2\ s^{-1}$ below 2000 m in the Greenland Sea, relaxing to background values above 1500m. High rates of deep mixing in the Greenland Sea are also supported by observations of CFC spreading [*Visbeck and Rhein*, 2000]and deliberate releases of SF_6 [*Watson et al.*, 1999]. In the Southern Ocean, CTD strain-variance based estimates of κ_z vary from background values of 0.1 $cm^2\ s^{-1}$ in the thermocline away from topography to values between 1-100 $cm^2\ s^{-1}$ in regions where the Antarctic Circumpolar Current impinges on regions of complex topography [*Garabato et al.*, 2004b; *Sloyan*, 2005; *Thompson et al.*, 2007]. Based on

3500 profiles of eddy diffusivity measurements, [*Kunze et al.*, 2006] found that mean vertical eddy diffusivity in the Southern Ocean is 7-10 times greater than for the Pacific at equivalent distance above the bottom, arguing for a deep, high-latitude eddy diffusion coefficient of 10-15 $cm^2\ s^{-1}$. Yet despite examining and averaging estimates of κ_z at many locations, it remains unclear whether the Kunze et al. results represent a truly unbiased volume-weighted estimate of high-latitude mixing. In both the Pacific and Atlantic, geochemical inverse solutions for vertical eddy diffusivity remain higher than microstructure- and CTD-based averages by an order of magnitude. By analogy, the default value of deep high-latitude vertical eddy diffusivity is set at $\kappa_z^h = 100\ cm^2\ s^{-1}$, relaxing to 1.5 $cm^2\ s^{-1}$ in the thermocline.

2.4 *Horizontal Mixing*

At basin scales, the magnitude of horizontal (isopycnal) eddy diffusivity in the ocean is 10^7-10^8 times larger than the vertical (diapycnal) eddy diffusivity due to the anisotropy of the density field. However, it has long been recognized that the apparent horizontal eddy diffusion is a strong function of the measurement scale [*Okubo*, 1971]. Simply put, the larger the patch size, the broad the range of turbulent scales capable of smearing it out, as opposed to advecting it in a Lagrangian sense. From a series of dye-release experiments on the scales of meters to hundreds of kilometers, *Okubo* [1971] found that:

$$\kappa_h = 0.5792 \cdot \ell^{1.15} \qquad 2\text{-}2$$

where κ_h is the horizontal eddy diffusivity ($m^2\ s^{-1}$) and ℓ is the average linear dimension of the patch (kilometers). [*Ledwell et al.*, 1998] arrived at a qualitatively similar conclusion for a SF_6 release in the North Atlantic, with both workers arriving at estimates of κ_h = O(1000 $m^2\ s^{-1}$) for ℓ = O(1000 km).

Several issues arise when attempting to implement this result in the ICBM. First, because the isopycnal diffusivity is much larger than the diapycnal diffusivity, significant

spurious diapycnal diffusivity can arise from assuming that isopycnal surfaces are coplanar with z-coordinate levels. Isopycnals are often inclined to the horizontal, so horizontal "isopycnal" diffusion has a spurious component that acts like diapycnal diffusion. Z-coordinate OGCMS now widely employ the [*Gent and McWilliams*, 1990] mixing scheme which utilizes off-diagonal terms in the mixing tensor to avoid the assumption that isopycnals are horizontal. However, this scheme is hardly applicable to models with just three horizontal regions. Moreover, the lack of specific horizontal geometry also means that it is difficult to implement conventional finite differences for the horizontal tracer gradients, since the model only assumes a surface area for each spatial region. To address these issues, two simplifications are made. The first is that horizontal mixing follows the pathways of advective fluxes between laterally adjacent regions. This is a coarse approximation to the ICBM model's concept of isopycnal layers. The second simplification is to specify reciprocal exchange fluxes instead of diffusivities, which can easily be shown to be equivalent for the discretized case:

$$J = \kappa_h \cdot A_\perp \frac{\partial C}{\partial x} = \kappa_h \cdot A_\perp \frac{C_2 - C_1}{\ell} = \frac{\kappa_h \cdot A_\perp}{\ell} C_2 - C_1 \qquad 2\text{-}3$$

where J is the flux between the reservoirs (moles time^{-1}), ℓ is a characteristic length separating the reservoirs, $A_\perp$ is the cross-section area separating two "isopycnally" adjacent reservoirs, and the leading term on the far right hand side has units of volume time^{-1}. If we allow that ℓ is of the same order as the length of the interface separating the two regions, where Δz is the depth of the interface separating the two regions, we can approximate:

$$A_\perp = \Delta z \cdot O(\ell) \qquad 2\text{-}4$$

$$J \approx \kappa_h \cdot \Delta z \cdot (C_2 - C_1) \qquad 2\text{-}5$$

In this form, a basin-scale horizontal eddy diffusivity of 1000 m^2 s^{-1} can be interpreted as 10^{-3} Sv of reciprocal mixing for each meter of depth.

2.5 *Non-local Mixing*

ICBMs must overcome one particularly severe problem in order to accurately represent modern global circulation using relatively few horizontal regions. At issue is the ventilation of the subtropical gyre thermocline (~100-1000m). Estimates from observations of tritium and CFCs in the Atlantic and Pacific suggest that gyre thermocline waters are rapidly ventilated, with tracer ventilation ages of 5 to 28 years increasing from approximately 100 to 800 meters depth [*Doney and Jenkins*, 1988; *Fine et al.*, 2001; *Sarmiento*, 1983b]. By computing the volume and mean ages of water masses bounded by closely spaced isopycnals, it is possible to estimate the ventilation rate of these water masses. For the North Atlantic, [*Sarmiento*, 1983b] calculated a ventilation rate of 30-40 Sv for σ_θ = 26.2-27.4; [*Doney and Jenkins*, 1988] found tracer ages to be 50% lower above σ_θ = 26.6, implying a slightly greater total ventilation flux. If the flux for the South Atlantic is similar, this would bring the total Atlantic ventilation flux to 60-80 Sv. For the North and South Pacific, [*Fine et al.*, 2001] estimates ventilation rates of 111 Sv and 123 Sv respectively for σ_θ = 24.5-27.3. Ignoring the contribution from the Indian Ocean, the global thermocline ventilation rate may be as large as 300 Sv. However, several steps in these calculations may lead to an upward bias. In [*Sarmiento*, 1983b], the assumption that tracers are instantaneously mixed throughout the thermocline leads to a value 36% higher than the assumption that shoaling water masses contain no CFC-11. Likewise, the CFC-11/CFC-12 ratio ages used [*Fine et al.*, 2001] reflect only the age of the CFC-bearing component of the water mass and ignore the contribution of dilution by older CFC-free water. This causes the water mass ages to appear too young, thereby increasing the apparent ventilation rate. If the minimum rate of global gyre thermocline ventilation is taken as six times the lowest rate determined by Sarmiento for the North Atlantic (based on relative surface area), it seems likely that the best estimate of the global gyre thermocline ventilation rate is between 150 and 300 Sv.

The problem is how to represent this large mixing term in a Z-coordinate box model with low latitudinal resolution. Ventilation of an isopycnal layer occurs where it outcrops into the surface mixed layer. For deeper layers, these outcrops occur at high latitude (>50°) and are well-described by the paradigm of high-latitude ventilation. However, water masses with $\sigma_\theta < 27.5$ generally outcrop equatorward of 50°, implying that vertical levels as deep as 1000m can be ventilated from the surface. Using the HILDA model, [*Siegenthaler and Joos*, 1992] showed that a box model cannot be simultaneously calibrated for temperature and bomb radiocarbon if the gyre thermocline is considered to be a single reservoir ventilated only by vertical eddy diffusion, since this approach fails to capture differences in the meridional gradients of various tracers. As represented by the thermocline ventilation model of [*Sarmiento*, 1983b], each progressively deeper thermocline layer should outcrop further poleward. Explicit representation of this process would require that each vertical level in the model be accompanied by a corresponding spatial outcrop region, dramatically increasing the complexity and numerical cost of the model. As a compromise, the global ICBM model implemented in Section 5 allows direct mixing between each gyre thermocline reservoir and both the low-latitude and high-latitude surface reservoirs (Figure 2.2). By varying the proportion of low-latitude and high-latitude surface water contribution to the ventilation of flux of each layer, it is possible to approximate the meridional gradient of each tracer as a linear combination of only two surface end-members.

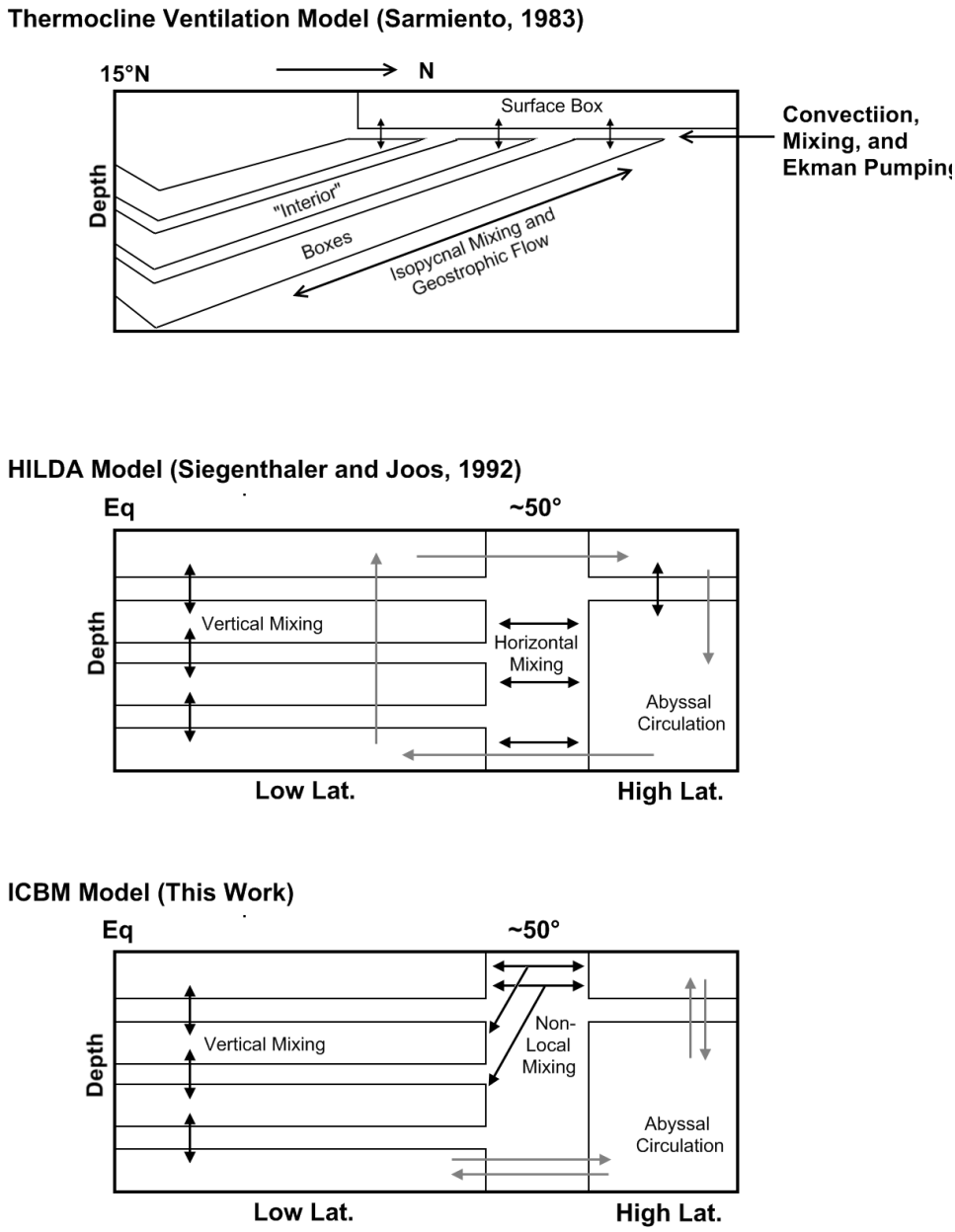

Figure 2.2. Schematic illustrating the thermocline ventilation schemes used in several box models. The ICBM model in the lower panel attempts to combine features of the thermocline ventilation model of [*Sarmiento*, 1983b] and the numerical version of HILDA model [*Siegenthaler and Joos*, 1992]. Non-local mixing between the high/low latitude surface reservoirs and the gyre thermocline layers is used to parameterize ventilation along outcropping isopycnals.

2.6 *The Transport Matrix*

The ICBM physical circulation is implemented as a sparse transport matrix, **T**, which contains all of the advective, diffusive, and non-local mixing terms. The construction of **T** is demonstrated for a small example problem in Appendix A, so only a conceptual overview is provided here. Specifically, if the ICBM has n reservoirs, then **T** is an n×n matrix such that:

$$\left.\frac{\partial \mathbf{C}}{\partial t}\right|_{transport} = \mathbf{TC} \qquad 2\text{-}6$$

where the entries of **T** have units of time^{-1} and **C** is an n×m matrix of (m) state variables (concentrations), e.g.:

$$\mathbf{C} = \begin{bmatrix} PO_{4,1} & O_{2,1} & \cdots & C_{m,1} \\ PO_{4,2} & O_{2,2} & \cdots & C_{m,2} \\ \vdots & \vdots & \ddots & \vdots \\ PO_{4,n} & O_{2,n} & \cdots & C_{m,n} \end{bmatrix} \qquad 2\text{-}7$$

The interpretation of **T** is such that for all off-diagonal entries, T_{ij} is the volume (mass) flux *to* reservoir *i from* reservoir *j* (F_{ij}), divided by the volume (mass) of reservoir i.

$$T_{ij} = \frac{F_{ij}}{V_i} \qquad 2\text{-}8$$

The entries on the diagonal, T_{ii} , are the effluxes from reservoir *i* :

$$T_{ii} = \frac{-\sum_{i}^{i \neq j} F_{ij}}{V_i} \qquad 2\text{-}9$$

and in general are the only negative entries in **T**. This approach provides a convenient formalism for the precalculation of all transport weights that is easy to code and check. When the basin is closed, as is the global ocean, all of the rows and columns in **T** should sum to zero prior to dividing by the reservoir volumes. Moreover, it allows the underlying

transport and finite-difference schemes to be modified independently of the circulation submodule itself.

The transportation matrix can be most easily constructed by summing the contributions of each of the circulation terms:

$$\mathbf{T}=\mathbf{T}_{advection}+\mathbf{T}_{Z-diffusion}+\mathbf{T}_{H-diffusion}+\mathbf{T}_{Non-local} \qquad 2\text{-}10$$

representing advective transport, vertical eddy diffusion, horizontal eddy diffusion, and non-local mixing processes respectively. To build the advection matrix, it is only necessary to provide the inputs to each reservoir:

$$T^{ij}_{advection} = \frac{1}{V_i}\begin{cases} Q_{ij} & i \neq j \\ -\sum_{j \neq i} Q_{ij} & i = j \end{cases} \qquad 2\text{-}11$$

where Q_{ij} is the flux (kg yr^{-1}) from reservoir j to reservoir i and V_i is the mass of reservoir i (kg). In the language of finite-differences, this is the first-order upwind method. The construction of the non-local mixing matrix proceeds similarly and can be directly combined with the advective case, so it is not considered separately.

The vertical diffusion matrix is constructed using second-order center differences with insulated boundaries:

$$T^{i,j}_{Z-diffusion} = \frac{1}{V_i}\begin{cases} \dfrac{2K_z^{i-1,i}A^{i-1,i}}{h_{i-1}+h_i} & j = i-1 \\ -\dfrac{2K_z^{i-1,i}A^{i-1,i}}{h_{i-1}+h_i} - \dfrac{2K_z^{i,i+1}A^{i,i+1}}{h_i+h_{i+1}} & j = i \\ \dfrac{2K_z^{i,i+1}A^{i,i+1}}{h_i+h_{i+1}} & j = i+1 \end{cases} \qquad 2\text{-}12$$

where $K_z^{i-1,i}$ and $A^{i-1,i}$ are the vertical eddy diffusion coefficient (m^2 yr^{-1}) and horizontal cross-sectional area (m^2) at the boundary between reservoir i-1 and reservoir i respectively, and h_i is the vertical thickness (m) of reservoir i. Terms are omitted at the upper and lower (insulated) boundaries whenever the index exceeds the dimensions of the model grid. Boundary fluxes due to sediment fluxes, gas exchange, and nutrient inputs are

all handled in the biogeochemistry submodule. When the ICBM has more than one horizontal region, the *i*-index is subdivided and the calculation repeated for each region.

The horizontal diffusion matrix is only applicable when the ICBM has more than one horizontal region. The calculation proceeds for each horizontal region, k, with adjacent regions, k-1 and k+1, along advective flow pathways (isopycnal layers). For reservoirs in a given horizontal region, there may be a one-to-one, one-to-many, or many-to-one relationship with reservoirs in an adjacent region. When the adjacency of reservoirs is one-to-one, the calculation is simply:

$$T^{ij}_{H-diffusion} = \frac{K_h}{V_i} \cdot \frac{\left(h_i + h_j\right)}{2} \qquad 2\text{-}13$$

That is, the horizontal diffusive flux is proportional to the mean thickness of the two boxes. When the relationship is one-to-many, there are multiple boxes in the adjacent region mixing with a single box in the current region:

$$T^{ij}_{H-diffusion} = \frac{K_h}{V_i} \cdot \frac{h_j}{\sum h_j} \cdot \frac{\left(h_i + \sum h_j\right)}{2} \qquad 2\text{-}14$$

where $\sum h_j$ is the sum of the thicknesses of all the reservoirs in the adjacent region that are isopycnal with reservoir *i* in the current region. Conversely, when the relationship is many-to-one, there are multiple boxes in the current region mixing with a single box in the adjacent region:

$$T^{i,j}_{H-diffusion} = \frac{K_h}{V_i} \cdot \frac{h_i}{\sum h_i} \cdot \frac{\left(\sum h_i + h_j\right)}{2} \qquad 2\text{-}15$$

where $\sum h_i$ is the sum of the thicknesses of all the reservoirs in the current region that are isopycnal with reservoir *j* in the adjacent region. In either case, the total horizontal mixing is linearly interpolated with depth between adjacent regions.

SECTION 3

BIOGEOCHEMICAL SUBMODEL

3.1 *Biogeochemical Submodel Overview*

In each areal region, an identical copy of the 1-D biogeochemical model simulates primary production, atmospheric gas exchange, dissolved and particulate organic matter export and remineralization, chemosynthetic reactions, and benthic processes (Figure 3.1). At present, the model is capable of simulating two classes of phytoplankton (nitrogen-fixing and "conventional" phytoplankton), phosphorus, nitrate, nitrite, ammonium, particulate organic matter (POM), labile and semi-labile dissolved organic matter (DOM), dissolved oxygen, dissolved nitrogen gas, total dissolved inorganic carbon (DIC), sulfate, sulfide, as well as the populations of five microbial functional groups: generalist heterotrophs, ammonium-oxidizers, nitrite-oxidizers, and anaerobic ammonium oxidizers (Table 3.1). In addition, the model is capable of simulating and tracking the distribution of potential temperature, salinity, CFC-11, and background and bomb radiocarbon, which are used to validate the circulation fields used in Section 5 and 6 for the modern global ocean and Black Sea respectively.

The basic features of the biogeochemistry submodel will be described briefly here, while the details will be provided in subsequent sections. The biogeochemical model is similar to many other models in the literature in that it describes the one-dimensional cycle of primary production in the photic zone, sinking and dissolved export, remineralization, secondary production (e.g. nitrification and anammox), and benthic processes. All of the particle, dissolved, and biomass organic matter pools in the model are initially assumed to have classical Redfield stoichiometry [C:N:P = 106:16:1, *Redfield*, 1958] and organic carbon is assumed to be in the zero oxidation state. The reason for this choice was to ensure that mass and redox balance of each process and the overall model were preserved exactly.

The model is open to riverine and atmospheric inputs of new nutrients, such as phosphate which must ultimately be buried in sediments to reach steady state. This open cycle is crucial for realistic long-term simulations of ocean biogeochemistry [*Hotinski et al.*, 2000]. In the surface layer of each one-dimensional region, nutrients are taken up by "conventional" phytoplankton and nitrogen-fixing diazotrophs [*Tyrrell*, 1999]. Both phytoplankton and diazotrophs compete for phosphorus, but phytoplankton are additionally restricted by the availability fixed-nitrogen species while nitrogen-fixers are limited to regions with surface temperatures above 17°C [*Breitbarth et al.*, 2007]. Phytoplankton limitation by light, iron, and zooplankton grazing are neglected in the current version of the model. Upon mortality, a fraction of newly formed phytoplankton biomass becomes particulate organic matter (POM) and sinks out of the surface layer [*Eppley and Peterson*, 1979]. Most of the sinking POM is instantaneously converted into labile and semi-labile dissolved organic matter (DOM) at depth [*Martin et al.*, 1987], but a small fraction, determined by the model hypsometry, is intercepted by the sediment surface in each vertical level and enters the benthic submodel.

Remineralization of organic matter takes place via labile and semi-labile dissolved organic carbon, and utilizes a variety of potential oxidants. The end products of remineralization are available for uptake during secondary chemoautrophic production. Repeated cycles of production and remineralization are made possible by advective and diffusive mixing, while burial of phosphorus in sediments provides the long-term (geological) constraint on primary production under modern mostly-oxic conditions. Most of the model parameters are provided in the text below, but additional parameters can be found in Appendix A.

Table 3.1. Simulated Biogeochemical Components

Component Name	Symbol	Units[5]
Dissolved Components:		
Phosphate	$[PO_4^{3-}]$	μmol kg^{-1}
Oxygen	$[O_2]$	μmol kg^{-1}
Nitrate	$[NO_3^-]$	μmol kg^{-1}
Nitrite	$[NO_2^-]$	μmol kg^{-1}
Ammonium	$[NH_4^+]$	μmol kg^{-1}
Dissolve Nitrogen Gas	$[N_2]$	μmol kg^{-1}
Sulfate	$[SO_4^{2-}]$	μmol kg^{-1}
Sulfide	$[H_2S]$	μmol kg^{-1}
Labile Dissolved Organic Matter[1]	[LDOM]	μmol C kg^{-1}
Semi-labile Dissolved Organic Matter[1]	[SDOM]	μmol C kg^{-1}
Total Dissolved Inorganic Carbon	[DIC]	μmol kg^{-1}
Phytoplankton Populations:		
Diazotrophs[a]	[NF]	μmol P kg^{-1}
"Conventional" Phytoplankton[1]	[PP]	μmol P kg^{-1}
Microbial Populations:		
Heterotrophic Bacteria[1]	[HET]	10^9 cells kg^{-1} [3]
Ammonium-oxidizing Bacteria[1,4]	[AOB]	10^9 cells kg^{-1} [3]
Nitrite-oxidizing Bacteria[1,4]	[NOB]	10^9 cells kg^{-1} [3]
Anammox Bacteria[1]	[AMX]	10^9 cells kg^{-1} [3]
Circulation Tracers:		
Potential Temperature	T	°C
Salinity	S	PSU
Radiocarbon	$[DI^{14}C]$	μmol kg^{-1} R^{*-1} [b]
CFC-11	[CFC11]	pmol kg^{-1}

[1] Organic matter pools are assumed to have Redfield stoichiometry, C:N:P = 106:16:1

[2] Where $R^* = (^{14}C/^{12}C)_{ref}$ and such that $\left[DI^{14}C\right]/[DIC] \equiv 1$ when in equilibrium with preindustrial atmosphere. Thus, $\Delta^{14}C \cong \left(\left[DI^{14}C\right]/[DIC] - 1\right) \cdot 1000$ ignoring the small correction for stable isotope fractionation.

[3] Assuming each cell contains 15×10^{-15}g carbon [*Nagata et al.*, 2000]

[4] Nitrifying "Bacteria" include nitrifying crenarchaeotes [*Wuchter et al.*, 2006]

[5] For concision, μM may be sometimes used interchangeably with μmol kg^{-1}.

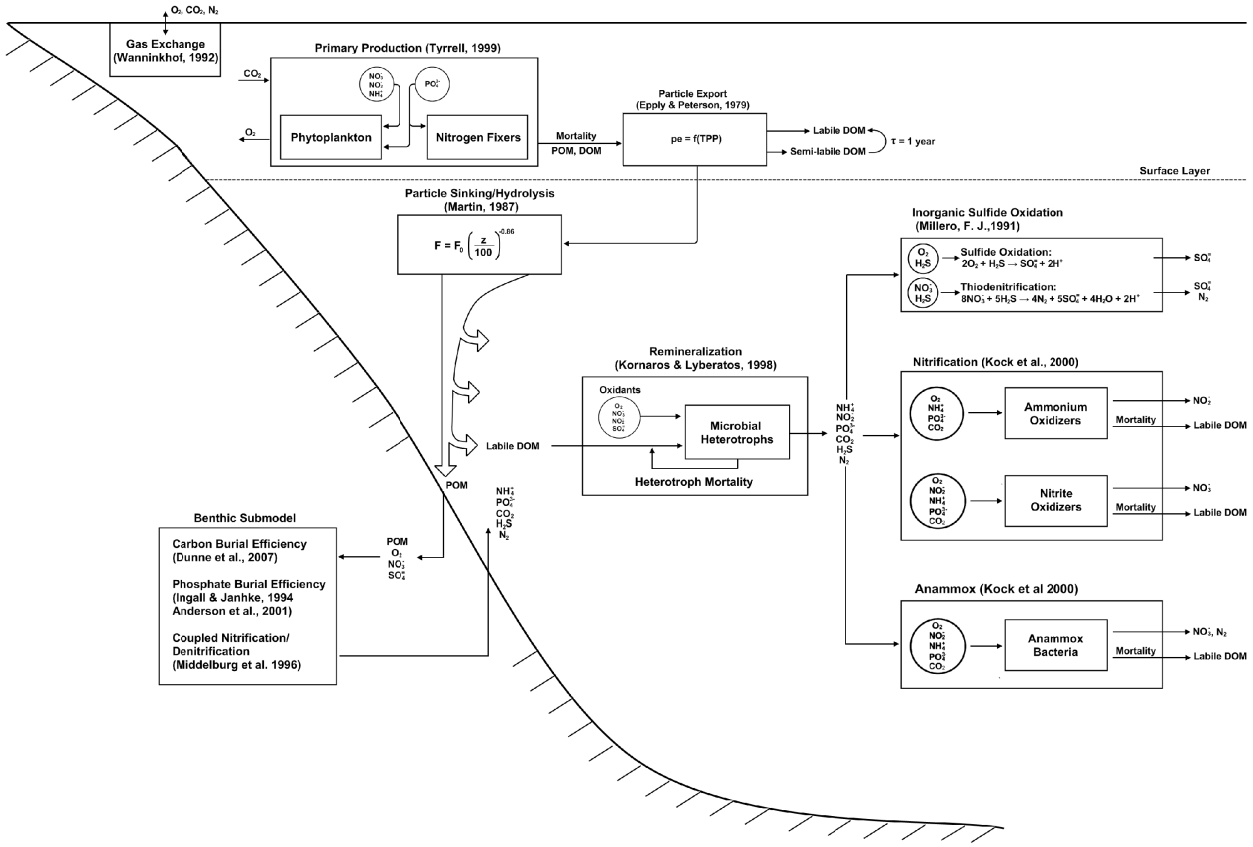

Figure 3.1. Schematic of the biogeochemical submodel. Large outer boxes represent individual submodules (m-files) which can be independently modified. Primary production and gas exchange occur only in the surface layer, while other processes operate in both the surface and multiple subsurface layers (not individually shown). Arrows and circles represent important fluxes and regulation pathways. Smaller interior boxes represent explicitly simulated biomass pools. See text for details.

3.2 *Surface Gas Exchange*

Rates of gas exchange are strongly dependent on the sea surface state and therefore surface wind speed [*Liss and Merlivat*, 1986]. Since this information is unavailable in the deep geologic past, the model is instead parameterized with a single value for the annually- and spatially- averaged mean oceanic squared wind speed, $\overline{U_{10}^2}$. The modern value of this parameter is 75 m^2/s^2 as calculated mean of monthly from the Quickscat climatology [*Risien and Chelton*, 2008]. Atmospheric exchange of O_2, N_2, and CO_2 are modeled using the Wanninkhof U^2 gas transfer velocity formulation [*Wanninkhof*, 1992]:

$$k_w = 0.31 \cdot \overline{U_{10}^2} \cdot (Sc/600)^{-0.5} \qquad 3\text{-}1$$

where k_w (cm/hr) is the gas transfer velocity, U_{10} (m/s) is the 10-meter wind velocity, and Sc is the dimensionless Schmidt number calculated for each gas using standard references [*Keeling et al.*, 1998; *Wanninkhof*, 1992]. The time rate of change of the dissolved gas in the ocean mixed layer is then:

$$\frac{\partial C}{\partial t} = \frac{k_w}{Z_{mix}}\left(C_{eq} - C\right) \qquad 3\text{-}2$$

where Z_{mix} is the depth of the mixed layer (equal to the thickness of the surface reservoir) and C_{eq} is the concentration of the gaseous species at equilibrium with the atmosphere, as calculated from standard gas solubility functions for seawater using the specified surface temperature and salinity [*Weiss*, 1970; *Weiss and Price*, 1980]. In the default modern simulation, partial pressures of atmospheric gases are set at 0.21 atm, 0.78 atm, and 280 µatm for O_2, N_2, and CO_2 respectively.

Because only about 0.5% of DIC is in the form of dissolved CO_2 (H_2CO_3*), the following expression is used to convert from DIC to dissolved CO_2:

$$[H_2CO_3^*] = \frac{K_2}{K_1} \cdot \frac{(2[DIC] - [ALK])^2}{[ALK] - [DIC]} \qquad 3\text{-}3$$

where K_1 and K_2 are the first and second carbonic acid dissociation constants, calculated for the specified surface temperature and salinity[*Millero*, 1995], and [ALK] is the alkalinity (μeq kg^{-1}). Because the modern validation runs are forced with observed alkalinity, the ICBM is not currently suited for oceanic CO_2 uptake studies for which a more detailed model of the carbon chemistry including a dynamic alkalinity state variable would be required. Currently, the simulation of [DIC] is meant only support simulation of the radiocarbon age for validation of the model circulation. At the surface, the air-sea flux of $DI^{14}C$, scaled by reference ratio as defined in Table 3.1 is:

$$\left.\frac{\partial\left[DI^{14}C\right]}{\partial t}\right)_{air-sea} = \frac{k_w^{CO_2}}{Z_{mix}} \cdot \left(\left[H_2CO_3 *\right]_{eq} - \frac{\left[H_2CO_3 *\right]}{\left[DIC\right]} \cdot \left[DI^{14}C\right] \right) \qquad 3\text{-}4$$

and the decay term, which occurs in every reservoir, is:

$$\left.\frac{\partial\left[DI^{14}C\right]}{\partial t}\right)_{decay} = -\lambda\left[DI^{14}C\right] \qquad 3\text{-}5$$

where $\lambda = 1.209 \times 10^{-3}$ yr^{-1} is the ^{14}C decay constant. Additional terms associated with transport of radiocarbon via the formation and remineralization of organic matter are discussed below. Because of the scaling applied to the units of $DI^{14}C$, the conventional radiocarbon age can be calculated:

$$t = -8033 \cdot \ln\left(1 + \frac{\Delta^{14}C}{1000}\right) = -8033 \cdot \ln\left(\frac{\left[DI^{14}C\right]}{\left[DIC\right]}\right) \qquad 3\text{-}6$$

where 8033 years is the mean lifetime of ^{14}C assuming a Libby ^{14}C half-life of 5568 years as is done by convention[*Stuiver and Polach*, 1977].

3.3 *Primary Production and Diazotrophy*

Primary production and diazotrophy (nitrogen-fixation) are simulated using populations of conventional phytoplankton (PP) and diazotrophs (NF) which compete for phosphorus and nitrogen [*Tyrrell*, 1999]:

$$\frac{\partial PP}{\partial t} = \mu_{PP} \cdot \min\left(\frac{PO_4^{3-}}{PO_4^{3-} + K_P}, f\left(NO_3^-, NO_2^-, NH_4^+\right) \right) \cdot PP\text{-}m \cdot PP \qquad 3\text{-}7$$

$$\frac{\partial NF}{\partial t} = \mu_{NF}(sst) \cdot \frac{PO_4^{3-}}{PO_4^{3-} + K_P} \cdot NF\text{-}m \cdot NF \qquad 3\text{-}8$$

where μ_{PP} and μ_{NF} are the maximum growth rates of conventional phytoplankton and nitrogen fixers, respectively; K_P is the Monod half-saturation parameter for phosphate-limited growth; and m is the mortality rate encompassing maintenance energy, grazing, and sinking. The maximum growth rate of the diazotrophs is reduced to zero when the specified surface temperature is less than 17°C, following experimental work with *Trichodesmium* IMS-101 [*Breitbarth et al.*, 2007]. In addition to phosphate, conventional phytoplankton can be limited by the availability of various fixed nitrogen species. The nitrogen limitation of [*Tyrrell*, 1999] was extended include NO_2^- and NH_4^+ following [*Gruber et al.*, 2006; *Parker*, 1993]:

$$f\left(NO_3^-, NO_2^-, NH_4^+\right) = \frac{NO_3^- + NO_2^-}{NO_3^- + NO_2^- + K_{Nox}} \cdot \frac{K_{Nred}}{NH_4^+ + K_{Nred}} + \frac{NH_4^+}{NH_4^+ + K_{Nred}} \qquad 3\text{-}9$$

where NO_3^- and NO_2^- have been summed in place of NO_3^- alone. This formulation assumes a preference for NH_4^+, because phytoplankton must first reduce NO_3^- prior to incorporation into biomass. In a review of six different parameterizations for NH_4^+ preference, [*Tian*, 2006] recommended the [*Parker*, 1993] formulation used here as the community standard.

Because of the metabolic cost of producing and maintaining the enzymes required to break the N_2 triple bond during the initial step of N_2-fixation, the reaction is only biologically favorable when fixed nitrogen species are limiting. This additional energy demand for nitrogen fixers is represented via a slightly lower maximum specific growth rate compared to conventional phytoplankton (87.6 yr^{-1} versus 91.25 yr^{-1} [*Tyrrell*, 1999]). The result is that N-fixation is favored only when conventional plankton are N-limited [*Tyrrell*, 1999].

The model does not currently include a parameterization of the iron-cycle, even though it has become widely accepted that broad regions of the ocean are limited by iron-availability and that this may have important implications for nutrient cycling [e.g.*Jickells et al.*, 2005; *Moore and Doney*, 2007b]. The reason for this is that, while the role of iron in the modern ocean is reasonably well-understood, its role over geological time is still much harder to predict or simulate in a mechanistic manner. In place of true Fe-limitation, the model offers an option to set a minimum level of PO_4^{3-} drawdown in the mixed layer to simulate the effects of Fe-limitation:

$$P - limitation = \min\left(\frac{\left(PO_4^{3-} - PO_4^{3-}{}_{min}\right)}{\left(PO_4^{3-} - PO_4^{3-}{}_{min}\right) + K_P}, 0 \right) \qquad 3\text{-}10$$

where $PO_4^{3-}{}_{\min}$ is the minimum allowed drawdown. By default, high-latitude $PO_4^{3-}{}_{\min}$ = 1.5 µmol/kg for modern global ocean simulation in agreement with observations. A second option is whether or not to allow nitrogen fixation in the upwelling zone surface. As reviewed by [*Canfield*, 2006], direct measurements in the Arabian Sea and nitrogen isotope studies of sinking POM in the Eastern Tropical Pacific suggest that there is only very limited nitrogen fixation occurring in intense regions of coastal upwelling. However, a global geochemical estimate of nitrogen fixation suggests that there may instead be an unusually high rate of nitrogen fixation in the Eastern Tropical Pacific [*Deutsch et al.*, 2007]. To handle either of these two cases, a user flag is supplied which can be specified to reduce the maximum growth rate of diazotrophs in particular spatial regions. By default, nitrogen fixation is disabled in the model upwelling region because preliminary experiments showed this to yield results more similar to the modern observations. Finally, because of the ability to enforce a zero growth rate for phytoplankton, either by toggling the N-fixation flag or setting $PO_4^{3-}{}_{\min}$ above ambient PO_4^{3-}, there is the potential to drive phytoplankton populations to extremely low values at which point numerical round-off errors can result in populations less than zero. To enhance the model stability under these

conditions, an small additional zero-order growth term is added which stabilizes phytoplankton populations at very low, but non-zero values [O(10^{-6}) μmol P kg^{-1}]. This extra source of phytoplankton biomass contributes a negligible amount of additional nitrogen, phosphorus, and organic matter to overall tracer budgets.

Finally, the net primary production and export production (μmol P kg^{-1} yr^{-1}) are calculated from:

$$NPP = \left(NF\_Growth + PP\_Growth\right) \quad 3\text{-}11$$

$$Export\ Production\ = f_{Export}\left(NF\_Mortality + PP\_Mortality\right) \quad 3\text{-}12$$

where f_{Export} is defined in the following section.

3.4 *Particle Export and Hydrolysis*

Upon mortality, photosynthetic biomass is transferred to one of two pools. It is either removed from the mixed layer as sinking particulate organic matter (POM) or converted to dissolved organic matter (DOM) *in situ*. The fraction of particle export is related to total primary production (NPP) by an empirical saturation relation fit to the data of [*Eppley and Peterson*, 1979]:

$$f_{Export} = 0.5 \cdot \frac{NPP^2}{NPP^2 + 92.8^2} \quad 3\text{-}13$$

where NPP is the net primary production as in equation 3-11 but converted to units of g C m^{-2} yr^{-1}. Exported organic matter is either intercepted by the sediment surface or converted to DOM at depth. The formulation of [*Martin et al.*, 1987] is used to describe the depth-dependent attenuation of the sinking particle flux due to remineralization:

$$F_{POM} = F_{POM}^{Z_{mix}} \cdot \left(\frac{Z + \left(100 - Z_{mix}\right)}{100} \right)^{-0.86} \quad 3\text{-}14$$

where F_{POM} is the flux of POM in at depth Z; $F_{POM}^{Z_{mix}}$ is the flux of POM at the base of the mixed layer; Z is the depth in meters (positive down); and Z_{mix} is the depth of the base of

the mixed layer. The equation has been modified from the original formulation of [*Martin et al.*, 1987] to accommodate situations where the mixed layer depth may not equal 100m.

The fraction of export production intercepted by the sediment surface is a function of both depth-attenuation of the particle flux and the basin hypsometry. Assuming a piecewise constant depth-derivative of the hypsometry over each reservoir's depth interval, we can calculate the flux of sinking POM intercepted by sediments in each reservoir:

$$\begin{aligned} F_{POM}^{Sed} &= \int_{Z_1}^{Z_2} F_{POM}(z) \cdot \frac{dSA}{dz} dz \\ &= \frac{dSA}{dz} \int_{Z_1}^{Z_2} F_{POM}(z)\, dz \\ &= \frac{dSA}{dz} \cdot \left[F_{POM}^{Z_{mix}} \cdot \frac{100}{0.14} \cdot \left(\frac{Z + (100 - Z_{mix})}{100} \right)^{.14} \right]_{Z_1}^{Z_2} \end{aligned} \qquad 3\text{-}15$$

where F_{POM}^{Sed} is the flux of POM to the sediment surface in µmol C yr-1, dSA/dz is the difference in surface area at the top and bottom of the reservoir interval divided by the reservoir thickness, and Z1 and Z2 are the depths at the top and bottom of a given reservoir respectively. We can then calculate the remineralized flux by difference:

$$F_{POM}^{Remin} = A^{Top} \cdot F_{POM}^{Top} - A^{Bottom} \cdot F_{POM}^{Bottom} - F_{POM}^{Sed} \qquad 3\text{-}16$$

where F_{POM}^{Remin} is the flux of organic matter (µmol C yr-1) transfered from the sinking POM pool to the DOM pools in a given reservoir, A^{Top} and A^{Bottom} are the basin surface area at the top and bottom of the reservoir, and F_{POM}^{Top} and F_{POM}^{Bottom} are the sinking POM fluxes per square meter at the top and bottom of the reservoir. As described below, the turnover time of DOM is very rapid, on the order of days or a year at most, such that it is functionally equivalent to assume either that POM consumption occurs directly or via a dissolution pathway. Because this turnover is so rapid, the addition of CO_2 and $^{14}CO_2$ to the DIC

pools is made concurrent with the transfer of organic matter to the labile (LDOC) and semi-labile (SDOM) pools, rather than after the actual oxidation step:

$$\left.\frac{\partial LDOM}{\partial t}\right)_{\text{Re min}} = \frac{0.7F_{POM}^{\text{Re min}}}{V} \qquad 3\text{-}17$$

$$\left.\frac{\partial SLDOM}{\partial t}\right)_{\text{Re min}} = \frac{0.3F_{POM}^{\text{Re min}}}{V} \qquad 3\text{-}18$$

$$\left.\frac{\partial DIC}{\partial t}\right)_{\text{Re min}} = \frac{F_{POM}^{\text{Re min}}}{V} \qquad 3\text{-}19$$

and the change in $DI^{14}C$ is calculated:

$$\left.\frac{\partial\left[DI^{14}C\right]}{\partial t}\right)_{\text{Re min}} = \frac{\left[DI^{14}C\right]_{surface}}{[DIC]_{surface}}\frac{F_{POM}^{\text{Re min}}}{V} \qquad 3\text{-}20$$

Detrital material that is not exported from the mixed layer as POM is converted directly to DOM in mixed layer, with 70% of the flux going to LDOM and 30% to semi-labile DOM (SDOM). The calculation for net flux of DIC and $DI^{14}C$ in the surface reservoir is similar to equations 3-19 and 3-20, but includes both CO_2 uptake by photosynthesis and remineralization.

3.5 *Organic Matter Remineralization*

The ICBM assumes that organic matter remineralization is predominantly microbial and that the substrate is exclusively labile dissolved organic matter (LDOM). For the modern ocean, vertebrates are thought to contribute less than 1% of total respiration while estimates of the metazooplankton contribution to range from 1-50% [*del Giorgio and Duarte*, 2002] with microbes making up the remainder. Even less is known about how these fractions have varied over Earth's geologic history. Fortunately, the rapid conversion of sinking POC to LDOC and subsequent remineralization in the model should adequately describe all of these modes, so long as particulate export and attenuation can be described by modern empirical export and particle flux attenuation functions. Several authors have proposed that carbon cycling prior to the evolution of

metazoans may have been dominated by dissolved and suspended organic carbon [*Fike et al.*, 2006; *Logan et al.*, 1995; *Rothman et al.*, 2003], which might be simulated by changing the terms of the particulate remineralization expression.

Like phytoplankton, the heterotrophic microbial reaction rates are simulated based on multi-substrate Monod kinetics where the volume-specific reaction rates depend on both the substrate concentrations and the organism population. The model heterotrophs consume oxidants in order of free energy yield: O_2, NO_3^-, NO_2^-, and SO_4^{2-}, in an extented and simplified version of the multiple-substrate inhibition model used by [*Kornaros and Lyberatos*, 1998] to model laboratory growth of *Pseudomonas denitrificans* on glutamate under oxic, anoxic, and transient conditions. Oxidation of organic matter by iron and manganese oxides is not currently simulated, since these elements are present at relatively low concentrations and their biogeochemistry is much more complex and poorly understood compared to oxygen, nitrogen, and sulfur.

Conceptually, the remineralization model has two parts, balanced stoichiometric redox equations for dissimulatory and assimilatory processes, and kinetic rate laws for each reaction. In general, the stoichiometric redox equations have the form:

$$\frac{1}{1-Y}\mathrm{LDOC} + n \cdot \mathrm{Ox} \xrightarrow{\text{Heterotrophs}} \frac{Y}{1-Y} \cdot \mathrm{Hetr} + n \cdot \mathrm{Ox}_{\text{reduced}} + \mathrm{CO_2} + \frac{16}{106}\mathrm{NH_4^+} + \frac{1}{106}\mathrm{PO_4^{3-}} \qquad 3\text{-}21$$

where Y is the bacterial growth efficiency (moles biomass/moles of carbon consumed), n is the number of moles of oxidant (Ox) required to oxidize 1 mole of LDOC (1 mole of $C^{(0)}$/mole LDOC) to CO_2. Hetr represents the moles of organic carbon in the new heterotrophic biomass, which can be converted to cells/L assuming 15 fg C/cell [*Nagata et al.*, 2000]. In the current version of the model, Y is held constant at 0.24 [*Bendtsen et al.*, 2002] for all substrates.

The rate of reaction 3-21 for each oxidant is determined by the instantaneous growth rate of heterotrophs on that oxidant:

$$\left.\frac{\partial Hetr}{\partial t}\right)_{Ox} = \mu_{Ox} \cdot [Hetr] \qquad 3\text{-}22$$

where μ_{Ox} is determined by a rate expression for the substrate limitation and inhibition of that particular oxidization pathway:

$$\begin{aligned}
\mu_{O_2} &= \mu_{\max,O_2} \cdot \left(\frac{LDOM}{LDOM + K_{S,O_2}}\right) \cdot \left(\frac{O_2}{O_2 + K_{O_2}}\right) \\
\mu_{NO_3^-} &= \mu_{\max,NO_3^-} \cdot \left(\frac{LDOM}{LDOM + K_{S,NO_3^-}}\right) \cdot \left(\frac{NO_3^-}{NO_3^- + K_{NO_3^-}}\right) \cdot \left(\frac{K_{I1,O_2}}{O_2 + K_{I1,O_2}}\right) \\
\mu_{NO_2^-} &= \mu_{\max,NO_2^-} \cdot \left(\frac{LDOM}{LDOM + K_{S,NO_2^-}}\right) \cdot \left(\frac{NO_2^-}{NO_2^- + K_{NO_2^-}}\right) \cdot \left(\frac{K_{I1,NO_3^-}}{NO_3^- + K_{I1,NO_3^-}}\right) \cdot \left(\frac{K_{I2,O_2}}{O_2 + K_{I2,O_2}}\right) \\
\mu_{SO_4^{2-}} &= \mu_{\max,SO_4^{2-}} \cdot \left(\frac{LDOM}{LDOM + K_{S,SO_4^{2-}}}\right) \cdot \left(\frac{SO_4^{2-}}{SO_4^{2-} + K_{SO_4^{2-}}}\right) \cdot \left(\frac{K_{NO_2^-}}{NO_2^- + K_{I1,NO_2^-}}\right) \cdot \left(\frac{K_{I2,NO_3^-}}{NO_3^- + K_{I2,NO_3^-}}\right) \cdot \left(\frac{K_{I3,O_2}}{O_2 + K_{I3,O_2}}\right)
\end{aligned} \qquad 3\text{-}23$$

Finally, the overall growth rate of heterotrophs is given by:

$$\frac{\partial Hetr}{\partial t} = \left(\mu_{O_2} + \mu_{NO_3^-} + \mu_{NO_2^-} + \mu_{SO_4^{2-}}\right) \cdot [Hetr] - mortality \qquad 3\text{-}24$$

with mortality term is discussed specifically in Section 3.7.

During denitrification, the oxidation of organic matter is coupled to the reduction of NO_3^- to N_2 in a five step process $\left(NO_3^- \rightarrow NO_2^- \rightarrow NO \rightarrow N_2O \rightarrow N_2\right)$[*Zumft*, 1997]. The trace gas products accumulate to only very low levels, and thus can be ignored for this application $\left(e.g. NO_3^- \rightarrow NO_2^- \rightarrow N_2\right)$. At present, it is unclear what fraction of reduced NO_3^- actually accumulates as free, extracellular NO_2^- during marine denitrification, as opposed to complete intracellular reduction to N_2 intracellular via tight coupling of the two enzymatic steps. To allow for both possibilities, the model provides a flag, fN_2 ($0 \leq fN_2 \leq 1$), which controls the fraction of NO_3^- reduced directly to N_2 with appropriate consideration of the change in redox stoichiometry. By default, this flag is set at 0.5, which seems to produce reasonable results.

3.6 *Nitrification:*

Oxidation of organic matter releases ammonium. Under aerobic conditions, nitrifying bacteria oxidize NH_4^+ to NO_3^- in a two-step chemolithoautrophic process, with NO_2^- as a free intermediate. The first step is carried out by ammonia-oxidizing bacteria (AOB), which oxidize NH_4^+ to NO_2^-. The second step in nitrification is carried out by nitrite-oxidizing bacteria (NOB), which oxidize NO_2^- to NO_3^- [*Ward*, 2000]. The overall stoichiometry of these reactions is commonly written:

$$\begin{aligned} NH_4^+ + 1.5O_2 &\rightarrow NO_2^- + 2H^+ + H_2O \\ NO_2^- + 0.5O_2 &\rightarrow NO_3^- \end{aligned} \qquad 3\text{-}25$$

No single nitrifying organism is known to oxidize NH_4^+ directly to NO_3^- [*Konneke et al.*, 2005]. However, the recent discovery that at least some crenarchaeotes, the largest group of marine microorganisms [*Karner et al.*, 2001], are capable of ammonia-oxidization has pointed out the need for continued research [*Ingalls et al.*, 2006; *Konneke et al.*, 2005; *Wuchter et al.*, 2006].

Since the equations in 3-25 are balanced redox equations, they cannot account for the electrons necessary to reduce CO_2 during carbon fixation. To represent balanced, whole-organism redox reactions, it is necessary to include carbon fixation and the uptake of nutrients to form nitrifier biomass (which is presently characterized by a *Redfield* compostion in the model):

$$\begin{aligned} 106CO_2 + 106H_2O + 16NH_4^+ + 1PO_4^{3-} &\rightarrow \\ 106\text{AOB or } 106\text{NOB} + 106O_2 & \end{aligned} \qquad 3\text{-}26$$

Estimates of N-oxidized/C-fixed by moles range from 7-16.6 for AOB and 40-80 for NOB [*Brion and Billen*, 1998 and references therein; *Glover*, 1985]. The ICBM is currently configured with mean values of 11 and 50, respectively. Combining these equations yields characteristic, balanced, whole-organism redox reactions:

$$11.15NH_4^+ + 15.5O_2 + CO_2 + 0.01PO_4^{3-} \xrightarrow{AOB} AOB + 11NO_2^- + 22H^+ + 21H_2O$$
$$50NO_2^- + 24O_2 + CO_2 + .15NH_4^+ + .01PO_4^{3-} + H_2O \xrightarrow{NOB} NOB + 50NO_3 \quad \text{3-27}$$

where AOB and NOB represent 1 mole C of nitrifier biomass. The kinetics of these reactions are controlled by the growth rates (i.e. carbon assimilation rates) of nitrifying organisms. The double-Monod growth model of [*Koch et al.*, 2000] used to simulate growth of aerobic and anaerobic nitrogen oxidizing bacteria in a rotating biological contactor is adopted here:

$$\frac{\partial AOB}{\partial t} = \mu_{AOB} \cdot \frac{O_2}{K_{O_2}^{AOB} + O_2} \cdot \frac{NH_4^+}{K_{NH_4}^{AOB} + NH_4^+} \cdot AOB \text{ - mortality}$$
$$\frac{\partial NOB}{\partial t} = \mu_{NOB} \cdot \frac{O_2}{K_{O_2}^{NOB} + O_2} \cdot \frac{NO_2^-}{K_{NO_2^-}^{NOB} + NO_2^-} \cdot NOB \text{ - mortality} \quad \text{3-28}$$

where μ is the maximum growth rate ($year^{-1}$), O_2, NH_4^+, and NO_2^- are dissolved concentrations of these species in µmol/kg, and K_{O2} and K_{NH4} are half-saturation constants. The endogenous respiration terms in the [*Koch et al.*, 2000] model have been replaced with an additional bacterial mortality term described below. Reactions rates are coupled to the whole organism stoichiometry equations via specification of the cellular organic carbon content (15 fg C/cell, [*Nagata et al.*, 2000]). Note that the above kinetic expressions are implemented in a slightly modified version from above. Addition terms limit growth under extremely low NH_4^+ or PO_4^{3-} concentrations (half-saturation constants of 0.03 µmol kg^{-1}), but have been omitted here for clarity since they have no effect under typical conditions. The purpose of these extra terms is to prevent nutrient drawdown from reaching negative concentrations very nutrient-limited circumstances.

Light-limitation of nitrification is thought to be the second major control on pelagic marine nitrification rates [*Guerrero and Jones*, 1996a; b; *Hooper and Terry*, 1974; *Horrigan et al.*, 1981; *Olson*, 1981a; b; *Ward et al.*, 1982; *Ward*, 1987]. While strong light inhibition has been demonstrated for both AOB and NOB, attempts to

determine which process is more photosensitive have yielded conflicting results [*Guerrero and Jones*, 1996a; *Lomas and Lipschultz*, 2006]. This relative sensitivity has particular relevance for theories regarding the source of primary nitrite maximum, typically found around the 0.1-0.2% light level at the base of euphotic zone [*Lomas and Lipschultz*, 2006]. More recently, it has been demonstrated that the nitrification does occur at low but measurable rates in the photic zone [*Lipschultz*, 2001; *Raimbault et al.*, 1999; *Ward*, 1987]. It has also been shown that light-inhibition of ammonium oxidation is inversely proportional to the ammonium-oxidation rate and that estuarine strains of AOB are less photosensitive than are pelagic strains [*Horrigan and Springer*, 1990]. The importance of these details should not be overlooked, as the significance of photoinhibition of nitrification may play an important role in regulating N-cycling under proposed conditions of photic-zone euxinia during the early Proterozoic and later in the geologic record [*Brocks and Schaeffer*, 2008; *Grice et al.*, 2005; *Pancost et al.*, 2002; *Pancost et al.*, 2004]. For lack of more detailed understanding, photoinhibition of nitrification is currently specified in the ICBM as a user-defined flag in the range 0-1, which directly scales the maximum rates of nitrification in the surface layer. By default, it is set to zero, consistent with earlier arguments for complete photoinhibition of nitrification in the photic zone.

3.7 *Anaerobic Ammonium Oxidation*

Anaerobic ammonium oxidation (anammox) was first predicted by [*Richards*, 1965], however it was only first demonstrated in the early 1990's in a wastewater treatment plant in Delft, Netherlands [*van de Graaf et al.*, 1990]. The first evidence for anammox in the natural environment came from Baltic marine sediments [*Thamdrup and Dalsgaard*, 2000]. Now eight years later, anammox is understood to be a major pathway of fixed-N loss in marine sediments and pelagic anoxic zones, possibly accounting for as much as 50% of total fixed-N loss [*Dalsgaard et al.*, 2005].

Isotope ^{15}N labeling has shown that the anammox process is represented by the reaction [*Mulder et al.*, 1995; *van de Graaf et al.*, 1995]:

$$NO_2^- + NH_4^+ \rightarrow N_2 + 2H_2O \qquad 3\text{-}29$$

It is only known to be carried out by members of the order *Planctomycetales* [*Strous et al.*, 1999]. Like nitrifiers, the main mode of anammox growth appears to chemolithoautotrophy [*Strous et al.*, 1999], however genome-sequencing and laboratory results have recently shown that anammox bacteria are potentially quite versatile, capable of utilizing formate to reduce both manganese and iron oxides, oxidizing iron with nitrate, and performing dissimilatory nitrate reduction to ammonium (DNRA) via nitrite as a free intermediate [*Kartal et al.*, 2007; *Strous et al.*, 2006]. These additional abilities have yet to be observed *in situ* and little is known about their occurrence, so they have not been included in the present version of the model.

Like nitrification, the canonical balanced redox equation for anammox does not include a term for carbon fixation. Based on the observed stoichiometry of anammox in a fluidized bed reactor, [*van de Graaf et al.*, 1996] proposed that carbon fixation is coupled to the oxidation of nitrite in anammox bacteria via:

$$2NO_2^- + CO_2 + H_2O \rightarrow 2NO_3^- + CH_2O \qquad 3\text{-}30$$

which would explain the observed excess consumption nitrite and production of nitrate. Assuming a ratio of 0.07 mol C fixed/mol NH_4^+ oxidized [*Strous and Jetten*, 2004], it is possible to write a balanced whole organism redox equation:

$$16NO_2^- + 14NH_4^+ + CO_2 \rightarrow 14N_2 + 2NO_3^- + CH_2O + 27H_2O \qquad 3\text{-}31$$

which is generally similar to the overall stoichiometry suggested by [*van de Graaf et al.*, 1996]:

$$30.8NO_2^- + 23.5NH_4^+ + CO_2 \rightarrow 24.6N_2 + 5.2NO_3^- + CH_2O + 44H_2O + 5.2OH^- \qquad 3\text{-}32$$

Following [*Koch et al.*, 2000], the kinetics of this reaction are simulated using a double Monod expression with an additional inhibition term for O_2:

$$\frac{\partial AMX}{\partial t} = \mu_{AMX} \cdot \frac{NH_4^+}{K_{NH_4}^{AMX} + NH_4^+} \cdot \frac{NO_2^-}{K_{NO_2}^{AMX} + NO_2^-} \cdot \frac{K_{O_2}^{AMX}}{K_{O_2}^{AMX} + O_2} \cdot AMX \text{ - mortality} \qquad 3\text{-}33$$

where AMX is the population density of anammox bacteria, μ is the maximum growth rate in $year^{-1}$, K_{NO2} and K_{NH4} are half-saturation constants, and K_{O2} is the inhibition constant. Parameters for this expression have been drawn from the available literature, composed entirely of laboratory measurements on enrichment cultures and cross-checked with physically purified cells of Candidatus "Brocadia anammoxidans" [*Jetten et al.*, 2001]. While the growth of *Candidatus "B. anammoxidans"* and *Candidatus "K. stuttgartiensis"* is cell density dependent [*Strous and Jetten*, 2004], anammox bacteria in the Black Sea appear as single cells [*Kuypers et al.*, 2003]. Despite this difference, the cell-specific activities of laboratory and *in situ* Black Sea strains appear to be consistent [*Strous and Jetten*, 2004]. Similar to the nitrification model, the code employs one additional Monod term for phosphate uptake in Redfield proportions with a very low half-saturation value (0.03 μmol kg^{-1}) which is not shown above. This insures numerically stability under extremely low phosphate conditions and is not expected to have any effect in typical simulations.

3.8 *Bacterial Mortality and Endogensis Metabolism*

Perhaps one of the most important and least well understood aspects of marine biogeochemistry is the form of the microbial biomass loss term (mortality plus endogensis metabolism). To illustrate this point, consider the following the following thought experiment. A simple chemostat is set up with a constant rate of inflow and outflow governed by an overflow. The concentration of the component of interest in the inflow is varied. Five cases will be examined for the reaction term:

1) Linear Rate Law

2) Michaelis-Menton (Saturation) Law

3) Monod Law with no Mortality (only dilution)

4) Monod Law with Linear Mortality

5) Monod Law with Quadratic Mortality

The corresponding model differential equations are:

$$1)\ \frac{\partial C}{\partial t} = \delta\left(C_{Inflow} - C\right) - k \cdot C$$

$$2)\ \frac{\partial C}{\partial t} = \delta\left(C_{Inflow} - C\right) - k \cdot \frac{C}{C + C_H}$$

$$3)\ \frac{\partial C}{\partial t} = \delta\left(C_{Inflow} - C\right) - k \cdot \frac{C}{C + C_H} \cdot X; \qquad \frac{\partial X}{\partial t} = -\delta \cdot X + k \cdot \frac{C}{C + C_H} \cdot X \qquad \text{3-34}$$

$$4)\ \frac{\partial C}{\partial t} = \delta\left(C_{Inflow} - C\right) - k \cdot \frac{C}{C + C_H} \cdot X; \qquad \frac{\partial X}{\partial t} = -\delta \cdot X + k \cdot \frac{C}{C + C_H} \cdot X - m \cdot X$$

$$5)\ \frac{\partial C}{\partial t} = \delta\left(C_{Inflow} - C\right) - k \cdot \frac{C}{C + C_H} \cdot X; \qquad \frac{\partial X}{\partial t} = -\delta \cdot X + k \cdot \frac{C}{C + C_H} \cdot X - m \cdot X^2$$

where C is the concentration of the component of interest; X is the population of microbes carrying out the reaction (in units of C) where applicable; C_{Inflow} is the concentration of the component in the inflow; δ is the dilution rate (reactor volume/inflow rate); k is a first order rate constant; C_H is a half-saturation constant in units of C; and m is a mortality coefficient. The steady state solutions are shown in Figure 3.2 for each case.

Clearly, the solutions are very sensitive to the models' underlying assumptions. Compared to the linear case, the Monod models initially result in much lower substrate concentrations for a given loading (i.e. source). The Monod models with only dilution or first-order mortality responded to increasing source strength by linearly increasing the population size, thus holding the steady state concentration to a term proportional to the half-saturation constant. Initially, the Monod term with quadratic mortality behaves similarly for low loadings, but this response is overcome has the rate of mortality

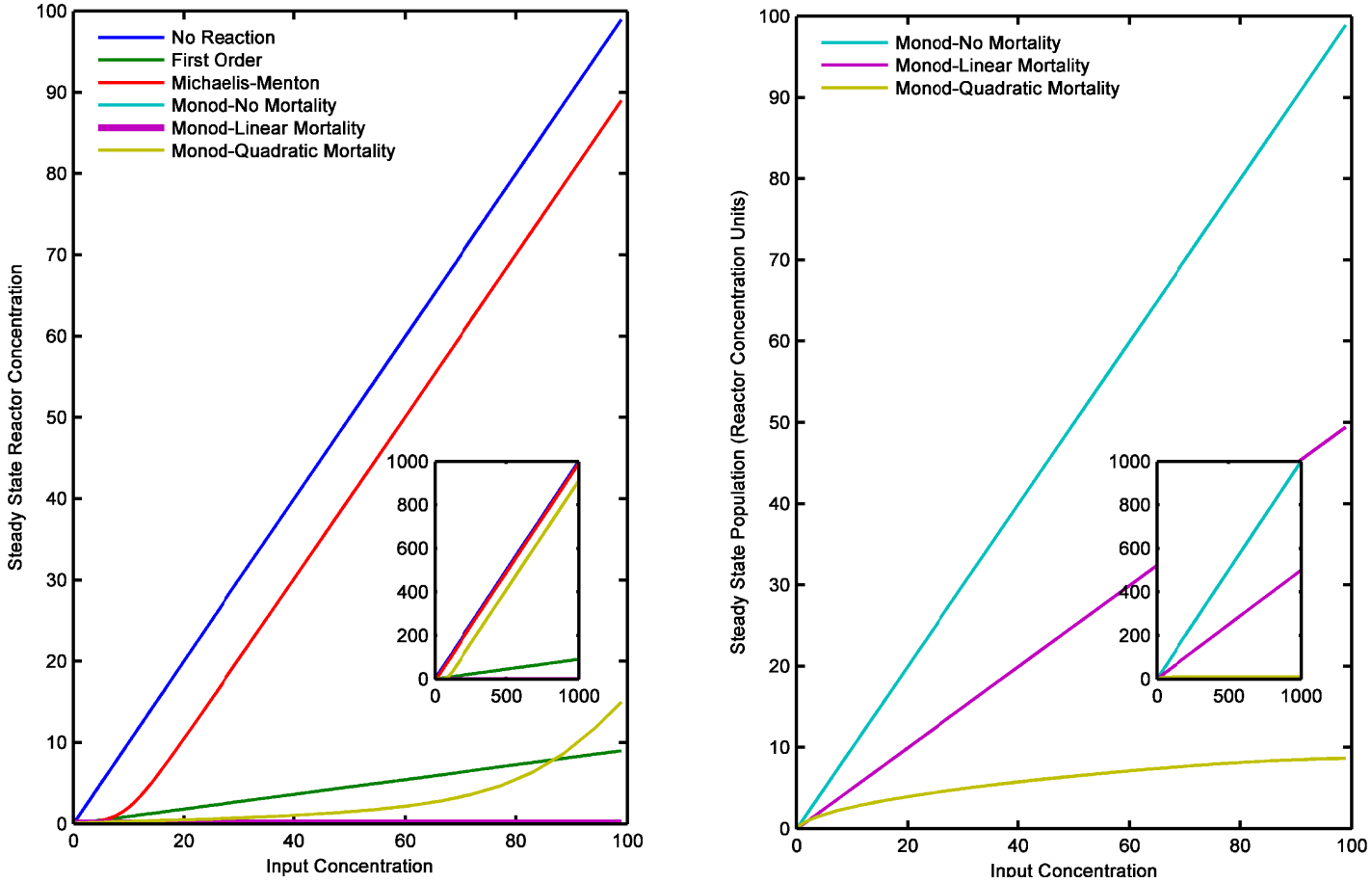

Figure 3.2. Phase portraits of steady state solutions to simple chemostats using a range of models for microbial biomass and bacterial mortality (Equation 3-34). The solutions depict a wide range of qualitative behaviors, demonstrating the potential importance of choosing reasonable models for microbial biomass and mortality.

becomes large and the population stabilizes. Thus, under high loadings the Monod model with quadratic mortality behaves like a zero-order rate law. While these results are not directly comparable to the full reaction-transport case, the results demonstrate that biogeochemical models which employ "simple" law rate laws may actually introduce a significant model bias compared to models that explicitly simulate microbial functional groups, and that explicit microbial models with different closure terms may also vary among themselves. It may be important in some cases to choose appropriate models for the microbial biomass and bacterial mortality.

Thus, rather than specifying a first-order or second-order closure term arbitrarily, the ICBM simulates microbial mortality following the empirical approach of [*Bendtsen et al.*, 2002], who assume a general form:

$$\text{mortality} = m \cdot B^n \tag{3-35}$$

where m and n are empirical constants and B is the microbial biomass. To determine appropriate values for the constants, [*Bendtsen et al.*, 2002] applied a simple model of carbon mass balance to measurements of particle flux and bacterial biomass in the central Pacific. At steady state, the rate of labile organic carbon supplied will equal the rate carbon oxidation and the corresponding rate of bacterial growth will equal the rate of mortality:

$$\begin{aligned} \frac{dB}{dt} &= 0 = \mu_{max} \cdot \alpha \cdot LDOC \cdot B - m \cdot B^n \\ \frac{dLDOC}{dt} &= 0 = D - \frac{1}{Y} \cdot \mu_{max} \cdot \alpha \cdot LDOC \cdot B + \varepsilon_{LDOC} \cdot m \cdot B^n \end{aligned} \tag{3-36}$$

where μ_{max} is the maximum growth rate, α is the substrate affinity, D is the allochthonous labile carbon supply, Y is the bacterial growth efficiency, and ε_{LDOC} is the community recycling efficiency of bacterial carbon. Solving for B, we find:

$$B = \sqrt[n]{\frac{D \cdot Y}{m \cdot (1 - Y \cdot \varepsilon_{LDOC})}} \tag{3-37}$$

the logarithm of which is of course a line:

$$\log B = \frac{1}{n}\log D + \frac{1}{n}\log\left(\frac{Y}{m\cdot\left(1 - Y\cdot\varepsilon_{LDOC}\right)}\right) \qquad 3\text{-}38$$

Below the euphotic zone, the principle supply of LDOC is the hydrolysis of sinking particulate matter. Therefore, we can use the divergence of the particle flux as the allochthonous labile carbon supply, D. Using the [*Martin et al.*, 1987] equation as a model for the observed particle flux:

$$\mathrm{D} = \mathrm{F}_{\mathrm{Corg}}^{\mathrm{Z_{mix}}}\cdot\frac{-0.86}{100}\cdot\left(\frac{\mathrm{Z} + \left(100 - \mathrm{Z_{mix}}\right)}{100}\right)^{-1.86} \qquad 3\text{-}39$$

Finally, to calculate m we must assume values of Y and $\varepsilon_{\mathrm{LDOC}}$. Estimates of the growth efficiency of marine bacterial heterotrophs vary widely from 0.02-0.50 [*del Giorgio and Duarte*, 2002], but Y = 0.24 is representative. While [*Bendtsen et al.*, 2002] uses a value of $\varepsilon_{\mathrm{LDOC}}$=.7, a value of 1 is used here, since all respiration is assumed to occur only via heterotrophic bacteria in the model. Using characteristic values for $\mathrm{F}_{\mathrm{Corg}}^{\mathrm{Z_{mix}}}$ of 1.53 mol C m^{-2} yr^{-1} [*Martin et al.*, 1987] and $\mathrm{B} = 6\cdot10^{10}\left(Z/1000\right)^{-0.9}$ cells/m^3 [Nagata et al., 2000], and a typical value for the conversion factor between cells and mass of carbon, υ_b=15 fg C/cell, yields optimal values for m = 0.71 (10^9 cells/L)$^{-1.07}$/yr and n = 2.07.

Alternatively, it is also possible to estimate the mortality function directly given independent estimates of microbial production and biomass, again assuming steady state:

$$\begin{aligned}\frac{\mathrm{dB}}{\mathrm{dt}} = 0 &= \mu_{\max}\cdot\alpha\cdot\mathrm{LDOC}\cdot\mathrm{B} - \mathrm{m}\cdot\mathrm{B}^{\mathrm{n}} \\ &= \mathrm{Production} - \mathrm{m}\cdot\mathrm{B}^{\mathrm{n}} \\ \log(\mathrm{Production}) &= \mathrm{n}\cdot\log(\mathrm{B}) + \log(\mathrm{m})\end{aligned} \qquad 3\text{-}40$$

Independent estimates of microbial heterotrophic production can be obtained by monitoring the incorporation of [^{3}H]-thymidine, [^{3}H]-leucine, or both. By this method, one avoids the need to estimate Y, D, and $\varepsilon_{\mathrm{LDOC}}$, at the expense of estimating a

conversion factor between radiolabel uptake and bacterial production. For leucine, this conversion factor is thought to be between 1.5-3 kg C (mol Leu)$^{-1}$, depending on the extent of intracellular isotope dilution [*Simon and Azam*, 1989].

This method was applied to eight sights in the Atlantic, Pacific, Indian and Mediterranean oceans where both bacterial abundance and production data were available (Figure 3.3, Table 3.2). These sites were selected on the basis of a large range of production and biomass (>10X) and small relative errors in bacterial counts and production measurements (generally < 25%). Sites that did not meet these criteria typically showed poor correlation of biomass and bacterial production. Despite very different assumptions, both methods suggest that the mortality term is close to quadratic (n = 1.4–2.1). The leading term is only poorly constrained. However, because of the additional geographic coverage of the second method, default values for the ICBM model are taken from the weighted mean estimate of the log-transformed variables for all points shown in Figure 3.3, yielding m = 13.45 (10^9 cells L^{-1})$^{-0.71}$ yr^{-1} and n = 1.71. Currently, the mortality model is applied to each population individually, since applying it aggregately quickly causes slower growing functional groups to go "extinct". However, it was calculated from bulk cell counts and production numbers, and thus it probably best reflects microbial heterotrophs which dominate the pelagic water column. More research is certainly warranted into the mortality rates of particular microbial species and function groups in the future.

3.9 *Inorganic Sulfur Reactions*

The current version of the ICBM sulfur cycle is limited to two species, SO_4^{2-} and H_2S, in a closed cycle. Neither inputs from rivers, hydrothermal vents, and submarine volcanism, nor outputs due to evaporite formation and sediment burial are simulated. It is implicitly assumed that these processes are at steady state and the mass of global marine sulfur reservoir can be specified as a constant variable.

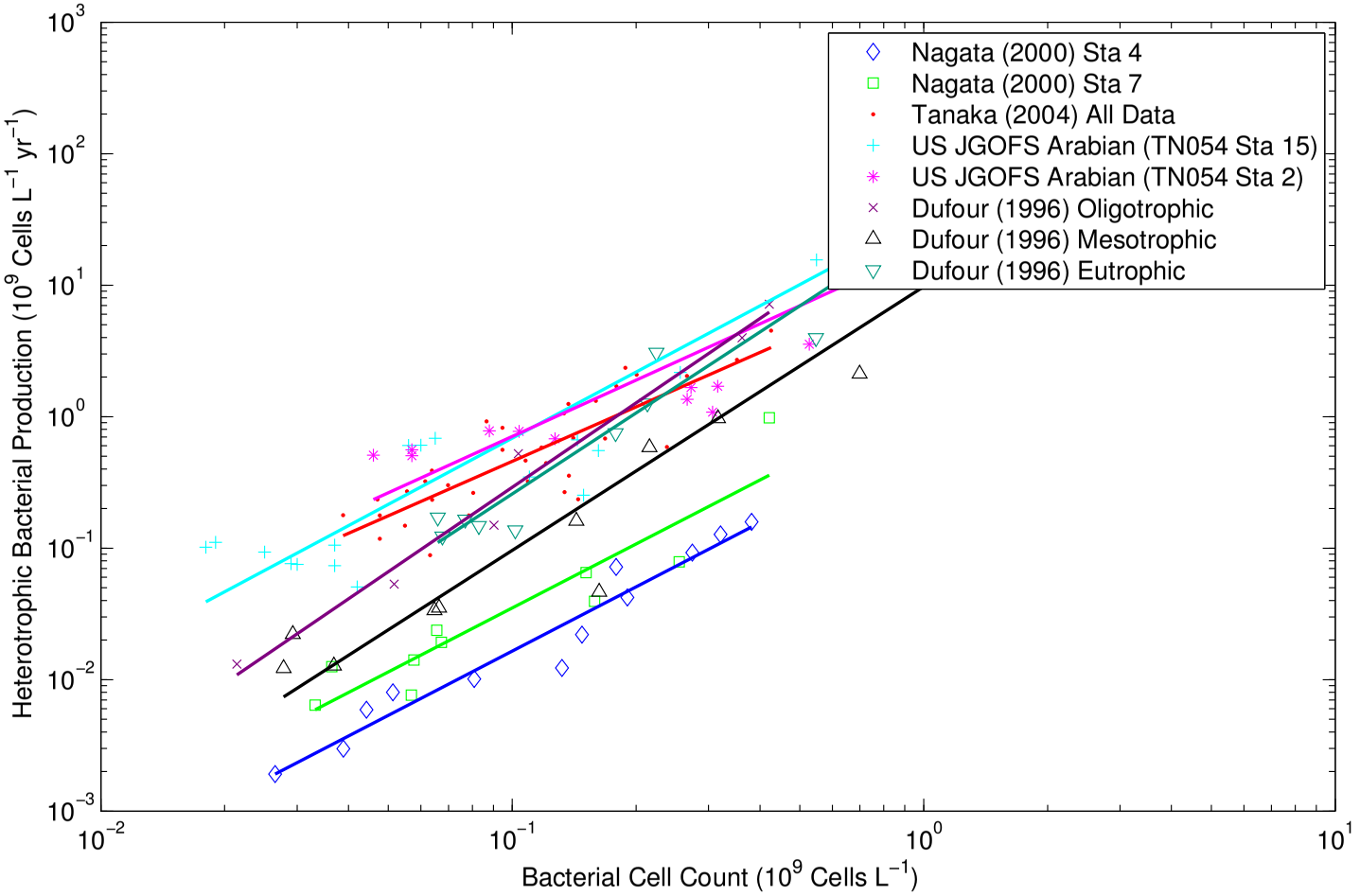

Figure 3.3. Log-log plot of bacterial production vs. bacterial cell count for several different datasets used to estimate the microbial mortality term using Equation 3-40. Results for each data set are provided in Table 3.2. See text for details.

Table 3.2. Sources of data and analysis of microbial mortality parameters using Equation 3-40. See text for details.

Author/Principle Investigator	Location	m $(10^9 \text{ cells } L^{-1})^{1-n} yr^{-1}$	n (unitless)	R^2
[*Nagata et al.*, 2000]	N. Pacific	0.7 +1.8/-0.5	1.6 +/- 0.6	0.95
[*Nagata et al.*, 2000]	N. Pacific	1.4 +25/-1.3	1.6 +/- 1.2	0.86
[*Tanaka and Rassoulzadegan*, 2004]	NW Med	11 +29/-7.9	1.4 +/- 0.6	0.70
[*Azam and Smith*, 2001]	Arabian	32 +64/-21	1.7 +/- 0.4	0.91
[*Azam and Smith*, 2001]	Arabian	18 +20/-10	1.4 +/- 0.4	0.91
[*Dufour and Torreton*, 1996]	Cape Verde	39 +986/-38	2.1 +/- 1.3	0.98
[*Dufour and Torreton*, 1996]	Cape Verde	9.7 +17/-6	2.0 +/- 0.5	0.96
[*Dufour and Torreton*, 1996]	Cape Verde	28 +39/-17	2.0 +/- 0.5	0.98

Sulfide is formed in the water column and sediments by heterotrophic sulfate reduction. Reoxidation of sulfide is simulated via two inorganic pathways. The first pathway is oxidation by molecular oxygen:

$$H_2S + 2O_2 \rightarrow 2H^+ + SO_4^{2-}$$
$$\frac{\partial H_2S}{\partial t} = -k_{H_2S} \cdot H_2S \cdot O_2 \qquad 3\text{-}41$$

The rate constant, k_{H_2S}, for this process has been shown to vary significantly as a function of several redox-sensitive trace metals which act as catalysts [*Millero*, 1991]. Here $k_{H_2S} = 54\ \mu\text{Mol}^{-1}\ \text{yr}^{-1}$ is equivalent to the 30 minute H_2S half-life observed for deep Black Sea samples exposed to air[*Millero*, 1991]. The second oxidation pathway is thiodenitrification as simulated by [*Konovalov et al.*, 2006]:

$$5H_2S + 8NO_3^- + \rightarrow 4N_2 + 5SO_4^{2-} + 4H_2O + 2H^+$$
$$\frac{\partial H_2S}{\partial t} = -k_{H_2S} \cdot H_2S \cdot NO_3^- \qquad 3\text{-}42$$

Thiodenitrification has been found to be biologically catalyzed in laboratory experiments [*Krishnakumar and Manilal*, 1999], as well as wastewater systems[*Yang et al.*, 2005]. In the environment, it is now also recognized to be carried out by *Beggiatoa sp*., *Thioploca* sp., and *Thiomargarita sp.* in marine and freshwater sediments[*Kamp et al.*, 2006; *Otte et al.*, 1999; *Schulz et al.*, 1999; *Sweerts et al.*, 1990], and has been reported in anoxic the water column of the Black Sea [*Tuttle and Jannasch*, 1973], Baltic [*Brettar and Rheinheimer*, 1991], and Namibian coast [*Lavik et al.*, 2006]. However, there appears to be little published information about the kinetics of this reaction in natural waters. Therefore, the same rate constant for aerobic oxidation of sulfide is assumed for now, though this is clearly subject to revision. Note that both of the reactions are modeled inorganically. Chemoautotrophic sulfur oxidation is an important omission, which should be explicitly included in a more detailed model of the sulfur cycle in the future.

3.10 *Sediment Model*

In each vertical level, the shoaling sediment surface intercepts a fraction of sinking particle export as given by the model hypsometry. This intercepted POM is instantaneously processed by the sediment submodel, which is composed of a series of parameterizations drawn from the literature. Carbon burial efficiency (CBE), the percent of total organic carbon flux which is ultimately buried, is calculated from the organic carbon rain rate following [*Dunne et al.*, 2007].

$$CBE = 0.013 + 0.53 \cdot \frac{F_{Corg}{}^{2}}{(7.0 + F_{Corg})^{2}} \qquad 3\text{-}43$$

where F_{Corg} is the flux of organic carbon delivered to the sediment surface in units of mmol C_{Org} m^{-2} d^{-1}. This equation was found to explain 66% of the variance in the available data [*Dunne et al.*, 2007].

Of the remineralized carbon (i.e. 1-CBE), a fraction, f_{Denit}, is remineralized via denitrification following the full metamodel of [*Middelburg et al.*, 1996]:

$$f_{\text{Denit}} = \frac{\text{Den}}{\text{F}_{\text{Corg}}} \qquad 3\text{-}44$$

$$\begin{aligned}\text{Log}(\text{Den}) = &\text{-}2.2567 - 0.1850 \cdot \log\left((1 - \text{CBE}) \cdot \text{F}_{\text{Corg}}\right) - 0.2210 \cdot \left[\log\left((1 - \text{CBE}) \cdot \text{F}_{\text{Corg}}\right)\right]^2 \\ &- 0.3995 \cdot \log\left(\text{NO}_3^-\right) \cdot \log\left(\text{O}_2\right) + 1.25 \cdot \log\left(\text{NO}_3^-\right) + 0.4721 \cdot \log\left(\text{O}_2\right) \qquad 3\text{-}45 \\ &- 0.0996 \cdot \log(\text{Z}) + 0.4256 \cdot \log\left((1 - \text{CBE}) \cdot \text{F}_{\text{Corg}}\right) \cdot \log\left(\text{O}_2\right)\end{aligned}$$

Because this equation was only calibrated from bottom water oxygen and nitrate concentrations of 10-350 µmol O2/kg and 1-60 µmol NO3-/kg respectively, the predicted contribution of denitrification to total remineralization can sometimes exceed 100% for BW O_2 < 10 µmol/kg in combination with high BW NO_3^- and low organic carbon flux. To prevent unreasonable values, f_{Denit} was scaled by:

$$f^*_{\text{Denit}} = 0.9 + \frac{\tanh\left(f_{\text{Denit}} - .9\right)}{10} \qquad \left(f_{\text{Denit}} > 0.9\right) \qquad 3\text{-}46$$

To estimate the fraction of denitrification coming from nitrification-denitrification, the remineralized fraction of benthic PON flux is estimated as:

$$f^N_{\text{Re min}} = 1 - \text{CBE} \cdot \frac{106}{16 \cdot C/N_{Burial}} \qquad 3\text{-}47$$

where C/N_{Burial}= 10 mole/mole, a typical value for marine sediments [Hedges et al., 1999]. Of the remineralized nitrogen, the fraction oxidized to nitrate in the sediments is simulated as:

$$f^N_{OX} = \frac{\text{O}_2}{\text{O}_2 + \text{K}_{\text{O}_2} + \text{k}_{\text{O}_2} \cdot (1 - \text{CBE}) \cdot \text{F}_{\text{Corg}}} \qquad 3\text{-}48$$

When the predicted nitrification is less than the total predicted denitrification, the difference in nitrate must coming from the overlying water column. This flux is limited according to:

$$f^N_{Diff} = \frac{\text{NO}_3^-}{\text{NO}_3^- + \min\left(\text{K}_{\text{NO}_3} + \text{k}_{\text{NO}_3} \cdot (1 - \text{CBE}) \cdot \text{F}_{\text{Corg}}, 0\right)} \qquad 3\text{-}49$$

Values for the constants, $K_{O_2} = 25\ \mu mol\ O_2\ kg^{-1}$, $k_{O_2} = 400\ \mu mol\ kg^{-1}$ (umol C cm^{-2} day^{-1}) $^{-1}$, $K_{NO_3} = 25\ \mu mol\ kg^{-1}$, and $k_{NO_3} = 10\ \mu mol\ NO_3^-\ kg^{-1}$ (umol C cm^{-2} day^{-1})$^{-1}$, where determined by fitting the simulated fluxes to those presented in [*Middelburg et al.*, 1996].

The remaining remineralization is modeled via aerobic respiration when the overlying water column is oxic (> 1 µmol kg^{-1} O_2), or sulfate reduction otherwise, with all sulfide being returned to the water column. In real sediments, the fraction of sulfide burial depends on the carbon flux and bioturbation [*Soetaert et al.*, 1996] and is related to the carbon burial efficiency [*Morse and Berner*, 1995].

Following the suggestions of previous authors [*Ingall and Jahnke*, 1997; *Ingall and Vancappellen*, 1990], we parameterize the C:P_{Reac} ratio of the organic matter burial flux as a function of bottom water dissolved oxygen (BW O_2) using:

$$C_{Org}/P_{Reac}\Big)_{Burial} = \frac{C_{Org}}{P_{Reac}}\Big)_{Burial}^{Oxic} + \frac{K_{PBE}}{K_{PBE} + BW\,O_2} \cdot \left[\frac{C_{Org}}{P_{Reac}}\Big)_{Burial}^{Anox} - \frac{C_{Org}}{P_{Reac}}\Big)_{Burial}^{Oxic} \right] \quad 3\text{-}50$$

where $C_{Org}/P_{Reac}{}^{Oxic} = 48.5$, $C_{Org}/P_{Reac}{}^{Anox} = 472$, and $K_{PBE} = 10$ µmol/kg. From the carbon burial flux, it is then possible to calculate the phosphorus burial flux. Unburied phosphorus is returned to the overlying water column. Note that the C_{Org}:P_{Reac} ratios used here are somewhat more extreme than the values proposed by [*Handoh and Lenton*, 2003] but bracket the range of C_{Org}:P_{Reac} ratios observed by Anderson et al (2001) for a variety of depositional environments (their Figure 3c). The shallowest downcore data reported by [*Anderson et al.*, 2001] correspond to approximately 2 mbsf and thus provide good estimate of the end product of early diagenesis.

SECTION 4

PROGRAM LAYOUT AND NUMERICAL METHODS

4.1 *Introduction to the Model Program*

This section provides an overview of the model implementation. The program is written entirely in MATLAB® 7.1 but should also be compatible with MATLAB 7.0 and later versions. The MATLAB language was intentionally chosen for its simplicity and readability, while providing access to powerful numerical routines and high level graphical output. The intent is to minimize barriers to potential new users, while maintaining reasonably fast computation. A full annotated version of the model source code is available upon request from the author.

Figure 4.1 provides an illustration of the program flow. The model is written with an emphasis on modularity, allowing individual components and processes to be easily added, modified, or replaced individually. For example, one might like to update the anammox submodule to reflect ongoing research into these organisms' metabolism and environmental kinetics. This can be done simply by modifying the code in the function `anammox.m`.

4.2 *Executing a Model Run*

A model run is executed by running the Solver script file (Figure 4.1). This script provides the initial conditions, model parameters, and numerical integration options to the solver. A separate parameter file provides the model geometry (reservoir depths, volumes, etc), circulation parameters, and selected biogeochemical parameters, which are passed as a structured array.

The numerical integration algorithm calls the Model function at least once during each time step. The Model function itself does only three things: inputs the state vector forming a matrix with each component in its own column, calls the `Circulation` and

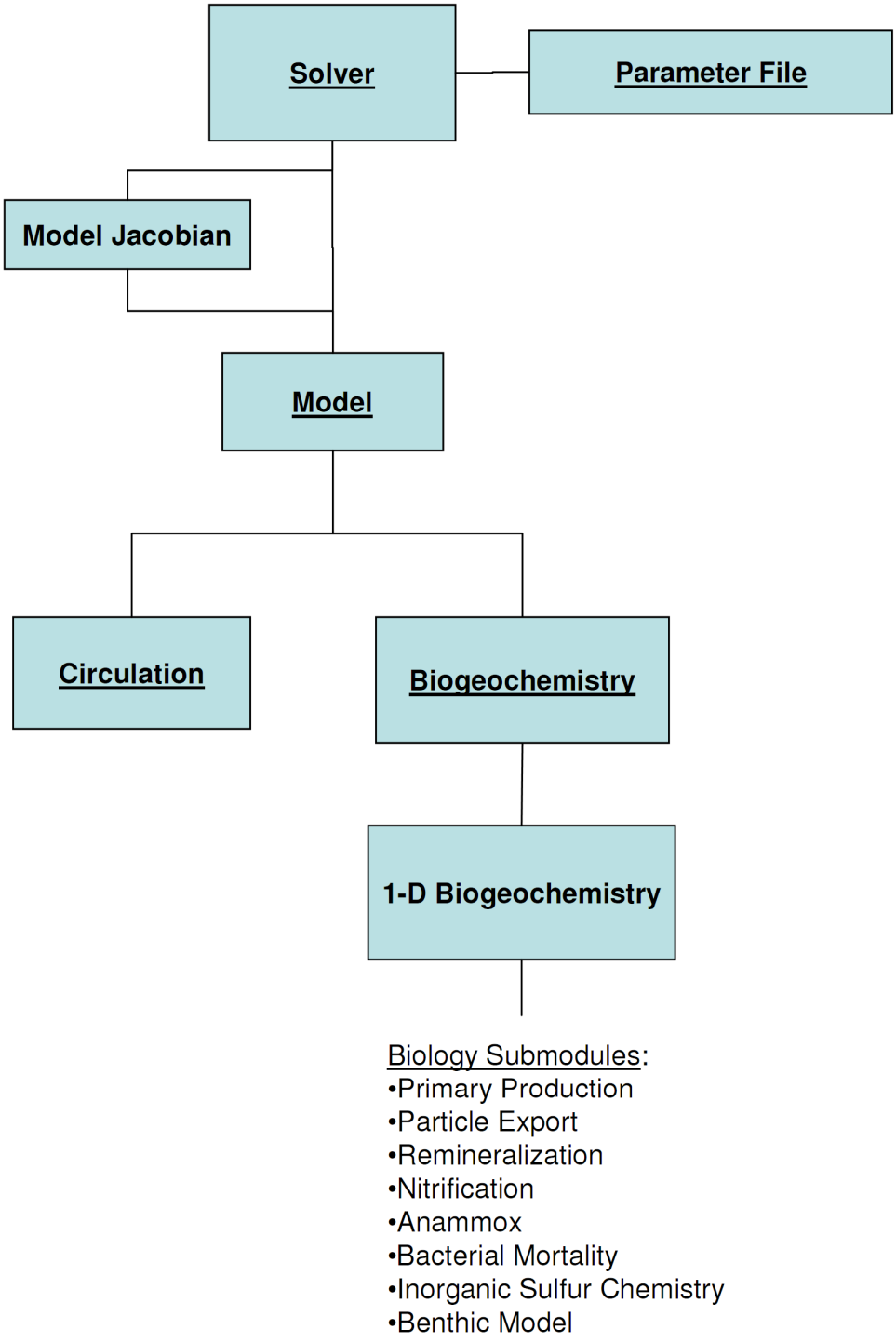

Figure 4.1 Model Overview emphasizing modularity of the code. Each name refers to a separate m-file.

`Biogeochemistry` submodels, and assembles and outputs the time derivative. The two submodels contain the body of the code. The `Circulation` function computes the conservative transport of all tracers, using the transportation matrix predefined in the `ParameterFile`. The `Biogeochemistry` function in turn calls `Biogeochemistry 1-D` once for each spatial region passing only the relevant elements of the state vector. `Biogeochemistry 1-D` calls the submodules (each a separate m-file) which describe the various biogeochemical processes under consideration, for example, primary production, particulate export and remineralization, nitrification, anammox, benthic processes, and so on. When the run is complete, the Solver script automatically saves the output and calls a user-supplied graphics routine to plot the output.

As discussed further in the numerical methods section below, the implicit numerical solver is occasionally required to calculate the model's Jacobian matrix during the integration process. To improve the solver performance, the sparse analytical Jacobian can be used in place of the default numerical approximation. This is done using the MAD autodifferentiation package from TomLAB® and by setting the 'Jacobian' option in `odeset` to a wrapper function, `Jacobian`, which initializes the current state vector as a MAD derivative object, calls the model, and then exacts the analytical Jacobian from the resulting derivative object automatically. In this way, the model can be changed arbitrarily without needing to update a hand-coded Jacobian function.

4.3 *Numerical Methods*

When solving the ICBM model, it is natural to view the problem as method of lines in the highly-resolved vertical direction, while laterally coupling the vertical 1-D regions uses the simple box model concept of exchange fluxes. The resulting system of ordinary differential equations (ODEs) can then be readily solved by employing an appropriate choice from among dozens of widely-available routines for solving ODE initial value problems.

Considering the ICBM as a series of vertical 1-D models, the general equation to be solved is:

$$\frac{\partial C}{\partial t} = \frac{\partial}{\partial z}\left(\kappa_Z A \frac{\partial C}{\partial z}\right) - \frac{\partial}{\partial z}(wAC) + \Phi_H + f(C(t,z)) \qquad 4\text{-}1$$

where C is a matrix of different component concentrations, z is the depth, κ_Z is the vertical eddy diffusivity, w is the vertical velocity, and A is the horizontal cross-sectional area. In general, κ_Z, w, and A all vary with depth. Φ_H is the divergence of the lateral transport, which couples different model regions. $f(C(t,z))$ is a nonlinear function representing the biogeochemistry in the water column and sediments.

The problem is discretized on a non-uniform vertical grid, and the diffusion and advection terms are approximated using the second-order center-difference (CD) and the first-order upwind difference (FUD) schemes respectively:

$$\frac{\partial}{\partial z}\left(\mathrm{K}_Z A \frac{\partial C}{\partial z}\right) = \frac{A_{i\text{-}1,i}\mathrm{K}_{Z,i\text{-}1,i}(C_{i-1} - C_i)}{0.5 \cdot V_i \cdot (h_{i-1} + h_i)} + \frac{A_{i,i+1}\mathrm{K}_{Z,i,\,i+1}(C_{i+1} - C_i)}{0.5 \cdot V_i \cdot (h_i + h_{i+1})} \qquad 4\text{-}2$$

$$-wA\frac{\partial C}{\partial z} = \begin{cases} \dfrac{w_{i\text{-}1,i}A_{i\text{-}1,i}}{\mathrm{V_i}}(C_{i-1} - C_i) & w \geq 0 \\ \dfrac{w_{i,i+1}A_{i,i+1}}{\mathrm{V_i}}(C_{i+1} - C_i) & w < 0 \end{cases} \qquad 4\text{-}3$$

where $\mathrm{V_i}$ is the volume (mass) of reservoir i, h_i is the depth thickness of reservoir i, and $A_{i\text{-}1,i}$ and $\mathrm{K}_{Z,i\text{-}1,i}$ denote the cross-sectional area and eddy diffusivity at the interface between reservoir i and reservoir i-1. The lateral exchange between adjacent 1-D regions is constructed in the familiar box-model fashion:

$$\Phi_H = \left.\frac{\partial C_i}{\partial t}\right)_{\text{Lateral Mixing}} = \sum_j Q_{ji}C_j - Q_{ij}C_i \qquad 4\text{-}4$$

where Q_{ij} is a flux from reservoir i to reservoir j. Equations 4-1 to 4-4 are combined into a single sparse transportation matrix (see Section 2 and Appendix B). The primary advantages of this finite volume scheme is that it conserves mass, is transportative

(disturbances only propagate downstream), is positive definite, and is extremely stable. Critically, because it is positive definite, it avoids spurious oscillations and negative concentrations under conditions of sharp gradients which are inherent in higher-order linear schemes (order 2 and greater). The main disadvantage of this approach is excess numerical diffusion due to the 2nd order truncation errors in the upwind advection scheme. In the ideal case (uniform grid, constant advection velocity, constant eddy diffusivity) the excess numerical diffusion is approximated to leading order by:

$$K_Z^N \approx \frac{w\Delta z}{2} \qquad 4\text{-}5$$

where w is the vertical velocity and Δz is the box thickness in the vertical. Compared to the ideal case, the size of the actual errors are larger than would be expected because of non-uniform cell spacing, variable advective velocity, and variable diffusivity which destroy fortuitous cancelation during the Talyor series derivation of the error estimate. However, numerical experiments demonstrated that additional error due to non-uniform grid spacing is likely to be of secondary importance when the variations in box width are small (not shown). The relative importance of K_Z^N relative to K_Z varies significantly with position in the model and model resolution. In the most highly resolved version of the global model used here (see Section 5), the numerical diffusivity calculated from Equation 4-5 ranges from 2-3% of K_Z in the gyre and high-latitude regions to about 50% of K_Z in the upwelling thermocline, driven by the large vertical velocity there. In the model of the Black Sea (see Section 6), the numerical diffusivity is less than 10% of the prescribed diffusivity with larger values at depth driven by larger box thicknesses. These errors, while not completely negligible, seem reasonable considering the factor of several uncertainty in literature estimates of diapycnal eddy diffusivity.

Spatial discretization results in a system of ordinary differential equations (ODEs) which are numerically integrated using the quasi-constant step, variable-order implicit

solver `ode15s` in the MatLab® 7.1 package. `Ode15s` is based on the numerical differentiation formulas (NDFs) which are similar to the backwards differentiation formulations (BDFs), also known as Gear's method, but permit slightly larger step-sizes for orders 1 through 3 (Ashino et al 2000, Shampine and Reichelt 1997). Because of their favorable stability properties when solving stiff chemical reaction equations, the BDFs and NDFs are two of the most commonly used numerical integration methods in chemistry applications [*Hundsdorfer and Verwer*, 2007]. The following paragraphs provide a brief overview of the BDFs and NDFs. The full details of these methods as implemented in ode15s can be found elsewhere [*Ashino et al.*, 2000; *Shampine*, 1994; *Shampine and Reichelt*, 1997; *Shampine*, 2005; *Shampine et al.*, 2005a].

The backward differentiation formulas are a subset of the linear multistep methods of numerical integration, which use linear combinations of the state vector and time derivatives at one or more past time steps to approximate the next time step. A simple example of the concept is provided in Appendix C, so only an overview will be provided here. In general, the linear k-step method is defined by the formula:

$$\sum_{j=0}^{k} \alpha_j w_{n+1+j-k} = \tau \sum_{j=0}^{k} \beta_j F\left(t_{n+1+j-k}, w_{n+1+j-k}\right) \qquad 4\text{-}6$$

where α_j and β_j are series of appropriately chosen constants which define the particular method, τ is the time step, $F(t,w)$ is vector function defining the ODE system, and w_n is the state vector at discrete time, t_n. Note that when, j = k, we are invoking the next time step, (t_{n+1}, w_{n+1}). Thus, when $\beta_k \neq 0,$ the method is implicit since the ODE system must be evaluated at the unknown state at the next time step.

The family of backwards differentiation formulas (BDFs) are then defined as linear multistep methods with:

$$\beta_k = 1, \quad \beta_j = 0, \quad (0 \leq j \leq k-1) \qquad 4\text{-}7$$

Since $\beta_k \neq 0$, they are implicit methods. This results in favorable stability properties when solving stiff systems of differential equations. Here, stiffness implies that one or more components of the solution change much more rapidly than other. One can rewrite the BDFs as:

$$\frac{1}{\tau}\sum_{j=0}^{k}\frac{\alpha_j}{\beta_k}w_{n+1+j-k} = F\left(t_{n+1}, w_{n+1}\right) \qquad 4\text{-}8$$

to show heuristically that the method's stability derives from forcing the backward difference approximation to the time derivative (LHS) to exactly equal the analytical ODE time derivative (RHS) evaluated at t_{n+1}. BDFs of order k=1 and k=2 are unconditionally stable for any choice of time step so long as the ODE function is bounded ("A-stable") [*Shampine and Reichelt*, 1997]. Higher order BDFs meet a slightly less rigorous stability condition ("A(α)-stability") requiring shorter time steps for some problems, but they are more accurate for any stable choice of time step [*Shampine and Reichelt*, 1997]. The sixth order BDF (BDF6) has a very narrow stability field and BDFs greater than order 6 are unconditionally unstable. `Ode15s` is based on methods of order 1 through 5 and automatically selects the highest order method which retains stability.

By default, the `ode15s` algorithm actually uses a slight variant of the BDFs known as the numerical differentiation formulas (NDFs). NDFs are very similar to BDFs and share all of the same favorable properties. For comparison with BDFs (Equation 4-8), NDFs are defined by the equation:

$$\frac{1}{\tau}\left[\sum_{j=0}^{k}\frac{\alpha_j}{\beta_k}w_{n+1+j-k} - \kappa\gamma_k\left(w_{n+1} - w_{n+1}^{(0)}\right)\right] = F\left(t_{n+1}, w_{n+1}\right) \qquad 4\text{-}9$$

where κ is a scalar constant and the coefficient $\gamma_k = \sum_{j=1}^{k} 1/j$. The κ term is added to control the leading term in the BDF truncation error. According to[*Shampine and Reichelt*, 1997], for any value of κ the NDF method is at of order k and the leading term in the truncation error is:

$$\left(\kappa\gamma_k + \frac{1}{k+1}\right)\tau^{k+1} y^{(k+1)} \qquad 4\text{-}10$$

By changing κ, it is therefore possible to choose an advantageous balance between accuracy and stability [*Pelios and Klopfens*, 1972]. For example, the first-order NDF (NDF1):

$$y_{n+1} - y_n - \kappa\left(y_{n+1} - 2y_n + y_{n-1}\right) = \tau \cdot F\left(t_{n+1}, y_{n+1}\right) \qquad 4\text{-}11$$

with $\kappa = -0.1850$, can take steps 26% larger than BDF1 while yielding the same accuracy [*Shampine and Reichelt*, 1997].

Because the BDFs and NDFs are implicit methods, the algorithm requires solving a (generally non-linear) system of equations for w_{n+1} at each time step. This is done by means of a simplified Newton iteration, beginning with the predicted value:

$$w_{n+1}^{(0)} = w_n + \sum_{m=0}^{k} \frac{\alpha_m}{\beta_k} w_{n+m-k} \qquad 4\text{-}12$$

Since the update to the Newton iteration requires the local derivative of the ODE with respect to each element in the state vector, the efficiency of the integration algorithm critically depends on the ability to inexpensively provide the Jacobian of the ODE function or a close approximation. Moreover, performance and storage gains can be obtained by specifying the sparsity of the Jacobian, since this reduces the work required to solve the system of linear equations for the correction to the current Newton iterate. By default, the MATLAB stiff ODE solvers employ a finite difference algorithm, `numjac`, to compute the full Jacobian. This is inefficient however, since the Jacobian matrix is rarely full, but in the absence of other information it is the only option. `Ode15s` also includes options to provide the analytical Jacobian or the Jacobian sparsity pattern, but for large systems of ODEs, hand-coding either of these options is so time-consuming and error-prone to make it impractical for almost all applications. Instead, it is possible to automatically calculate the sparse analytical Jacobian using the model source code and the

TOMOPT® MatLab Automatic Differentiation (MAD) package [*Forth*, 2006; *Forth and Edvall*, 2007]. The MAD package automatically evaluates the analytical Jacobian of the ICBM model by forward-mode operator overloading. Basically, the MAD package contains a library of functions and their derivatives which replace the default MatLab operators whenever one of the function arguments is of the "fmad" derivative-object class. Thus, the derivative of arbitrary MatLab code can be calculated by employing the chain rule on a line-by-line basis. A simple wrapper consisting of less then ten lines of MatLab code contained in the `Jacobian` function allows `ode15s` to call the MAD-enabled ODE function to compute the Jacobian whenever necessary, with no other user input. This method is approximately twice as efficient as using the default finite-differencing and is competitive with finite-differencing even when supplied with the Jacobian sparsity [*Forth and Edvall*, 2007].

SECTION 5

SIMULATION OF THE MODERN GLOBAL OCEAN

5.1 *Introduction to the Global Ocean Model Validation*

Can intermediate complexity box models coupled with process-based biogeochemistry reproduce the observed features of widely disparate modern environments? To test the ICBM model biogeochemistry over a wide range of conditions, the model was validated for both the modern Global Ocean and Black Sea, changing only the physical transport model and bathymetry. In this section, we focus first on developing a circulation model specifically for the modern Global Ocean and then on the results of coupled circulation-biogeochemistry integrations. Section 6 presents similar results for the Black Sea.

5.2 *Global Ocean Model Structure*

This section builds on the data and conceptual outline presented in Section 2. The global model used here consists of three spatial regions, the high-latitude ocean, the low-latitude ocean gyres, and a coastal upwelling zone (Figure 5.4). The area of upwelling zone is taken to be that of the modern suboxic region of the ocean, defined as where the minimum water column oxygen concentration is less than 10 μmol kg^{-1} using the World Ocean Atlas 2005 dataset [*Garcia et al.*, 2006a; b; *Locarnini et al.*, 2006]. Similarly, the extent of the high latitude ocean is based on modern regions of deepwater formation, defined as areas where the annual mean surface temperature is below 4°C. In the Northern Hemisphere, the extent of the high latitude region was further cropped to the North Atlantic, excluding the Arctic Ocean, Hudson Bay, and the Bering Sea (Figure 5.1). Each spatial region is then subdivided vertically into a column of boxes, with high resolution in the upper 1000 m and courser resolution at depth. Each vertical level is chosen to correspond to a particular neutral density level that can be traced across all three spatial

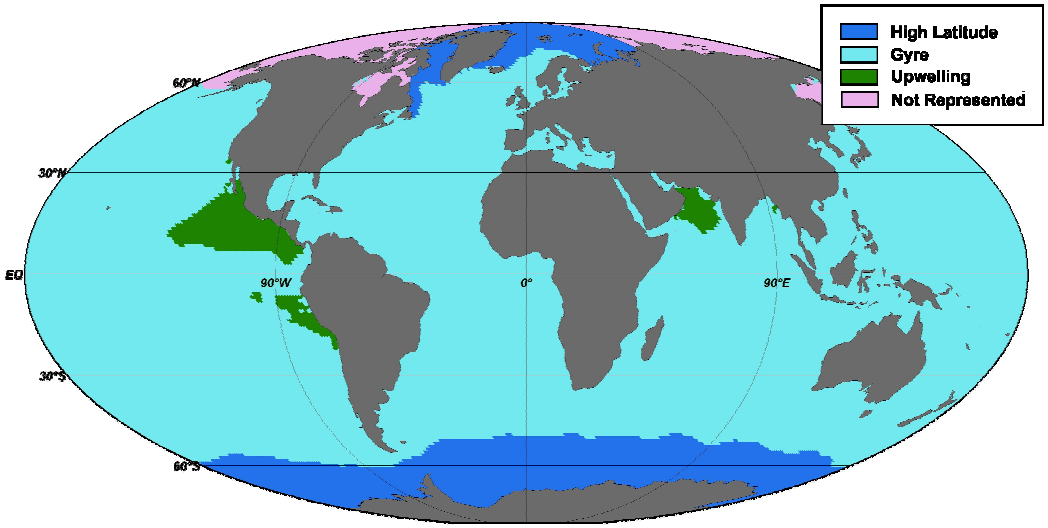

Figure 5.1. Map used to calculate the surface area of each region in the global ICBM model. High-latitude regions are defined by the SST = 4°C isotherm, excluding the Arctic Ocean, Hudson Bay, and Bering Sea. The upwelling regions are defined by the 10 µmol kg^{-1} O_2 contour at the depth of minimum water column oxygen. Note that the ICBM model represents only one region of each type, using the aggregate observed surface area.

regions, ensuring that flow between spatial regions follows realistic isopycnal pathways. To test the model's sensitivity to varying vertical resolution, the results from both a low-resolution and high-resolution model are presented. For each model region, it is necessary to specify the benthic hypsometry which defines the cross-section area, volume, and sediment surface area associated with each reservoir. The regional hypsometry was calculated from the ETOPO2v2 2' global bathymetry [*U.S. Department of Commerce*, 2006] for the regions indicated in Figure 5.1, and the results are presented in Figure 5.2.

5.3 *Global Model Boundary Conditions and Spin-up*

Surface gas fluxes were computed using the Wanninkhof (1992) U^2 relationship, using an annually- and spatially-averaged mean oceanic squared wind speed of 75 m^2/s^2 as calculated from the Quickscat climatology [*Risien and Chelton*, 2008]. The

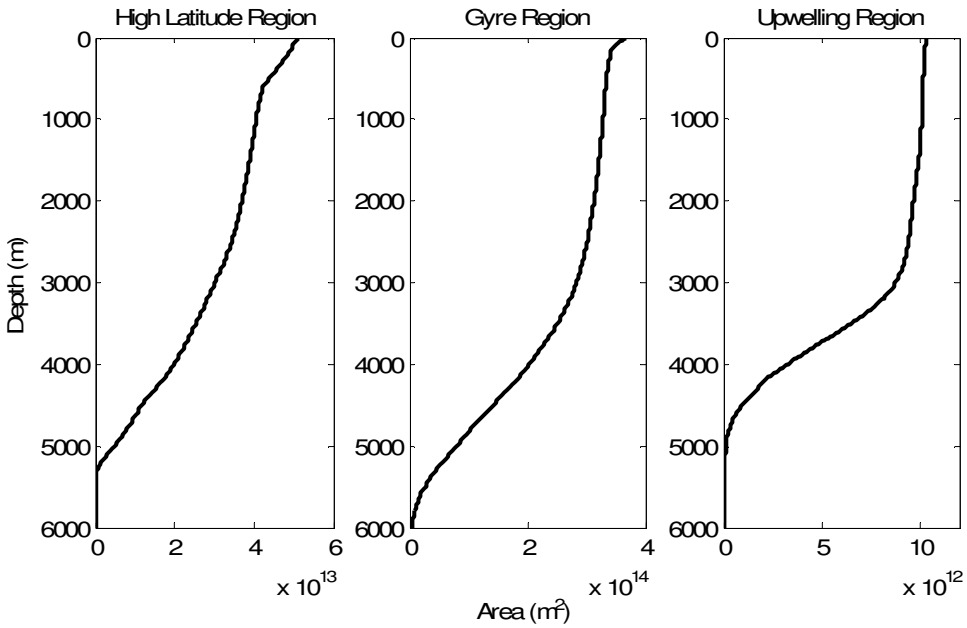

Figure 5.2. ETOPO2v2-derived hypsometric curves for each region classification shown in Figure 5.1. Note the different scales in each panel.

temperatures of the surface boxes in the high latitude, gyre, and upwelling regions were fixed at -1°C, 20°C, and 25°C, respectively. A constant sea surface salinity of 35 was used for calculating gas saturation in all regions. Mean surface alkalinity for the high latitude, gyre, and upwelling regions were fixed at the spatially-weighted mean values from the GLODAP database, 2300 µmol/kg, 2325 µmol/kg, 2280 µmol/kg respectively for all runs.Validation model runs were carried out in two steps. First, a 100ky spin-up was conducted to bring all components to steady state. During this step, preanthropogenic P_{CO2} (280 ppmv) and atmospheric $\Delta^{14}C$ (0 ‰) were used to calculate the simulated background $\Delta^{14}C$. During the second step, the spin-up integration was extended by 300 years (corresponding to the period 1700-2000) to further validate the model's transport of bomb radiocarbon and CFC-11. During this integration, the model was forced with the observed atmospheric pCO_2, pCFC-11, and $\Delta^{14}C$ values shown in Figure 5.3. For both integrations, external inputs of phosphate and nitrogen (as nitrate) were initially taken as in Tyrell (1999), 7.22×10^{10} and 4.87×10^{12} moles yr^{-1}, respectively.

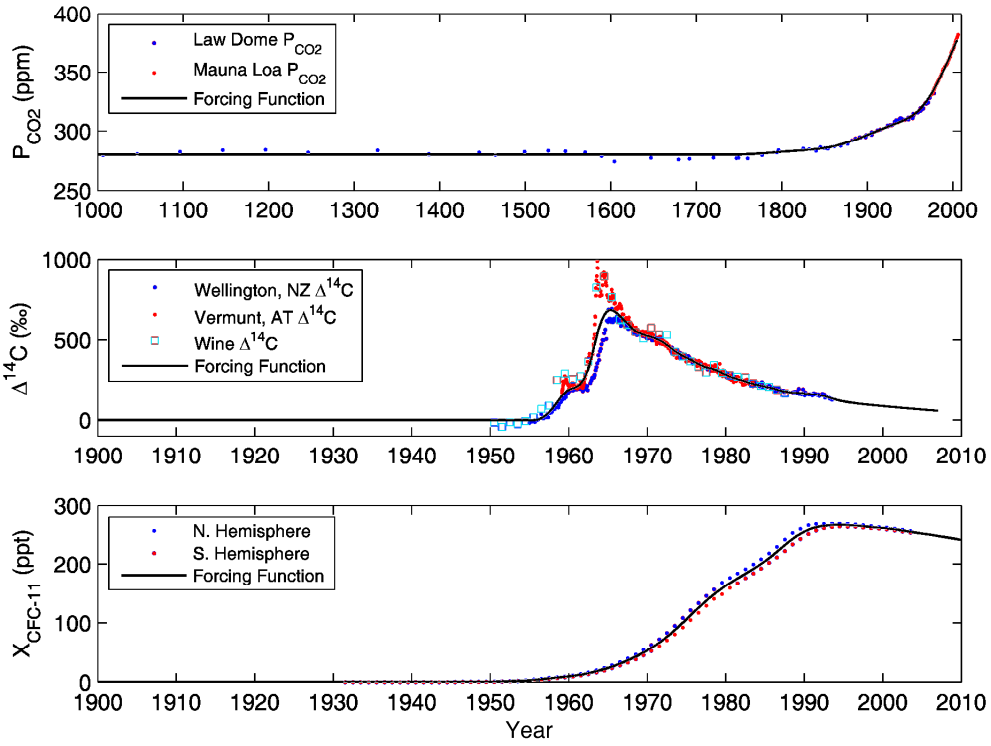

Figure 5.3. Atmospheric forcing functions for CFC-11 and bomb radiocarbon simulations. (Top) Atmospheric PCO2 forcing function derived from the Law Dome ice core and Mauna Loa atmospheric P_{CO2} data [*Etheridge et al.*, 1996; *Keeling and Whorf*, 2005]. (Middle) Atmospheric bomb $\delta^{14}C$ forcing function derived from measurements in Wellington, New Zealand, Vermunt, Austria, and Georgian wines [*Burchuladze et al.*, 1989; *Levin et al.*, 1994; *Manning and Melhuish*, 1994]. (Bottom) CFC-11 forcing derived from reconstructed northern and southern hemisphere atmospheric CFC-11 concentrations [*Walker et al.*, 2000].

However, preliminary experiments suggested that this level of phosphorus input would be insufficient to support observed levels of primary production given simulated rates of P-burial. The allochthonous input of phosphate was therefore adjusted upward to 15×10^{10} moles yr^{-1}. The new adjusted value is still within the estimated ranges of preanthropogenic riverine and atmospheric inputs of reactive P inputs to the ocean (4-16×10^{10} moles yr^{-1} [*Benitez-Nelson*, 2000]) and P-burial in oceanic sediments (5-21×10^{10} moles yr^{-1}, see Table 5.6).

5.4 *13-box Model of the Modern Global Ocean*

For illustration purposes, it is useful to first construct a 13-box model of global ocean circulation (Figure 5.4). The model's vertical levels were chosen to correspond to particular density surfaces, which can be traced between geographic regions to define isopycnal circulation pathways (Table 5.1). The advective circulation simulates the major features of the modern meridional circulation while combining the northern and southern hemisphere regions of deepwater formation into a single "high-latitude" zone. From bottom to top, ventilation of the ocean gyres is considered to occur via four independent pathways: bottom water, deep water, intermediate water, and ventilation along shallow outcropping isopycnals. For the first three processes, ventilation rates are set at 17, 17, and 12 Sv respectively (Table 2.1, 1 Sv = 10^6 m^3/s). Ventilation of the gyre thermocline along outcropping isopycnals is set at 220 Sv based on CFC-derived estimates of transport [*Fine et al.*, 2001; *Sarmiento*, 1983a]. In the real ocean, this outcropping occurs mostly at mid-latitudes which are not well-represented by either the low-latitude gyre or high-latitude ICBM model regions. Instead, the model simulates ventilation of the gyre thermocline as combination of mixing with these two end-members, with 43% of the ventilation occurring with high-latitude surface reservoir and the remainder with the gyre surface reservoir. The global coastal upwelling flux is set at 18 Sv, based on the sum of estimates for the world's major coastal upwelling zones (Table 2.2). Diffusive mixing fluxes are as described in Section 2.3-2.4.

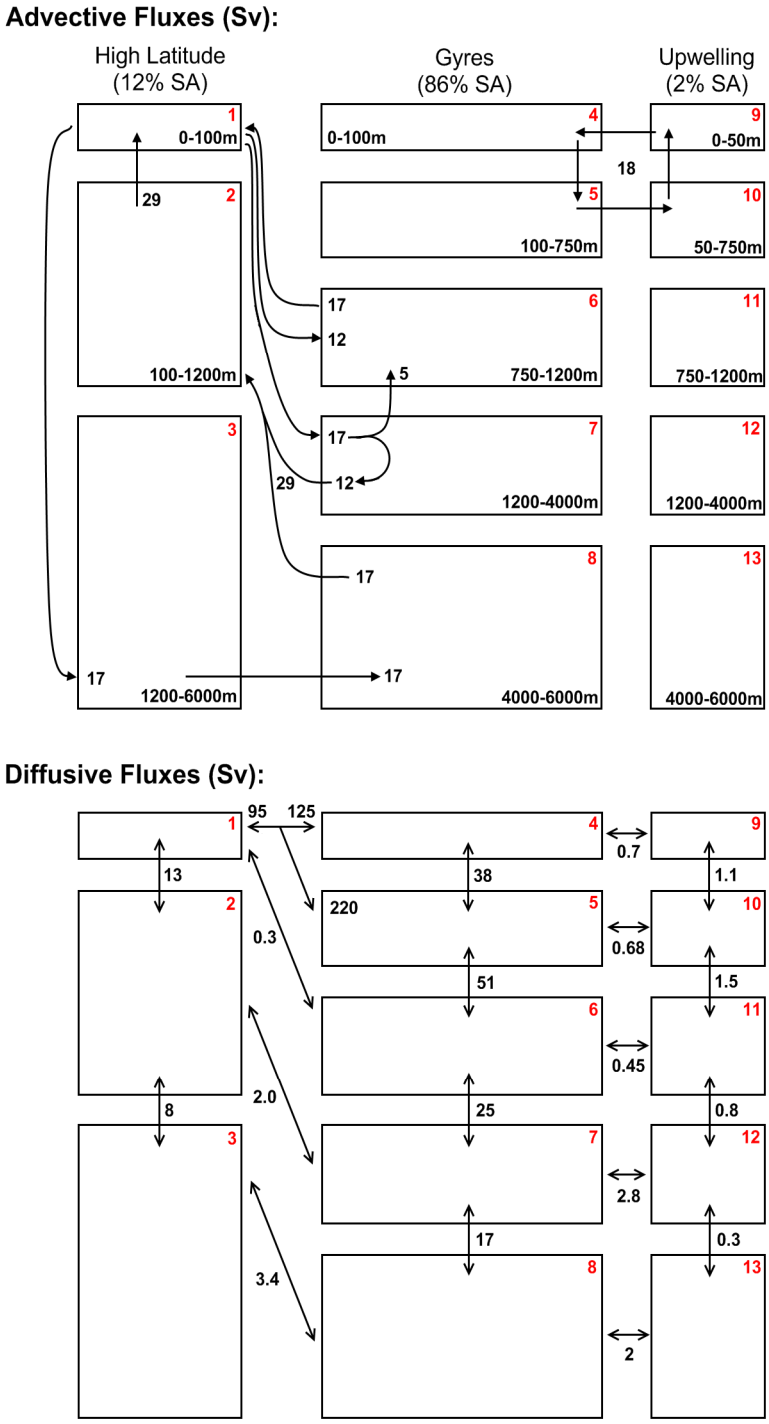

Figure 5.4. Schematic of the 13-box circulation. All fluxes are in Sverdrups (1 Sv = 10^6 m^3s^{-1}).

Table 5.1. Neutral density layers and water mass descriptions used to define vertical layers in each region of the 13-box model.

	Gyre		Upwelling		High Latitude	
Neutral Density	Interface Depth (m)	Water Mass	Interface Depth (m)	Water Mass	Interface Depth (m)	Water Mass
<24.74	0	Surface Water	0	Surface Water		
25.74	100	Thermocline	50	OMZ Core		
27.34	750	Intermediate Water	750	Intermediate Water	0	Polar Surface Water
27.65	1200	Deep Water	1200	Deep Water	100	Polar Deep Water
28.11	4000	Bottom Water	4000	Bottom Water	1200	Bottom Water
>28.14	6000		6000		6000	

5.5 *79-box Model of the Modern Global Ocean*

Sharp vertical redox gradients, such as those found in regions of intense coastal upwelling, are only crudely represented by the coarse resolution of the 13-box model. This may result in distortions of the steady state profiles and potentially large errors in the steady state fluxes. To examine the sensitivity of ICBM models to vertical resolution, a 79-box model was constructed by vertically subdividing the 13-box model. The new model has a vertical resolution of 50 meters in the upper 1000 meters, 100 meters between 1000-2000 meters, and 1000 meters below 2000 meters. The exact depth of each reservoir interface and the approximate corresponding neutral density surfaces for the 79-box model are provided in Table 5.2. Advective fluxes for the 79-box model were taken from the 13-box model, interpolated uniformly with depth. Diffusive mixing fluxes are as described in Section 2.3-2.4. Ventilation of the gyre thermocline (100-1000 meters)

Table 5.2. Neutral density layers and water mass descriptions used to define vertical layers in each region of the 79-box model.

	Gyre		Upwelling		High Latitude	
Neutral Density	Interface Depth (m)	Water Mass	Interface Depth (m)	Water Mass	Interface Depth (m)	Water Mass
<24.74	0	Surface Water	0	Surface Water		
25.74	100		50			
26.17	150		75			
26.42	200		100			
26.60	250		150			
26.73	300		200			
26.83	350		350			
26.91	400	Thermocline	400	OMZ Core		
26.99	450		450			
27.07	500		500			
27.13	550		550			
27.19	600		600			
27.25	650		650			
27.30	700		700			
27.34	750		750		0	
27.39	800		800			
27.43	850		850			
27.47	900	Intermediate Water	900	Intermediate Water		Polar Surface Water
27.50	950		950			
27.54	1000		1000			
27.60	1100		1100			
27.65	1200		1200		100	
27.70	1300		1300		125	
27.74	1400		1400		143	
27.78	1500		1500		163	
27.82	1600		1600		184	Polar Deep Water
27.85	1700	Deep Water	1700	Deep Water	209	
27.88	1800		1800		238	
27.90	1900		1900		275	
27.92	2000		2000		312	
28.05	3000		3000		806	
28.11	4000		4000		1200	
28.14	5000	Bottom Water	5000	Bottom Water	1400	Bottom Water
>28.14	6000		6000		6000	

was distributed proportional to depth-dependent CFC-ventilation rates determined for the North Atlantic and Pacific Ocean [*Fine et al.*, 2001; *Sarmiento*, 1983a]. The fraction of high-latitude and gyre surface waters contributing to the ventilation of each layer was determined from the mixing ratio required to yield the global mean winter outcrop SST for the neutral density layers in Table 5.2. The total ventilation flux, mean winter outcrop temperature, and fraction of high-latitude contribution to the mixing are given in Table 5.3.

5.6 *Global Model Results*

Reference data for model validation were taken from the discrete bottle observations compiled for the GLODAP Data Atlas [*Sabine et al.*, 2005] corresponding to each of the regions in Figure 5.1. WOCE radiocarbon and CFC-11 observations were made between 1983 and 1997, but most observations date from 1992 to 1996 and are

Table 5.3. Gyre Outcrop Ventilation Parameters for the 79-box Model.

Gyre Vertical Level #	Depth (m)	Potential Density (kg/m^3)	Mean Winter Outcrop Temp. (°C)	Ventilation Flux (Sv)	High Latitude Contribution (%)
2	100-150	25.74-26.17	14.84	40	25
3	150-200	26.17-26.42	12.56	40	35
4	200-250	26.42-26.60	10.72	40	44
5	250-300	26.60-26.73	10.37	20	46
6	300-350	26.73-26.83	9.54	15	50
7	350-400	26.83-26.91	8.37	15	55
8	400-450	26.91-26.99	7.31	10	60
9	450-500	26.99-27.07	6.10	10	66
10	500-550	27.07-27.13	5.29	6	70
11	550-600	27.13-27.19	4.47	4	74
12	600-650	27.19-27.25	3.53	4	78
13	650-700	27.25-27.30	2.43	4	84
14	700-750	27.30-27.34	1.78	4	87
15	750-800	27.34-27.39	0.99	4	91
16	800-850	27.39-27.43	0.94	1	91
17	850-900	27.43-27.47	0.51	1	93
18	900-950	27.47-27.50	0.17	1	94
19	950-1000	27.50-27.54	-0.09	1	96

therefore compared directly with simulated results for 1994. Additional data on total organic carbon (TOC) [*Peltzer and Hansell*, 2001; *Peltzer*, 2002], dissolved organic carbon (DOC) [*Hansell and Carlson*, 1998], ammonium [*Codispoti*, 2000a; b], and heterotrophic bacterial cell counts [*Ducklow*, 2002a; b; *Farooq and Smith*, 2001] were drawn from the JGOFS AESOPS and Arabian Sea process studies as well as the HOT and BATS sites [*Karl*, 2008; *Knap et al.*, 2008]. AESOPS, Arabian and HOT/BATS data are compared to the model high latitude, upwelling, and gyre regions, respectively. The concentration of semi-labile DOC (SDOC) was determined by subtracting the mean TOC or DOC for depths greater than 2000 meters (42 μM) from all TOC or DOC observations [*Carlson and Ducklow*, 1995]. Since labile DOC and POC typically contribute 1-10 μM C to upper-ocean TOC, the estimates of semi-labile DOC derived from TOC data are most likely overestimated by 10-25%. DOC data was used whenever available to avoid this problem. Since TOC values can sometimes exceed 100 μM C during phytoplankton blooms, TOC-derived DOC values were cross-checked by subtracting observed POC from TOC whenever both measurements were available for the same samples, and TOC-derived SDOC data were discarded whenever estimated errors exceeded 10 uM. Finally, all data corresponding to each model region were binned by depth and presented as the frequency of observations within a given depth bin. This approach avoids explicitly averaging geographically-disparate observations (e.g. the North Atlantic and North Pacific radiocarbon) as has been done in previous similar box model studies [e.g. *Siegenthaler and Joos*, 1992].

5.6.1 *Circulation Tracers*

For both the 13- and 79-box models, simulated potential temperature and background radiocarbon generally agree well with observations (Figure 5.5). Simulated high-latitude background radiocarbon better approximates observations from the Southern Ocean (left field) than the North Atlantic (right field), consistent with the construction of

the model's high-latitude circulation. The simulated background radiocarbon for the ocean gyre regions (-156‰) is intermediate between observations in the deep Atlantic (-75‰ to -150‰) and Pacific (-150‰ to -250‰). In the upwelling region, the large deviation in the background radiocarbon reflects the inability of the current model to simultaneous simulate both the deep Atlantic and Pacific radiocarbon pools using a single gyre region. Presently, the major upwelling regions, the Northern and Southern Eastern Tropical Pacific and Arabian Sea, all reflect Indo-Pacific water mass ages at depth, while the model gyre and upwelling region reflect a mean value for the Atlantic and Pacific.

The model simulation of CFC-11 and bomb ^{14}C transient tracers is also quite good (Figure 5.5). The penetration of bomb radiocarbon into the high latitude region may be overestimated by 10-20‰, however the sparse geographic distribution of observations and an inherent 10‰ uncertainty in separating the background and bomb radiocarbon signals may also partially explain the discrepancy [*Rubin and Key*, 2002]. Simulated CFC-11 distributions show excellent agreement with observations.

5.6.2 *Nutrients, O_2, and DIC*

Model nutrient profiles are typically well within the range of observations (Figure 5.6-Figure 5.8), however the lower resolution model is clearly subject to overshooting in regions with sharp vertical gradients. In detail, dissolved nitrate and phosphate are more similar to observations from the Pacific and Southern Oceans. This is a consequence of limiting high-latitude phosphorus drawdown below 1.5 μM, which results in higher levels of performed nitrate and phosphate throughout the model. In the gyre region of the high-resolution model, simulated surface nitrate and phosphorus concentrations are 0.89 μM and 0.15 μM, giving a surface NO_3^-:PO_4^- ratio of 5.9. In upwelling regions, simulated surface nutrient concentrations are approximately twice as high, 1.8 μM and 0.38 μM respectively, while surface concentrations in high latitude region remain elevated, 23.46 μM and 1.62 μM, with a NO_3^-:PO_4^- ratio of 14.5. There are no significant differences

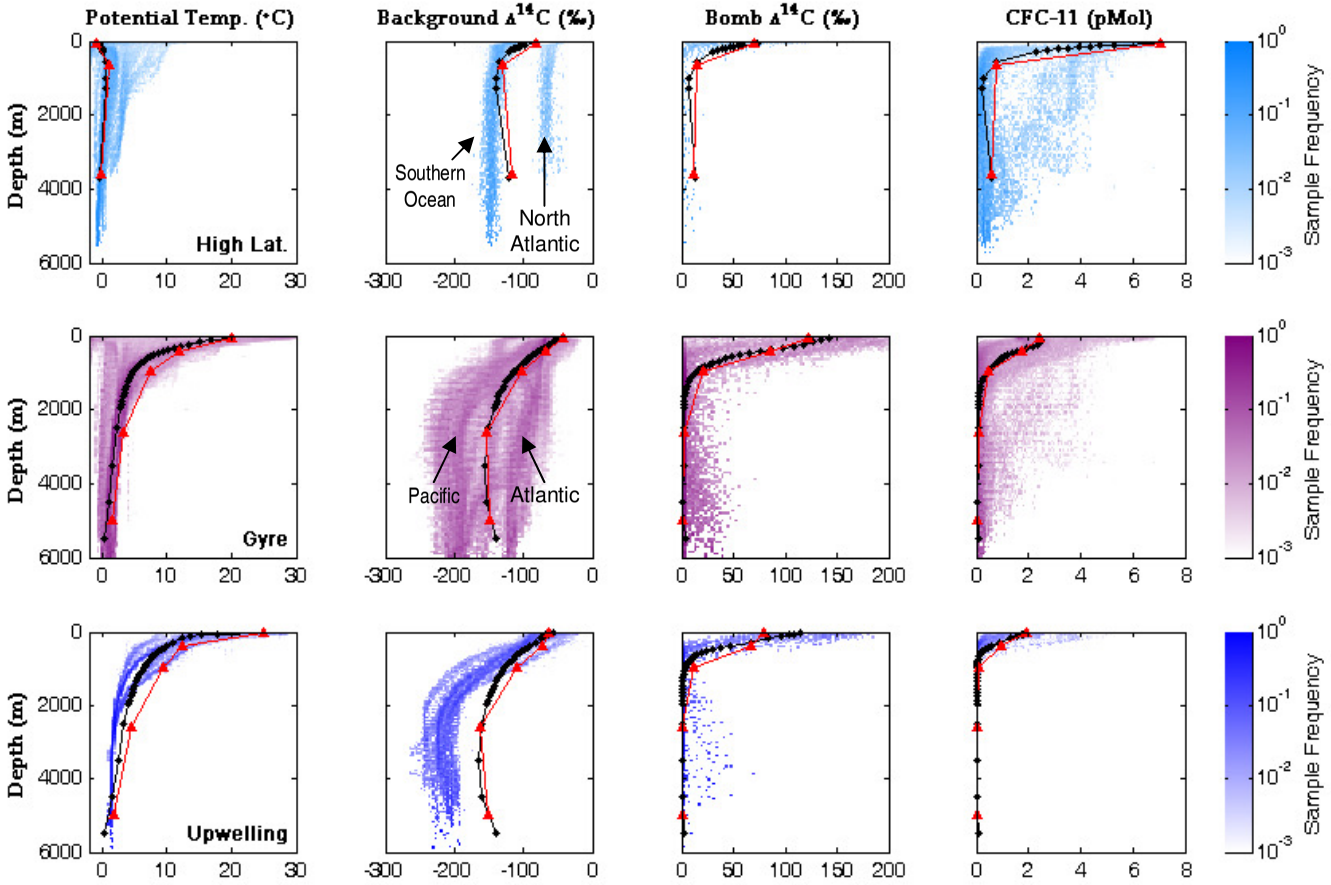

Figure 5.5. Simulated tracer profiles for the high-resolution (black) and low-resolution (red) Global Ocean ICBM model. Different rows correspond to the different geographic regions represented by the models. Data for validation was taken from the GLODAP database. Bimodal observations represent data from spatially distinct regions, such as the North Atlantic and Southern Ocean or Atlantic and Pacific.

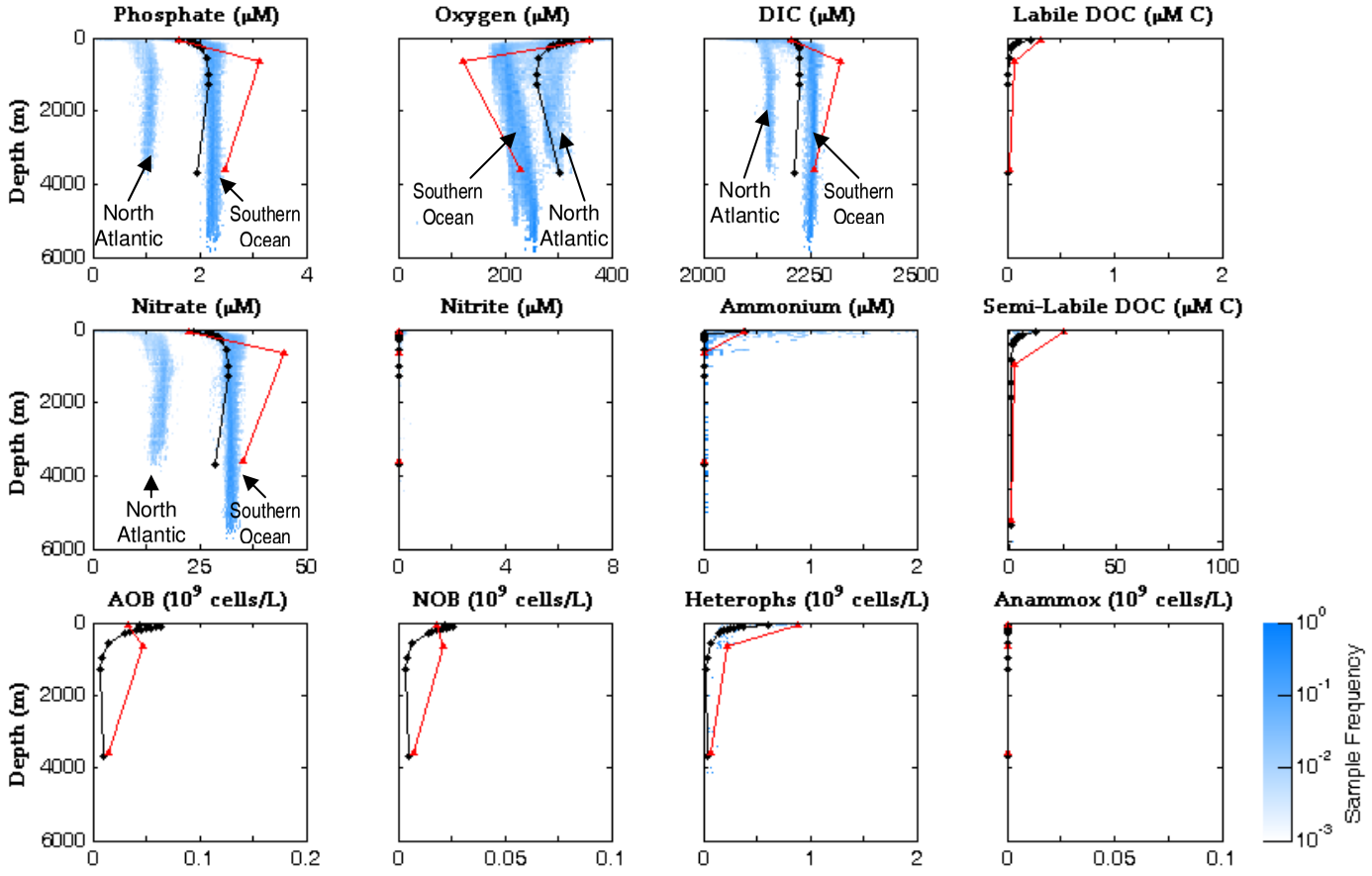

Figure 5.6. Simulated high-latitude biogeochemical profiles for the high-resolution (black) and low-resolution (red) Global Ocean ICBM model. Colored fields represent frequency of observations in the combined GLODAP and JGOFS AESOPS datasets.

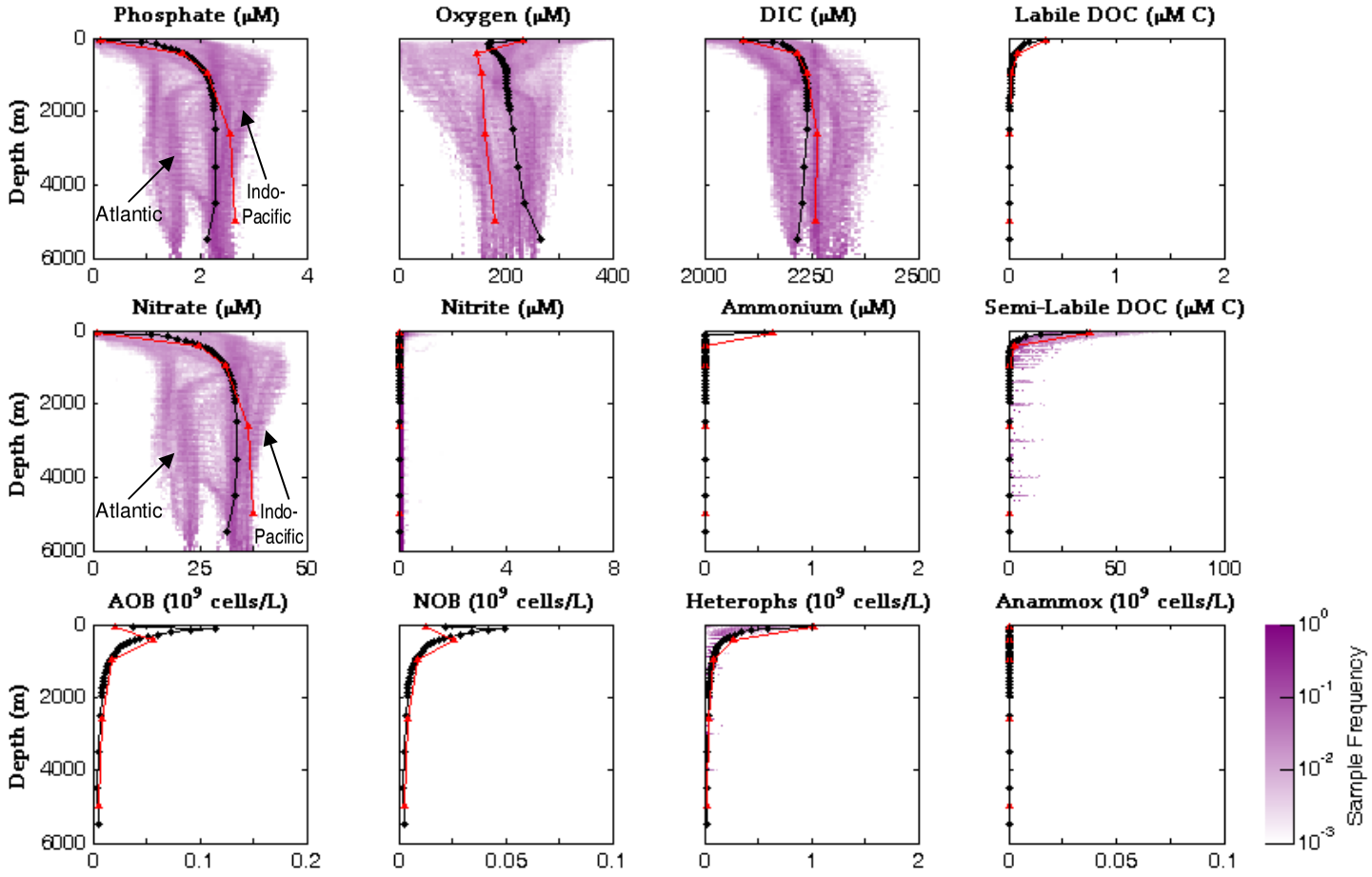

Figure 5.7. Simulated gyre biogeochemical profiles for the high-resolution (black) and low-resolution (red) Global Ocean ICBM models. Colored fields represent frequency of observations in the combined GLODAP, HOT, and BATS datasets.

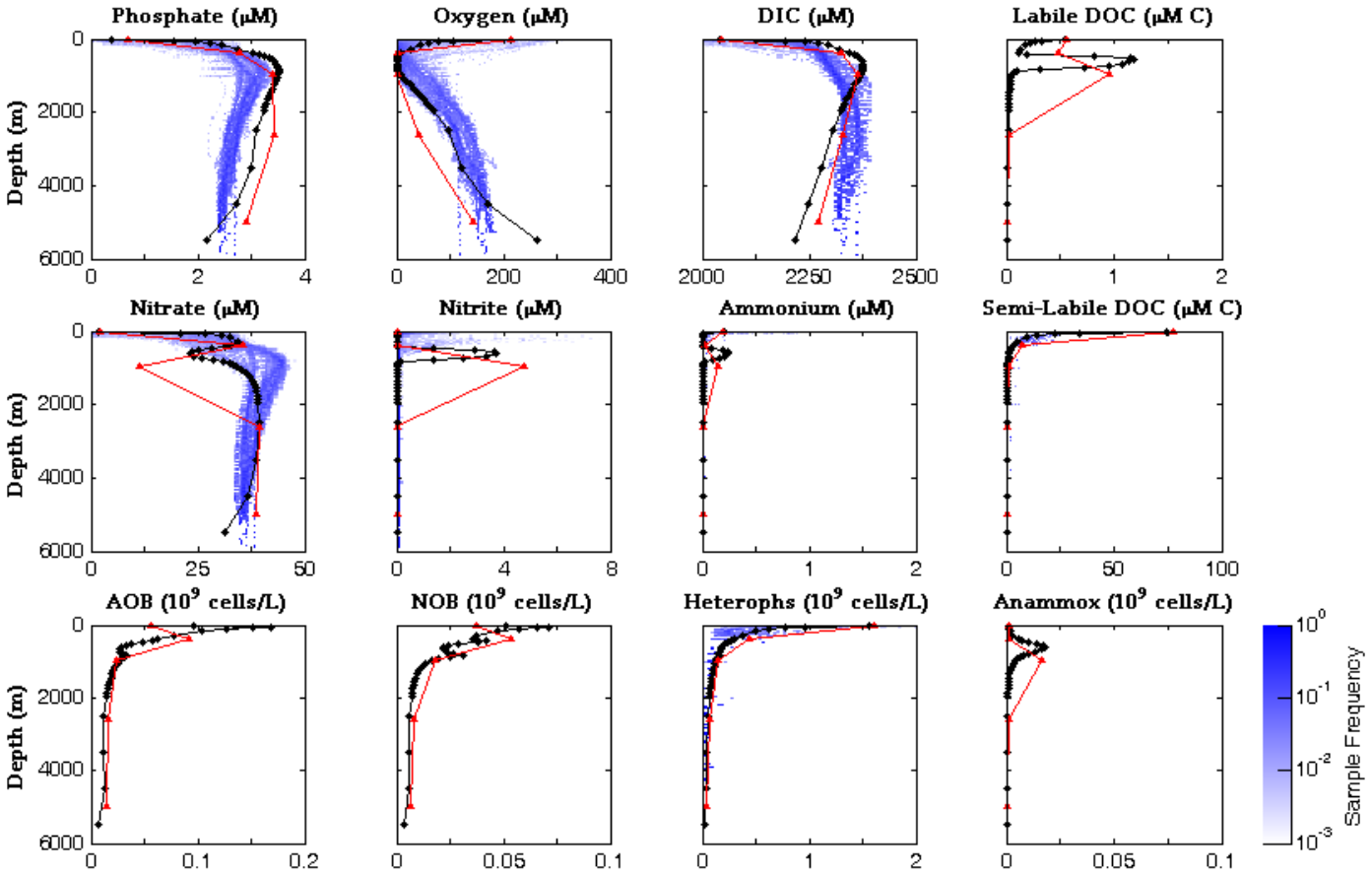

Figure 5.8. Simulated upwelling biogeochemical profiles for the high-resolution (black) and low-resolution (red) Global Ocean ICBM models. Colored fields represent frequency of observations in the combined GLODAP and JGOFS Arabian Sea datasets.

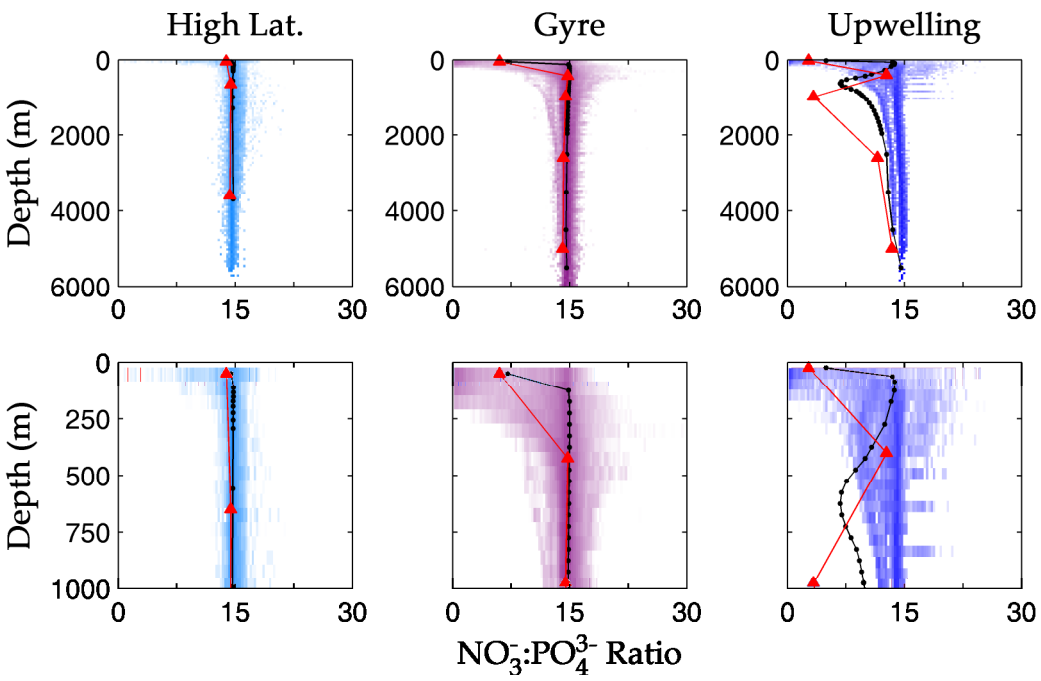

Figure 5.9. Comparison of simulated NO_3^-:PO_4^- ratios in the high-resolution (black) and low-resolution (red) models with observations. Lower panels show detail from the upper 1000 meters.

between the surface nutrient concentrations predicted by the high and low resolution models. Below 2000 meters, simulated phosphate in the upwelling region exceeds observed values by 0.3 µM and oxygen concentrations are at the lower range of observations, likely indicating insufficient lateral mixing in this region. The simulated nitrate deficit (defined as $N^* = [NO_3^-] - 16 \cdot [PO_4^{3-}] - 2.90$ [*Deutsch et al.*, 2001; *Gruber and Sarmiento*, 1997]) is an indicator denitrification and nitrogen fixation processes. Denitrification causes nitrate to be depleted relative to phosphorus, causing the nitrate deficit to become increasing negative. The simulated value of N* peaks at -34.5 µM in the model upwelling zone. This is higher than any regionally-average estimate of nitrate-deficit [*Deutsch et al.*, 2001; *Gruber and Sarmiento*, 1997], but is similar to the extreme ranges of N* observed on the WOCE P21E and I107N sections (Figure 5.10). Because pelagic denitrification occurs in "hot spots" of upwelling, the model must capture these more extreme values if realistic pelagic denitrification rates are to simulated.

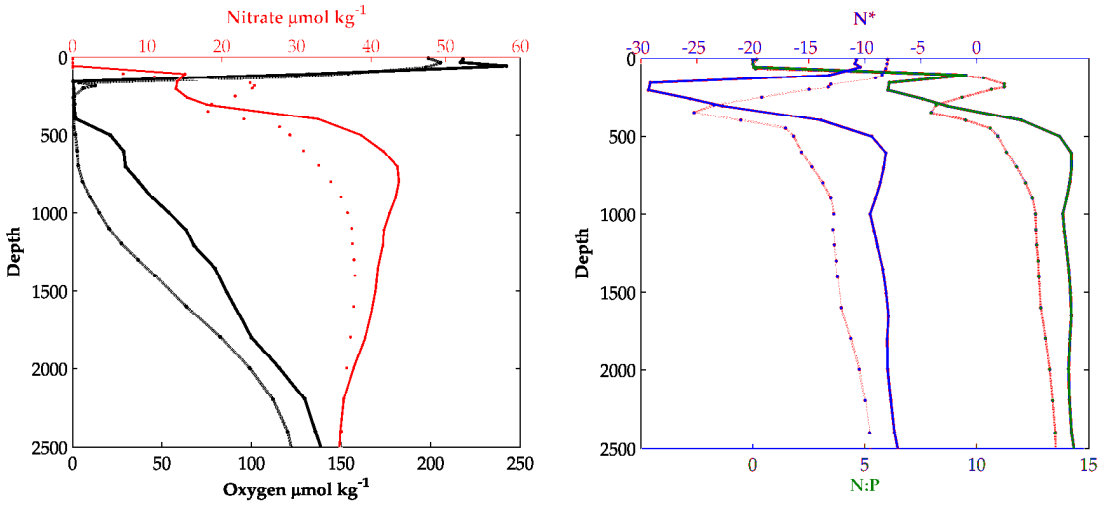

Figure 5.10. Profiles of dissolved oxygen, nitrate, N:P ratio, and N* for two upwelling sites in the Arabian Sea (dotted lines) and Eastern Tropical South Pacific (solid lines). Note the strong nitrate depletion associated with the oxygen minimum zone at 200-400 meters. Data are from the WOCE Hydrographic Programme (Section I107N, Stn 792 [19.333°N, 64.333°E, 8/13/1995], Section P21E, Stn 41 [16.746°S, 81.003°W, 4/8/1994]).

Both simulated nitrite and ammonium also follow observed trends. Ammonium is <0.01 µM throughout the water column, with a surface maximum of 0.4-0.6 µM, consistent with observations. In the upwelling region, both models predict a subsurface ammonium peak of 0.15-0.2 µM at the core of the oxygen minimum zone that is not apparent in any observed dataset to the best of the author's knowledge, although scattered values as high as 0.2 µM can be found at the depth of the OMZ in the Arabian Sea JGOFS data [*Codispoti*, 2000b]. In the high latitude and gyre regions, simulated nitrite is consistently below 0.01 µM. The current biogeochemical model has no mechanism for generating the primary nitrite maximum (typically ~0.5 µM µM) at the bottom of the euphotic zone, which is thought to be the results of incomplete nitrate reduction by phytoplankton or differential light limitation of ammonium- and nitrite-oxidizing nitrifiers [*Lomas and Lipschultz*, 2006; *Olson*, 1981b]. In the upwelling region, the magnitude of secondary nitrite maximum associated with the oxygen minimum zone is well-simulated

with a peak concentration of 3.75 μM. However, the depth of the simulated nitrite maximum, 600 m, is deeper than the depths of 50-500 meters typically observed.

As with nutrients, simulated gyre and high-latitude dissolved oxygen and DIC are typically immediate between Atlantic and Pacific and North Atlantic and Southern Ocean values. In general, simulated profiles show good agreement with observations. The only substantial deviation is in the lower 3000 meters of upwelling region, where the small box volumes and poorly detailed circulation make it difficult to simulate this region accurately. Higher in the upwelling water column, the depth of the oxygen minimum zone where simulated $O_2 < 10$ μM extends from 300-1000 meters and is well within the range of observations.

5.6.3 *Dissolved Organic Matter*

Simulated semi-labile dissolved organic matter (SDOM) concentrations are in generally within the range of observations. Surface concentrations of SDOM in the high-latitude and gyre regions are 12 μM and 38 μM, respectively. Surface concentrations of SDOM in the upwelling region, 77 μM, are somewhat higher than the values of 21-59 μM observed in the Arabian Sea. Until recently, determining the contribution of LDOM to the combined LDOM and SDOM pool required incubating the samples in the dark for several weeks to determine the proportion of rapidly degraded DOM. Since this method was time consuming and new incubation-free methods of separating LDOM and SDOM have only recently become available [*Davis and Benner*, 2007], very few data points are available for model validation. LDOM pools with turnover times of hours to weeks are thought to at most only a few percent of total DOM, 0 - 2 μM, as simulated here [*Carlson and Ducklow*, 1995].

5.6.4 *Microbial Populations and Rates*

In each region, the simulated profiles in each region capture the observed exponential decline in cell count with depth and correctly predict the magnitude of

surface and deep water populations. In detail, the model slightly over-predicts the surface populations in the gyre and upwelling regions. Moreover, observations from HOT and BATS also show a decline in microbial heterotrophs above 100 meters, while the model predicts a continuous exponential decrease with increasing depth. These discrepancies likely reflect the simple, steady-state, dynamics of the ICBM mixed layer.

Compared to bulk "heterotrophic" bacterial cell counts, much less is known about the abundance of nitrifiers and anammox bacteria in pelagic marine environments. Simulated populations of ammonium oxidizers increase from 2-3% of heterotrophic microbial cells in the mixed layer to >20% below 1000 meters. Absolute simulated abundances of ammonium oxidizers display a strong subsurface maximum immediately below the mixed layer, with peak abundances ranging from 0.6×10^8 cells/L in to the high latitude region to 1.6×10^8 cells/L in the upwelling region. Abundances declined to 0.05-0.1×10^8 cells/L at 4000 meters. Simulated nitrite oxidizer abundance displayed similar trends, but absolute abundances were only 43-75% of ammonium oxidizers. Early work enumerating specific species of marine ammonium oxidizing bacteria using immunofluorescent methods determined cell abundances of 2-8×10^4 cells/L between 0-100 meters [*Ward et al.*, 1982].This is between 3 and 4 orders of magnitude lower than predicted here. However, an important contribution to marine ammonium-oxidation from marine crenarchaeotes has been recently reported [*Wuchter et al.*, 2006]. Marine crenarchaeotes are ubiquitous and abundant throughout the ocean, approaching 40% of the total direct cell count [*Karner et al.*, 2001]. Working at the HOT site, Ingalls et al (2006) used an elegant compound-specific radiocarbon method to determine that 80% of archaeal biomass from 670 meters was supported by direct autotrophic production incorporating ambient, aged DIC. At this same site, Karner et al. (2006) determined that the relative abundance of crenarchaeotes rose sharply from 2-3% of the total DAPI count in the photic zone to 20-40% of total counts at depth. This profile bears a strong

resemblance to the simulated abundance of ammonium-oxidizers. If 80% of the crenarchaeotes at the HOT site were indeed autotrophic nitrifiers, the resulting cell counts profiles would closely match the simulated gyre nitrifier populations.

Below the uppermost reservoir, where nitrification rates are set to zero by default to simulate photoinhibition, simulated rates of ammonium- and nitrite-oxidation are tightly coupled and decrease exponentially with depth. Maximal simulated rates in each region are 6.2, 8.4, and 21.4 nM N/day in the high-latitude, gyre, and upwelling regions respectively. These patterns are similar to field observations, which indicate that maximal rates of ammonium-oxidation occur at the base of the euphotic zone [*Ward et al.*, 1989; *Ward*, 2000]. In the upwelling region, simulated rates of nitrite-oxidation display modest local maxima of 1 nM N/day in excess of ammonium-oxidation rates at the upper and lower boundaries of the oxygen minimum zone.

Cell counts of *Planctomycetes*-like anammox bacteria in have been determined for the Benguela and Peru upwelling systems [*Hamersley et al.*, 2007; *Kuypers et al.*, 2005]. Counts range from 0.4 - 3×10^7 cells/L for the Benguela system and 4-15×10^7 cells/L off of Peru. These values bracket the anammox population of 1.8×10^7 cells/L simulated for the core of the upwelling zone OMZ. However, the observed cell counts come from shallow-water, shelf environments (0-300 meters), while the model's OMZ core is located at 625 meters. At an open water site off Chile, the maximum rate of anammox was found just below the mixed layer between 50-100 meters[*Thamdrup et al.*, 2006]. Thus it is apparent that while the simulated anammox cell abundance is comparable in magnitude to observed values, more detailed hydrodynamic models of specific upwelling regions will be required to simulate the detailed spatial pattern of observations.

5.6.5 *Primary Production and Export*

Table 5.4 compares simulated regional and global carbon fluxes to estimates from the literature. Global marine net primary production is simulated at 43.4 Gt C/yr and 40.2

Table 5.4. Comparison of simulated and published estimates of global marine carbon fluxes. Compilation after Dunne et al. (2007). Units are Gt C/yr (1 Gt = 10^{15} g).

Parameter	13 Box ICBM	79 Box ICBM	Literature Value	Reference
Global Net Primary Production	43.4	40.2	44-57	[*Carr et al.*, 2006] and references therein
High Latitude Net Primary Production	5.7	2.4	1.1-6.1	[*Carr et al.*, 2006] and references therein
Global Export Production	12.1	10.8	9.6+/-3.6	[*Dunne et al.*, 2007]
			11.1-12.9	[*Laws et al.*, 2000]
			9.2	[*Aumont et al.*, 2003]
			8.6	[*Heinze et al.*, 2003]
			8.7-10.0	[*Gnanadesikan et al.*, 2004]
			9.6	[*Schlitzer*, 2004]
			5.8-6.6	[*Moore et al.*, 2004]
Export Flux South of 50°S (vs. entire ICBM high latitude)	1.7	0.24	.69 +/- 0.26	[*Dunne et al.*, 2007]
			1.1 +/- .2	[*Pollard et al.*, 2006]
Flux across 1000m (60°N-60°S vs. ICBM gyre)	1.11	1.14	0.63+/-.22	[*Dunne et al.*, 2007]
			0.86	[*Jahnke*, 1996]
			0.71-0.86	[*Gnanadesikan et al.*, 2004]
Flux across 2000m (30°S-47°N vs. ICBM gyre)	0.61	0.63	0.20+/-.08	[*Dunne et al.*, 2007]
			0.16+/-0.11	[*Ganachaud and Wunsch*, 2002]
			0.22-0.32	[*Gnanadesikan et al.*, 2004]
Global Flux to bottom	1.82	1.67	2.3 +/-0.9	[*Dunne et al.*, 2007]
			0.93	[*Muller-Karger et al.*, 2005]
Burial in Margins (50-2000m)	0.12	0.12	0.29 +/- 0.15	[*Dunne et al.*, 2007]
			.06 +/- 0.06	[*Muller-Karger et al.*, 2005]
Burial in Deep Sea (>2000m)	0.0019	0.0024	.012 +/-.02	[*Dunne et al.*, 2007]
			0.09	[*Muller-Karger et al.*, 2005]

Gt C/yr for the 13- and 79-box models respectively. This is slightly lower than the range of estimates in a recent review of global primary production estimates from satellite observations and GCM models, which ranged from 44-57 Gt C/yr [*Carr et al.*, 2006]. Predicted high-latitude primary production is quite different between the low-resolution and high-resolution models, 5.7 and 2.4 Gt C/yr, but both estimates are within the current range of satellite-based estimates, 1.1-6.1 Gt C/yr [*Carr et al.*, 2006]. Globally, the estimated export flux of particulate organic carbon is 12.1 and 10.8 Gt C/yr for the two models, which is similar to a number of other recent estimates (Table 5.4). Broken down by region, the model-estimated particle export ratios are 30%, 27%, and 44%, for the high-latitude, gyre, and upwelling regions respectively for the low-resolution model, and 10%, 27%, and 42% for the high-resolution model. Low-latitude POC fluxes across 1000 and 2000 meters are slightly greater than previous estimates, but the benthic carbon flux and carbon burial flux are well within the range of published estimates (Table 5.4).

5.6.6 *Nitrogen Fixation, Denitrification, and Anammox*

Table 5.5 compares simulated and published estimates of marine nitrogen fluxes. Nitrogen cycling in the low-resolution model is much more vigorous than in the high resolution model, though the rate of nitrogen fixation predicted by the two models brackets published estimates. Since both models have been run to steady state, new inputs of nitrogen (nitrogen fixation and allochthonous inputs) exactly balance fixed-N losses (benthic denitrification, pelagic denitrification and anammox, and N-burial). Because allochthonous N-inputs are fixed, simulated nitrogen fixation must ultimately adjust to accommodate combined fixed-N losses.

In the low resolution model, both benthic denitrification and pelagic denitrification/anammox are significantly higher than in the high-resolution model, while N-burial remains constant. The increase in pelagic denitrification appears to be entirely due to model resolution. At low resolution, the sharp redox gradients associated with the

Table 5.5. Comparison of simulated and published estimates of global marine nitrogen fluxes. Units are Tg N/yr (1 Tg = 10^{12} g).

Parameter	13 Box ICBM	79 Box ICBM	Literature Value	Reference
Pelagic N-Fixation	146	80	117	[*Codispoti et al.*, 2001]
			120+/-50	[*Gruber*, 2004]
			138	[*Deutsch et al.*, 2007]
Total Allochthonous Inputs	68	68	160	[*Codispoti et al.*, 2001] (Modern)
			130+/-25	[*Gruber*, 2004] (Modern)
			50	[*Brandes and Devol*, 2002] (Preanthropogenic)
			41.2	[*Galloway et al.*, 2004] (Preanthropogenic)
Pelagic Denit. + Anammox	75	38	150	[*Codispoti et al.*, 2001]
			65+/-20	[*Gruber*, 2004]
			70	[*Deutsch et al.*, 2004]
% Anammox of Total Pelagic Fixed-N Loss	13%	21%	29%	[*Dalsgaard et al.*, 2003]
			19-35%	[*Dalsgaard et al.*, 2003] (Gulfo Dulce)
			100%	[*Hamersley et al.*, 2007] (Peru Margin)
			100%	[*Kuypers et al.*, 2005] (Benguela Margin)
Benthic Denitrification	115	88	300	[*Codispoti et al.*, 2001]
			180+/-50	[*Gruber*, 2004]
			190	[*Deutsch et al.*, 2004]
Burial	24	24	15	[*Codispoti et al.*, 2001]
			25+/-10	[*Gruber*, 2004]

upwelling oxygen minimum zone are poorly resolved, artificially broadening the suboxic region. The large difference in the rates of benthic denitrification in the high versus low-resolution model is a consequence of a 4 Tg/yr (5%) increase of benthic denitrification in the gyre region, apparently due to decreased vertical resolution, and a large increase in high-latitude benthic denitrification, from near 0 Tg/yr to 22 Tg/yr, due to increased high latitude export production.

5.6.7 *Phosphorus Cycling*

Table 5.6 compares the ICBM marine phosphorus cycle with data from several recent reviews of global phosphorus cycling. Unfortunately, literature estimates are widely disparate. The problem hinges around determining the reactivity and fate of the large flux of particulate inorganic phosphorus (PIP) delivered to estuaries and river deltas. Between 70-90% of PIP delivered to the ocean is thought to be insoluble or otherwise unavailable for biological uptake [*Compton et al.*, 2000]. This fraction rapidly settles out in estuaries and the near-shore environment, but early diagenetic cycling or erosional reworking of sediments may still liberate an unknown fraction (Colman and Holland, 2000). Large anthropogenic inputs of phosphorus to coastal marine environments further complicate efforts to determine preanthropogenic reactive phosphorus inputs [*Paytan and McLaughlin*, 2007]. Since the phosphorus biogeochemical cycle has no significant gas phase, a viable alternative to determining P-inputs is to determine P-burial rate from sediment P-concentration and accumulation rates. However, difficulty separating reactive authigenic phases from nonreactive detrital phosphorus hampers this approach, while spatial heterogeneity complicates the task of extrapolating global burial rates from isolated measurements. As a result, reactive phosphorus burial estimates vary from 3-21 $\times$ 10^{10} mol P/yr (Table 5.6). Thus, at present it seems impossible to constrain the marine phosphorus cycle to better than a factor of 3. Nevertheless, it is comforting that the ICBM models are able to reproduce the observed deep water phosphate concentration and global

Table 5.6. Comparison of simulated and published estimates of global marine phosphorus fluxes. Units are 10^{10} mol P/yr.

Parameter	13 Box ICBM	79 Box ICBM	Literature Value	Reference
Total Preanthropogenic Reactive P Inputs (Riverine + Aeolian)	15	15	3.8-7.2	[*Paytan and McLaughlin*, 2007][1]
			10-15.5	[*Compton et al.*, 2000]
			18.4	[*Follmi*, 1996]
			3-15	[*Froelich*, 1988]
Total Anthropogenic Reactive P Inputs	0	0	0.8-3.8	[*Paytan and McLaughlin*, 2007][1]
			1-17	[*Compton et al.*, 2000]
Total Reactive P burial	15	15	3.2-8.1	[*Compton et al.*, 2000]
			21	[*Filippelli and Delaney*, 1996]
			9.4	[*Berner and Berner*, 1996b]
			15.2	[*Follmi*, 1996]
			8-18.5	[*Ruttenberg*, 1993]
			5	[*Froelich et al.*, 1982]
P-removal at mid-ocean ridges	0	0	1.2-1.6	[*Wheat et al.*, 1996]

[1] Assumes 10-30% of total riverine P is reactive and 25% of reactive P is exported from estuaries.

primary production while employing realistic deterministic export, remineralization, sedimentation, and burial parameterizations, using an allochthonous reactive phosphorus input of 15×10^{10} mol P/yr. This value is well within the range of global reactive phosphorus input and burial estimates.

5.7 *Discussion and Sensitivity Testing*

The global ICBM model displays several advantages over previous models generations of ocean box models. In the high-resolution configuration, the model is able to simultaneously reproduce observed high-latitude and gyre temperature, background $\Delta^{14}C$, bomb $\Delta^{14}C$, and CFC-11 profiles. This was not previously possible using the regard is the parameterization of isopycnal ventilation of the gyre thermocline with a fraction of the source water coming from both gyre surface and high-latitude reservoirs. In other

words, water subducted at intermediate-latitude density outcrops is modeled as a linear combination of the gyre and high latitude surface reservoirs (Table 5.3).

As described in Section 1, an early generation of 3-box ocean models [*Knox and McElroy*, 1984; *Sarmiento and Toggweiler*, 1984a; *Siegenthaler and Wenk*, 1984a] displayed extreme over-sensitivity to high-latitude nutrient drawdown resulting in anoxia of the deep ocean [*Sarmiento et al.*, 1988a; *Sarmiento and Orr*, 1991]. These experiments were duplicated using the ICBM model to show that high-latitude nutrient drawdown in the ICBM more closely resembles the results of early GCM experiments than 3-box models. Specifically, sudden release of the nutrient drawn-down limitation in the global ICBM high-latitude surface reservoir results in a small region of anoxia in the high-latitude water column at approximately 500 meters depth but has only a small impact on gyre oxygen profiles (Figure 5.11). At the deepest gyre depths, where the oxygen perturbation is largest, the ICBM simulates a 130 μM decrease in dissolved oxygen (black profiles) which compares to a decrease of 100-125 μM found by Sarmiento and Orr (1991) using an early 3-D GCM model. Simulations with a simplified 13-box global ICBM model display similar results (red profiles). The sudden onset of high-latitude nutrient consumption is initially accompanied by a sharp spike in global export production of 10 Gt C/yr, which is subsequently suppressed by a rapid increase in pelagic denitrification to 590 Tg N/yr that accompanies the onset of high-latitude anoxia (not shown). In response to denitrification, nitrogen fixation slowly increases over the next 10ky to 350 Tg N/yr. After 10 ky, rates of denitrification, nitrogen fixation, and global export production all decrease, relaxing to steady state values by 100 kyr. The new equilibrium state is characterized by slightly higher global export production (13.1 Gt C/yr), significantly higher rates of nitrogen fixation and denitrification (207 and 102 Tg N/yr, respectively), and the absence of anammox. These changes provide numerical support for the original hypotheses presented in [*Knox and McElroy*, 1984] that the

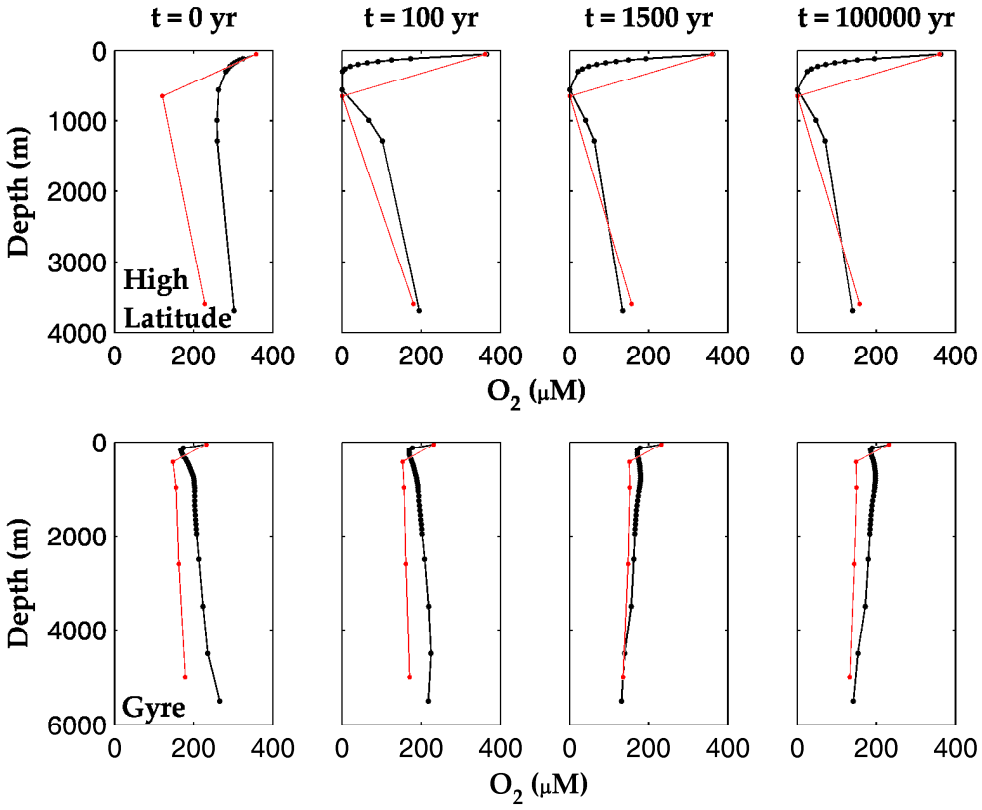

Figure 5.11. Perturbations to ICBM-simulated dissolved oxygen profiles as a result of high-latitude nutrient drawdown. Profiles at t = 0 (left panels) are the steady state results of previous standard simulations. At t=0, the restriction on high-latitude nutrient drawdown is removed (previously set at 1.5 μM PO_4^{3-}). Release of nutrient limitation allows for a rapid increase in high-latitude export production and onset of high-latitude suboxia occurs with 10 years (upper panels). However, gyre profiles are only modestly perturbed (lower panels). Results are similar to those found by previous workers using an early 3D GCM model [*Sarmiento and Orr*, 1991]. Similar responses are found for both the 13-box (red) and 79-box (black) versions of the global ICBM model.

drawdown of high latitude nutrients could result in anoxia and increased rates of denitrification. However, the exact pattern of anoxia predicted by the ICBM model differs substantially from that found by early authors [*Knox and McElroy*, 1984; *Sarmiento et al.*, 1988a] and is instead similar to the results of early 3-D GCM simulations [*Sarmiento and Orr*, 1991].

More recent work has focused on quantifying the "high-latitude sensitivity" of global P_{CO2} to changes in high-latitude nutrient consumption in box models and GCMs

[*Archer et al.*, 2000; *Bacastow*, 1996; *Broecker et al.*, 1999; *Lane et al.*, 2006]. While the focus of the current ICBM development is on Proterozoic biogeochemistry, future work should examine a variety of these high-latitude sensitivity metrics for the ICBM model. The improved simulation of transient tracers, net export production, and dissolved O2 dynamics compared with earlier 3-box, box-diffusion, and PANDORA-type models suggests that the high-latitude sensitivity of the ICBM model should cluster closer to the GCM models than have previous box models.

5.8 *Discussion of the Biogeochemical Model*

The ICBM biogeochemical model explores the significance of adding or combining several new components to the model structure. In particular, the addition of explicit, oxygen-dependent nitrogen cycling (including nitrogen fixation, nitrogen fixation, ammonium oxidation, nitrite oxidation, pelagic denitrification and anammox, and sedimentary denitrification) was designed to allow simulation of changes in the marine nitrogen cycle in response to variations in ocean redox. This work complements previous models of nitrogen and phosphorus cycling[*Bjerrum et al.*, 2006; *Deutsch et al.*, 2004; *Handoh and Lenton*, 2003; *Lenton and Watson*, 2000a; *Lenton and Klausmeier*, 2007; *Shaffer*, 1989; *Slomp and Van Cappellen*, 2007; *Tyrrell*, 1999; *Van Cappellen and Ingall*, 1994; *Wallmann*, 2003]) by explicitly simulating the role of oxygen and "realistic" deepwater ventilation and upwelling processes in controlling feedbacks on marine nitrogen cycling. Some of these same processes have begun to appear to ocean GCM models [*Moore and Doney*, 2007b], but computational expense has so far limited simulations to ~2500 model years which does not allow time for adjustments in the dissolved phosphate inventory. Thus, the ICBM approach provides a significant contribution to field which is currently unavailable in other models.

Since several of the features of the biogeochemical model are novel, initial sensitivity tests of the model structure were undertaken to assess the significance of the

new processes. These results are not shown, but are described in the following paragraphs. In the first experiment, all microbial populations, dynamically calculated in the default model, were replaced with constant values equal to the maximum values obtained at steady-state in the default global runs: 0.169, 0.071, 1.611, and 0.018×10^9 cells/L for ammonium-oxidizers, nitrite-oxidizers, heterotrophs, and anammox bacteria respectively. The results of simulations with and without dynamic simulation of microbial populations were remarkably similar. The only significant differences observed in the runs without microbial dynamics were a depression of the small labile organic matter and ammonium peaks in the upwelling zone oxygen-minimum zone and a 3% increase in total N_2 production. Examination of the transient dynamics of the two runs revealed no significant differences in the model dynamics. Apparently, as simulated here, the dynamic adjustment of the microbial populations plays only a minor role in controlling the overall reaction rates of marine biogeochemical processes on time scales longer than 1 year. These results support the idea that processes with short response times are often unable to affect the longer-term dynamics in coupled biogeochemical models.

In a second sensitivity experiment, the simulation of nitrite dynamics was removed from the model. Nitrite is a short-lived intermediate in many biogeochemical processes, such as nitrification and denitrification. To remove nitrite from the model, all processes capable of producing nitrite in the default simulation were modified to eliminate simulation of the nitrite-intermediate. The nitrification module was modified by summing the separate ammonium-oxidation and nitrite-oxidation steps to produce a single "nitrification" reaction regulated by ammonium-oxidation kinetics. The denitrification module was modified to likewise combine dissimulatory nitrate- and nitrite-reduction. In other words, these reactions were modified assuming the first step of each process is rate limiting and that the nitrite intermediate is at quasi-steady state. As a consequence of these modifications, the anammox reaction is completely inhibited by the

absence of nitrite production anywhere in the model domain. Again, we find that the model dynamics were relatively insensitive to these modifications. Simulated steady-state and transient component profiles were very similar to the default run, with the obvious exceptions of nitrite and anammox bacteria which are completely absent from the model. The decrease the production of N_2 by anammox is more than compensated for by an increase in classical denitrification rates, resulting in a 10% (3.5 Tg N/yr) increase in pelagic N_2 production. Preliminary experiments alternately disabling classical denitrification, anammox, or thiodenitrification seem to generalize this result, suggesting that total pelagic fixed-N losses might be less sensitive to the exact pathway of the removal than might be expected. However, further work is needed to confirm this result.

Taken together, these experiments suggest that the combined ICBM transport and biogeochemical submodels are surprisingly insensitive to changes in the architecture of the biogeochemistry submodel. Nutrient cycling appears to be primarily governed by the first-order processes of primary production, export, remineralization, and burial. Changes in the exact representation of individual processes have only secondary effects. If confirmed, these results may indicate that some of the processes simulated in the default model, such as microbial kinetics and reaction intermediates like nitrite, may be removed from future versions of the model with little effect. However, it is difficult to exclude the possible impact of these processes under all conditions, so decisions regarding model complexity must still depend on nature of the question under consideration.

SECTION 6

SIMULATION OF THE MODERN BLACK SEA

6.1 *Introduction to the Black Sea Validation*

In order to further test the ICBM biogeochemistry, it is useful to simulate environments which are more similar to the conditions expected in ancient oceans. Globally, a number of anoxic and euxinic (sulfide-bearing) marine basins have been proposed as analogs of ancient suboxic oceans. These include silled basins such as the Black Sea, Baltic Sea, Cariaco Basin, and Gulfo Dulce; hypersaline basins such as the Orca and Tyra Basins; and permanently anoxic fjords such as Effingham Inlet and Framvaren Fjord. These basins share a number of similarities, including steep bathymetry, restricted circulation, and strong density stratification.

The goal of this section is to show that the same ICBM biogeochemistry used in the global model to simulate open ocean conditions can also be used to simulate the Black Sea when an appropriate model geometry and circulation model are adopted. The alternative circulation model is modified from a 1-D inversion of the Black Sea temperature and salinity fields as described below [*Ivanov and Samodurov*, 2001]. A brief review of Black Sea circulation is provided in Section 6.2. Section 6.3 and 6.4 provide a description of the new circulation model and model boundary conditions. Finally, numerical simulations are presented and compared with observations in Section 6.5.

Preliminary simulations showed that 3 modifications to the model biogeochemistry model parameterizations were necessary to simulate the Black Sea with good accuracy. These changes, described below, reflect simplifications and basin dependent assumptions in the model. First, and most importantly, the temperature restriction on nitrogen fixation (set to >18°C in the global model) was eliminated. The seasonal temperature climatology of Black Sea surface waters ranges from ~7°C in early spring to 30°C in late summer, with a mean temperature of about 14°C. This mean

temperature would imply that the basin is too cold for most marine nitrogen fixers, however summer time temperatures in the Black Sea may actually be quite favorable for nitrogen fixation. This seasonality is not represented in the current version of the ICBM model. Removing the temperature restriction is equivalent to assuming that any summertime maximum in nitrogen fixation, when waters are warm enough for significant nitrogen fixation, is annually averaged over the seasonal cycle. Without nitrogen fixation, the simulated Black Sea is restricted to oxic conditions throughout the water column by a strong denitrification feedback, making this a small but substantial modification. The second change was to adapt the coastal primary production enhancement to 2X the open ocean flux for shelf region less than 100 meters deep (c.f. 2.5X in regions <1000 meters in the global model). This change reflects the larger proportional area of shelf in the Black Sea and the mesotrophic environment of the central Black Sea compared with the very oligotrophic nature of the open ocean gyres. This change results in a small increase in deepwater and sulfide and nutrient concentrations, bringing them closer to observed values. The final change was to modify the Black Sea ICBM's representation of sinking carbonate to include a significant dissolution flux below 500 meters due to strong undersaturation with respect to carbonate and aragonite in the deep Black Sea [*Hiscock and Millero*, 2006]. This change results in a ~100 μM increase in simulated deep water TCO_2. These last two changes improved the accuracy of the model but do not produce a qualitative change in the simulated Black Sea profiles and fluxes.

6.2 *Circulation of the Black Sea*

The Black Sea is currently the world's largest anoxic marine basin and is widely considered to be archetypical of other such settings [*Anbar and Knoll*, 2002; *Murray and Izdar*, 1989]. Anoxia is primarily the result of strong stratification driven by a flow of dense, warm, and salty Mediterranean water into the Black Sea along the bottom of the Turkish Strait system (Dardanelles Straits, Sea of Marmara, and Bosphorus Straits). This

dense water cascades over a sill at 60 meters depth at the northern mouth of Bosphorus Straits [*Latif et al.*, 1991], entrains Black Sea water in a ratio of 3-10x [*Ivanov and Samodurov*, 2001; *Lee et al.*, 2002; *Murray et al.*, 1991], and fills the deep basin of the Black Sea to create a strong halocline between approximately 50 and 150 meters depth [*Murray et al.*, 1991]. At the surface, large inputs of freshwater from rivers and precipitation maintain the positive water balance of the Black Sea and drive the outflow of brackish surface water back out through the surface layer of the Bosphorus straits [*Ozsoy and Unluata*, 1997]. The two layer structure of the Turkish straits, with warm salty water flowing into the Black Sea in the lower layer and cool brackish water following out at the surface, sets up the salinity balance which governs the relevant dynamics. The schematic mean annual circulation of the Turkish Strait system is given in Figure 6.1.

Figure 6.2 depicts a typical CTD cast from the central Western Gyre (R/V Knorr 2001, Station 2, Cast 9). Panels A-C show the full-scale trends in potential temperature,

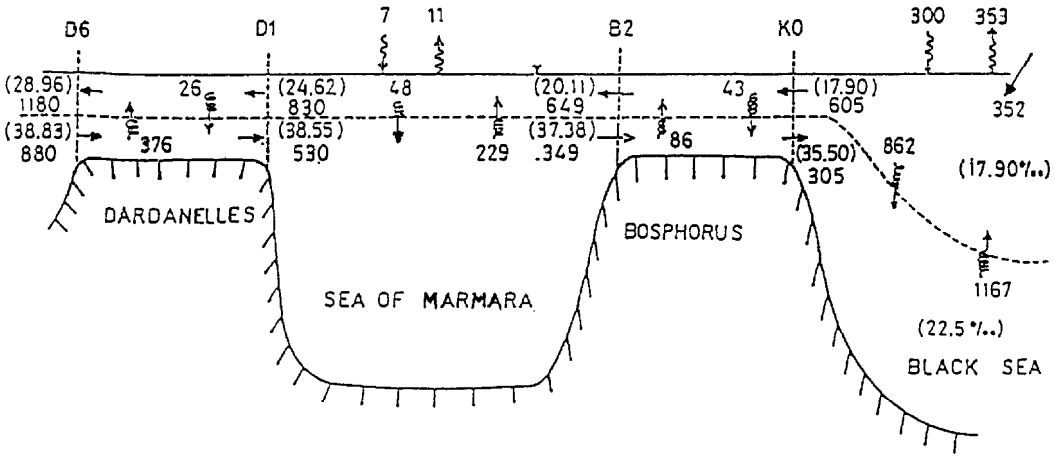

Figure 6.1. Mean annual volume fluxes in the Turkish Straits system [*Latif et al.*, 1991; *Unluata et al.*, 1990]. Fluxes are given in km^3/yr. Numbers in parentheses are average salinity values used in computations. (Figure from [*Ozsoy and Unluata*, 1997]).

salinity, and potential density respectively. Panels D-F focus in on the upper water column structure and cold intermediate layer (CIL), while panels G-I highlight the bottom boundary homogenous layer (BBHL). The full scale profiles (A-C) primarily reflect the influence of the Bosphorus Plume at depth and freshwater input at the surface creating strong salinity and density gradients in the upper 500 meters. Below 52 meters, both salinity and potential temperature increase monotonically with depth. Panels D-F depict a surface mixed layer extending to a depth of 46 m, underlain by the CIL extending from 47 to 79 meters as defined by the 8°C isotherm [*Murray et al.*, 1991]. The CIL is thought to be formed annually during the coldest winter months, either locally during winter storms [*Gregg and Yakushev*, 2005; *Ivanov et al.*, 2001; *Ovchinnikov and Popov*, 1987] or by isopycnal transport from the North West Shelf region where the coldest winter temperatures are found [*Filippov*, 1965; *Staneva and Stanev*, 1997; *Tolmazin*, 1985]. It appears that the relative importance of both processes varies from year to year depending on particular regional weather events [*Gregg and Yakushev*, 2005; *Oguz et al.*, 1991; *Stanev et al.*, 2003]. It is estimated that CIL waters are partially replaced every other year on average [*Ivanov et al.*, 2000]. In Figure 6.2, the bottom panels (G-I) depict the stair-step-like transition to the BBHL. Such steps are a characteristic feature of the diffusive double-diffusion regime which occurs when a weakly salinity-stratified water column is heated from below, destabilizing the profile and creating a convective boundary layer [*Eremeev*, 1998; *Murray et al.*, 1991; *Turner*, 1973].

6.3 *Circulation Model of the Black Sea*

The model of Black Sea circulation used here is adapted from an inverse solution to the laterally-averaged heat, salt and, mass balance equations, based on known inputs of heat, salt, and mass [*Ivanov and Samodurov*, 2001; *Samodurov and Ivanov*, 1998]. This approach is similar to that used by Konovalov in biogeochemical models specifically

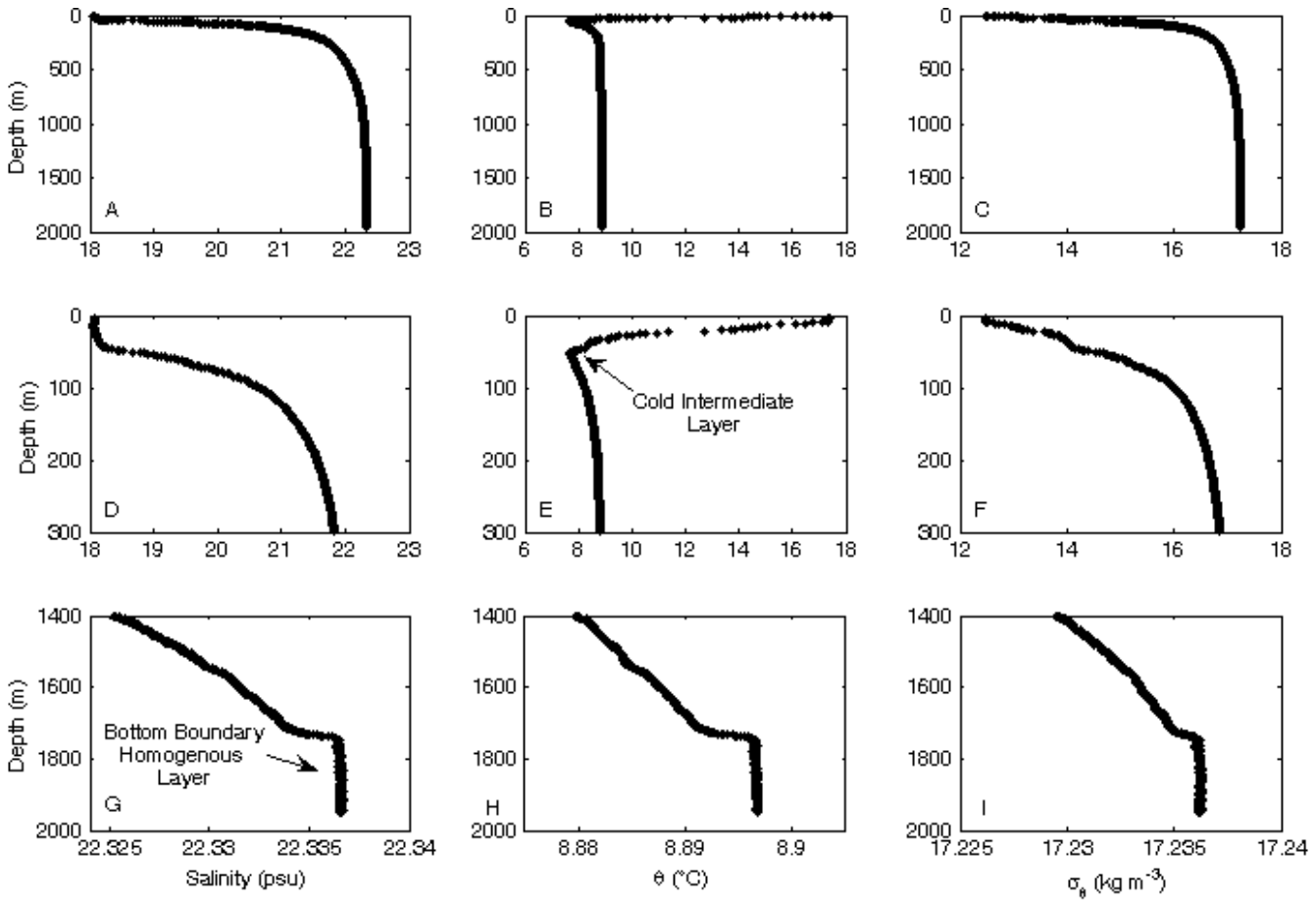

Figure 6.2. Typical Black Sea CTD cast. The top panels (A, B,C) depict the full scale profiles of salinity, potential temperature, and potential density respectively. Panels D-F expand the upper 300 meters to highlight the Cold Intermediate Layer. Panels G-I expand the bottom 600 meters, highlighting the Bottom Boundary Homogenous Layer. Note the scale in the lower panels. (After [*Murray et al.*, 1991])

designed for the Black Sea [*Konovalov et al.*, 2004; *Konovalov et al.*, 2000; *Konovalov et al.*, 2006]. The complete details of the original circulation model can be found in *Ivanov and Samodurov* [2001]. A conceptual overview will be provided here for completeness before focusing on three important modifications, the addition of hypsometry, a stationary surface layer, and simplification of the Bosphorus Plume dynamics.

The basic processes invoked by *Ivanov and Samodurov* [2001] are depicted in Figure 6.2, as first described by [*Ozsoy et al.*, 1993]. Inflowing Mediterranean water from the deep layer of the Bosphorus Straits entrains ambient CIL water from southwest shelf in the depth region between 50 and 100 meters. Upon reaching the shelf break at approximately 100 m, the dense plume cascades down slope toward the abyssal plain. As it flows down slope, fingers of plume water are laterally injected into the basin along specific isopycnals, presumably due to buoyancy forces acting on stratified layering within the plume itself. At the bottom of the continental slope, any remaining portion of the plume spreads out across the abyssal plain and is homogenized within the BBHL by geothermal heating and convective processes. Injection of the plume waters at depth is balanced by diffuse basin-wide upwelling.

The physical inverse model divides the water column vertically into three regions; the plume entrainment region (50-100 m), the plume disintegration region (100-1750 m), and the BBHL (1750-2200 m). Coupled heat, salt, and mass continuity equations are defined for each layer to determine the continuous vertical velocity and eddy diffusivity profiles. The calculation assumes that the only source of salt and mass to the interior water column is the Bosphorus plume. Heat is provided by both the plume and the geothermal flux through the abyssal plain. Heat flux from the basin walls above the upper boundary of the BBHL is neglected.

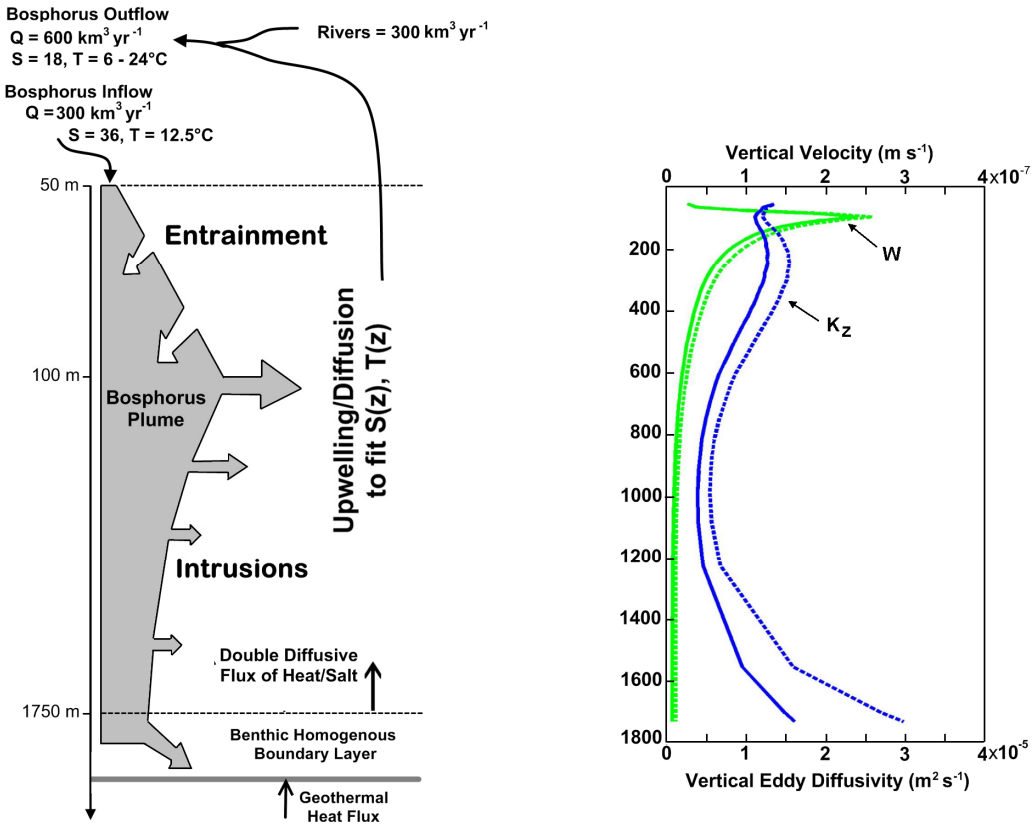

Figure 6.3. (Left) Basic processes included in the 1-D vertical model of *Ivanov and Samodurov* [2001]. (Right) Resulting profiles of vertical upwelling velocity (W, green) and vertical eddy diffusivity (K_Z, blue). Solid lines are the original profiles of *Ivanov and Samodurov* [2001]. Dotted lines are the profiles used in this work following a correction for the decrease in basin cross-sectional area with depth.

To solve for unknown circulation, *Ivanov and Samodurov* [2001] make and justify several assumptions:

1) The vertical diffusivity of heat and salt are the same everywhere except at the upper boundary of the BBHL, where double diffusive processes dominate the vertical mixing as a result of strong geothermal heating.

2) The Bosphorus Plume is linearly stratified in density by the time it reaches the first point of intrusion.

3) All intrusions leave the Bosphorus plume as pure advection (i.e. the core of the plume is left unaltered).

4) All intrusions are isopycnal intrusions except in the BBHL where the plume water may be denser than the ambient water.

5) Simple physically-consistent functions can be used to model the real vertical upwelling velocity.

Making these assumptions allows one to solve for the unknown profiles of vertical eddy diffusivity and upwelling velocity (Figure 6.2, solid lines). The original inverse model did not account for the effect of basin hypsometry, which is very important in controlling nutrient burial and water column redox conditions in "nutrient trapping" regimes like the Black Sea [*Sarmiento et al.*, 1988b]. To allow for the effects of hypsography, the original estimates of the eddy diffusivity and vertical velocity were scaled by:

$$w(z) = w°(z) \cdot \frac{3.8 \times 10^{11} m^2}{Area(z)} \qquad K_z(i) = K_z°(z) \cdot \frac{3.8 \times 10^{11} m^2}{Area(z)} \qquad 6\text{-}1$$

where $w°(z)$ and $K_z°(z)$ are the original calculated upwelling velocity and eddy diffusivity and $3.8 \times 10^{11} m^2$ is the basin area assumed by *Ivanov and Samodurov* [2001]. The scaling adjusts the vertical fluxes of heat and salt to match the original fluxes, despite assuming a decreasing cross-sectional area with depth. The Black Sea hypsometry (not shown) was derived from the ETOPO2v2 satellite bathymetry at 2-minute horizontal resolution and 1 meter vertical resolution.

The most important change made to the circulation model of *Ivanov and Samodurov* is to adopt a different scheme for plume entrainment and intrusion. This modification is unavoidable since the original model does not specify the transport of passive tracers during plume formation and intrusion [*S. Konovalov*, personal communication]. The scheme adopted here (Figure 6.4) is a simplified version of that

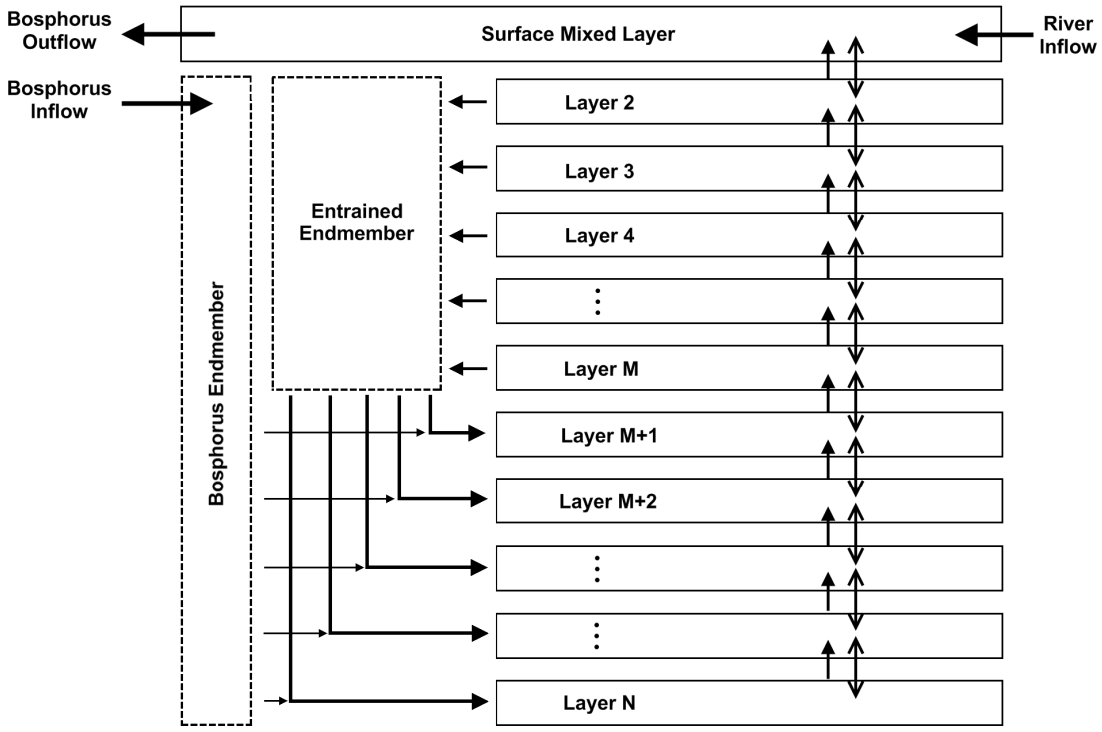

Figure 6.4. Schematic illustration the two-endmember Bosphorus plume model used to simulate the Black Sea. Ventilation of the deep layers occurs by mixing the two endmembers according to the depth-dependent entrainment ratio. The dashed boxes indicate that the endmembers boxes are not explicit reservoirs in the model. Entrained water is instantaneously mixed with incoming Bosphorus water and injected into the deeper layers. See text for details.

used by [*Lee et al.*, 2002]. The continuous process of entrainment of CIL water into the Bosphorus Plume and subsequent injection into the deep Black Sea is simplified as two-endmember mixing between the Bosphorus Inflow and entrained waters (Figure 6.4). The entrainment ratio of the endmembers for plume injection in each layer (M+1 to N, Figure 6.4) was determined by fitting the model to the observed temperature and salinity profiles shown in Figure 6.2, using the vertical advection and diffusion profiles of *Ivanov and Samodurov* [2001]. Entrainment ratios are defined as the fraction of entrained flow divided by the fraction of Bosphorus Input injection into each vertical level. For the

optimization calculation, an annually-averaged potential temperature and salinity of 13.91°C and 36 psu for the Bosphorus Inflow and 7.743°C and 18 psu for the CIL (Layer 2) were assumed. The double-diffusive dynamics of the BBHL and geothermal heating were ignored. The entrainment ratios were constrained to decrease downward and exactly preserve conservation of mass. The entrainment ratios estimated by this procedure are 287.05, 8.473, 6.199, 5.520, 5.492, and 4.879 in the layers 87-105m, 105-110m, 115-450m, 450-1000m, 1000-1750m, and >1750m respectively. These are significantly higher than the values determined by *Lee et al.* [2002], which ranged from 9.95-3.78, apparently due to differences in the model structure and vertical velocity and mixing profiles.

Finally, the physical inverse model did not consider the seasonal thermocline (0-50 m). Here, to simulate surface primary production, a stationary, non-seasonal, surface mixed-layer similar to that used for the global ocean ICBM is added to the Black Sea model. The lower boundary of the mixed layer is taken to be 50 m, roughly the maximum extent of winter mixing and the uppermost level of the physical inverse model. The vertical velocity and eddy diffusivity at the base of the mixed layer are taken as the uppermost values computed by *Ivanov and Samodurov* [2001]. To circumvent the need for numerically expensive seasonal dynamics in multi-millennial simulations, the potential temperature of the second layer, representing the CIL, is fixed at 7.743°C.

6.4 *Boundary Conditions*

The Black Sea physical model was run coupled to the biogeochemistry submodel described in Section 3. The high resolution configuration shown here uses 183 vertical levels, with varying resolution from 1 meter at the oxic-anoxic interface to 300 meters below 1000 meters. Concentrations of components in the Bosphorus inflow are given in Table 6.1.

Surface gas fluxes were computed using the *Wanninkhof* [1992] U^2 relationship, assuming an annual basin-wide mean 10-m wind velocity of 3.5 m/s based on the 10m

Table 6.1. Concentrations of various components in the Bosphorus Inflow.

Parameter	Value (units)	Reference
Phosphate	1.09 µmol/kg	[*Tugrul and Polat*, 1995]
Oxygen	40 µmol/kg	R/V Knorr 2001 Leg 2 Stn. 1
Nitrate	9.05 µmol/kg	[*Tugrul and Polat*, 1995]
TCO_2	2710 µmol/kg	[*Hiscock and Millero*, 2006]
$\Delta^{14}C$	-65 ‰	[*Siani et al.*, 2000]
H_2S	0 µmol/kg	R/V Knorr 2001 Leg 2 Stn. 1
Labile DOC	0.05 µmol/kg	[S. Konovalov, pers. comm.]
Semi-Labile DOC	6 µmol/kg	[S. Konovalov, pers. comm.]
Microbial Populations	0 cells/L	-
θ	13.91°C	-
Salinity	36	-

European Centre for Medium-Range Weather Forecast [*Kara et al.*, 2005]. Since the CIL is seasonally ventilated during winter, surface gas exchange was calculated assuming an equilibrium temperature of 7.743°C. Surface DIC and $DI^{14}C$ equilibrium concentrations were calculated assuming preanthropogenic P_{CO2} (280 ppmv) and atmospheric $\Delta^{14}C$ (0 ‰), and a surface alkalinity of 3259.2 µeq/L [*Hiscock and Millero*, 2006]. Additional riverine inputs of DIC are included assuming an inflow of 300 km^3/yr and DIC concentration of 3114 µM [*Berner and Berner*, 1996a] and $\Delta^{14}C = 0$ ‰. Due to extensive eutrophication since the 1960s [*Cociasu et al.*, 1996; *Kideys*, 2002; *Mee*, 1992], appropriate preanthropogenic riverine inputs of nitrogen and phosphorus are more difficult to parameterize. Since the Danube nutrient discharge to the Black Sea has been reconstructed for the period 1950-2000 in the context of the daNUbs project [*Behrendt et al.*, 2005; *Schreiber et al.*, 2005], these data are used here. The daNUbs-estimated nutrient fluxes for the period prior to 1960 agree well with the data of *Almazov* [1961], with total

N and P discharges of 140 and 12 kt/year respectively. The Danube River accounts two-thirds of the total riverine inflow to the Black Sea [*Jaoshvili*, 2002] and it is thought to account for a similar fraction of nutrient inputs [*Cociasu et al.*, 1996; *Konovalov and Murray*, 2001]. Thus, assuming that the Danube accounts for 50-70% of total preindustrial nutrient inputs due to riverine and atmospheric inputs, the estimated total preindustrial N and P loading is 200-280 kt N yr^{-1} and 17-24 kt P yr^{-1} respectively. However, examination of 11 sediment cores from the Black Sea suggests a basin-integrated phosphorus accumulation rate of 47 kt P yr^{-1} for the 100 year period prior to 1950 [*Teodoru et al.*, 2007]. This suggests there remains at least a factor of two uncertainty in pre-1960 nutrient inputs.

6.5 *Black Sea Simulation Results*

The results of the default run are shown in Figure 6.5. Hydrographic observations from the 2001 and 2003 R/V Knorr cruises [*Murray*, 2006 <http://www.ocean.washington.edu/cruises/>] and $\Delta^{14}C$ measurements from the "Odysseus 65" expedition [*Östlund*, 1974] are shown in gray. To reduce the observational scatter due to dynamic displacement of isopycnal surfaces, it is customary to plot Black Sea hydrographic against potential density rather than depth [*Murray et al.*, 1995]. However, this convention tends to emphasize the upper water column, while compressing the deeper observations. Here the observations have been converted from density coordinates back to depth coordinates by interpolating between the spatial and climatological mean depths of selected isopycnal layers [*Basturk et al.*, 1994]. This method ensures both minimal scatter and a conventional graphical representation.

The physical circulation shows reasonable agreement with observations, as indicated by tight overlap of the simulated and observed salinity and temperature profiles. The exact profiles of simulated salinity and temperature are sensitive to the model resolution due to errors in the calculated entrainment of salt and heat. The magnitude of

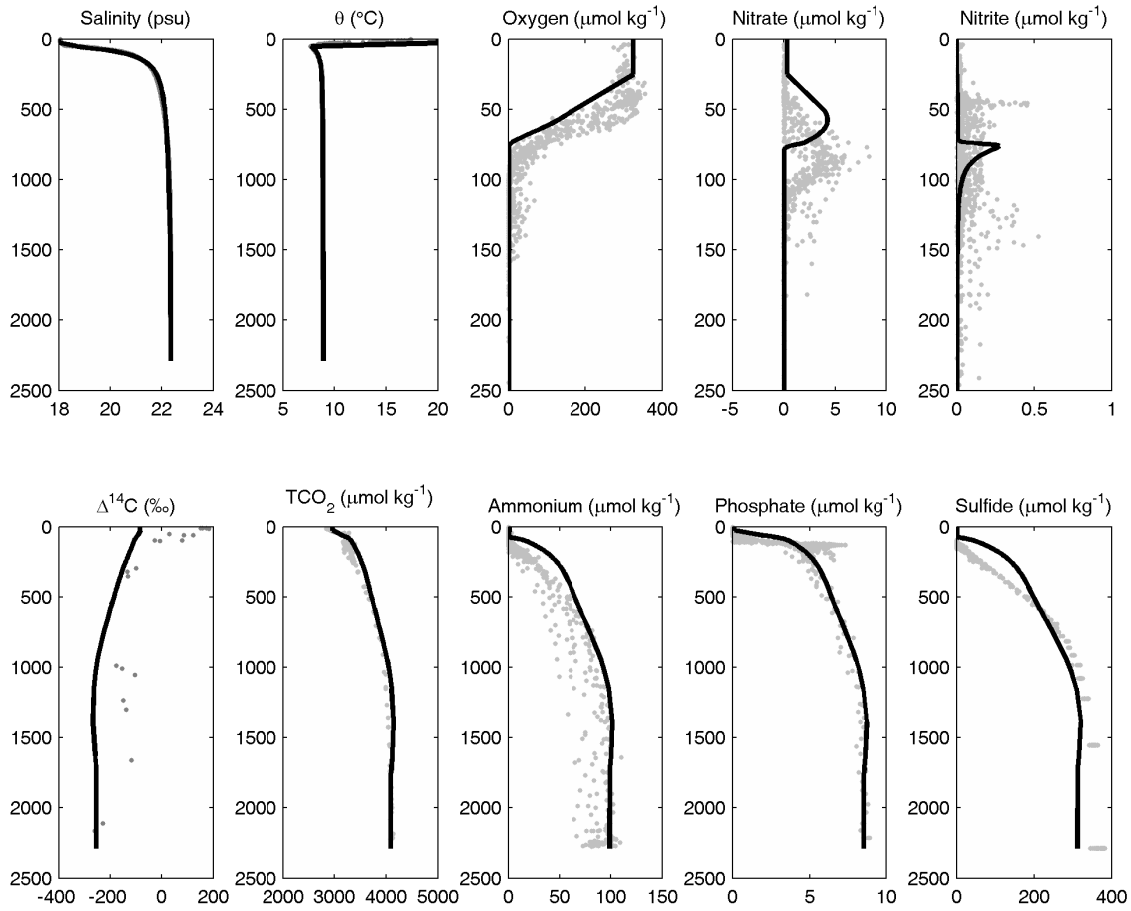

Figure 6.5. Comparison of simulation results (bold line) with observations (gray dots). The depths for observation points were calculated from the observed potential density and the basin-mean depth-density relationship. Salinity and potential temperature observations and simulations overlap.

this error is significantly reduced at the nominal resolution of 1 meter used in the default run here, resulting in close agreement between simulated and observed salinity and temperature. Simulated BBHL $\Delta^{14}C$ is also in agreement with observed values [*Östlund*, 1974]. The simulated mixed layer $\Delta^{14}C$, -82.31‰, is only slightly lower than estimated pre-bomb surface values of -55‰ to -74‰ from museum specimens of live-collected mollusks [*Siani et al.*, 2000]. The $\Delta^{14}C$ values observed by *Östlund* [1974] in the upper 250 meters are clearly the result of contamination with bomb radiocarbon. Between 1000 and 1700 meters, the model $\Delta^{14}C$ is 75-150‰ lighter than reported by *Östlund* [1974], but the scatter in the measurements and potential for bomb radiocarbon contamination make it difficult to interpret the significance of this discrepancy.

The overall trends in non-conservative components agree reasonably well with observations. Simulated BBHL ammonium and phosphate, 100.6 μM and 8.65 μM respectively, are well within the observational scatter. Simulated BBHL sulfide, 317.7 μM, is 60 μM lower than observed values. This is discrepancy is most likely the result of imposing classical *Redfield* [1958] C:N:P stoichiometry on sinking POM. C:N ratios observed in Black Sea POM range from 7.5 to 9.6 [*Burlalova et al.*, 1997; *Coban-Yildiz et al.*, 2006; *Yilmaz et al.*, 1998], 10-45% higher than the classical value of 106:16 [*Redfield*, 1958]. Examination of the correlation between deep euxinic H_2S, NH_4^+, and PO_4^{3-} suggests a long-term average POM stoichiometry of C:N:P = 130:16:1 [*Hiscock and Millero*, 2006], or C:N = 8.12. Applying a correction factor of (130/16)/(106/16) = 1.22 to the simulated H_2S exactly recovers the observed BBHL values, but exacerbates disagreement between 100-500 meters.

The current version of the Black Sea model is unable to reproduce all of the detailed structure of the suboxic layer. The simulated upper boundary of the suboxic layer occurs at 76 meters, within the range of observed depth range of 68-208 meters, but above the 94 meter mean depth of the $\sigma_\theta = 15.65$ isopycnal used to define the upper boundary of

the SOL [*Murray et al.*, 1995]. In the model, the lower boundary of the SOL is compressed upward, with much steeper gradients of sulfide and ammonium than observed in the data. Simulated O_2 and H_2S do not coexist at concentrations greater than 1 μmol/kg, but both components approach zero at a depth of 76 meters. The upward shift in the depths of the nitrate and secondary nitrite maxima is also a result of the compression of the SOL. The reasons for these discrepancies seem well understood. Similar results for Black Sea biogeochemical models which do not include explicit manganese and iron cycling [*Oguz et al.*, 2001]. In the Black Sea, measurements of dissolved and particulate iron and manganese [*Landing and Lewis*, 1991; *Lewis and Landing*, 1991; *Spencer and Brewer*, 1971; *Trouwborst et al.*, 2006; *Yemenicioglu et al.*, 2006] in combination with numerical simulations [*Konovalov et al.*, 2004; *Konovalov et al.*, 2006; *Oguz et al.*, 2001; *Yakushev et al.*, 2007] suggest that oxidation of the upward flux H_2S does not occur by dissolved oxygen, but instead is mitigated by the cycling of trace metal species. Specifically, dissolved Fe^{2+} and Mn^{2+} are transported to the upper SOL by diffusion and advection where they are oxidized by oxygen and nitrate, forming $Fe(III)(OH)_3$, $Mn(IV)O_2$, and Mn(III) species. Because of their low solubility, iron and manganese oxides quickly form solid particles which sink back down to the lower SOL where they again reduced by oxidation of H_2S. The cycle is thought to be responsible for the formation of the SOL layer itself, separating the oxic and euxinic layers by tens of meters [*Murray et al.*, 1995]. Absorption of phosphate onto metal oxides is also thought to be the process responsible for the formation of the so-called “phosphate dipole,” the strong minimum and maximum clearly observable in the phosphate profile at the depth of the chemocline [*Shaffer*, 1986].

Table 6.2. Calculated Black Sea Organic Carbon Fluxes (g C m^{-2} yr^{-1})

Parameter	Model	Literature Value	Reference
Central Gyre Primary Production	96	40-214 87-284 210	*[Yilmaz et al., 2006] and therein* [*McCarthy et al.*, 2007] [*Karl and Knauer*, 1991]
Shelf Primary Production	192	94-584	Yilmaz et al. (2006) *and therein*
Particulate Export Production (across 50 meters)	29	51 (60 m)	[*Karl and Knauer*, 1991]
Flux to Sediments (<100 m)	49	50-118 (NW Shelf)	[*Gregoire and Friedrich*, 2004]
Burial (<100 m)	10	4.6 7.5 (NW Shelf)	[*Teodoru et al.*, 2007] [*Gregoire and Friedrich*, 2004]
Flux to Sediments (>100 m)	3.6	1.4-4.7 (1200 m Sed. Trap)	[*Hay et al.*, 1990]
Burial (>100 m)	0.10	2.7	[*Teodoru et al.*, 2007]

6.5.1 *Rates of Simulated Processes in the Black Sea.*

The simulated rates of numerous Black Sea processes were compared against measured and estimates rates from the literature (Table 6.2-Table 6.5). Measured rates of primary production in the Black Sea demonstrate spatial, seasonal, and interannual variability [e.g.*Yilmaz et al.*, 2006; *Yunev et al.*, 2002]. The observed seasonal bloom cycle is typically characterized as a single winter-early spring bloom between November and March [*Yunev et al.*, 2002] or a fall and early spring bloom[*Chu et al.*, 2005]. Rates measured in coastal regions and especially on the Northwest Shelf are typical higher than rates in the central region of the sea [*Yilmaz et al.*, 2006]. The ability to use satellite chlorophyll observations to supplement *in situ* primary production measurements is hampered by a significant and apparently variable overestimation of chlorophyll a concentration by standard SeaWIFS algorithms [*Sancak et al.*, 2005; *Suetin et al.*, 2002; *Suetin et al.*, 2004] by a factor of 2-4 [*McCarthy et al.*, 2007; Oguz et al., 2003; Oguz and

Ediger, 2006]. The simulated annual average rate of open water productivity, 96 g C m^{-2} yr^{-1}, is consistent with the above observations to within their uncertainty. In order to achieve realistic nutrient burial rates and basin-wide nutrient budgets, it was necessary to parameterize enhanced coastal production in both the Black Sea and Global Ocean models. In the Black Sea model, this value is set at 2 times open water productivity for regions of less than 100 meters depth. Thus, the simulated coastal productivity (192 g C m^{-2} yr^{-1}) is also consistent with estimates of primary production on the shelf.

The simulated particle export ratio past 50 meters (25%) is very similar to that measured by for a sediment trap at 60 meters [*Karl and Knauer*, 1991], however the simulated particle flux attenuation (based on [*Martin et al.*, 1987]) was much slower than the very rapid flux attention observed by *Karl and Knauer* [1991] between 60 and 250 meters. The simulated and measured particle export ratio past 350 meters become more similar again, 7% and 4% respectively. The resulting simulated flux of organic carbon to the bottom for the shelf region (<100 m) was similar to the lower range estimated for the Northwest Shelf on an areal basis [*Gregoire and Friedrich*, 2004]. I am unaware any direct empirical estimates of the organic carbon flux to the deep Black Sea sediments, however the model-estimated flux was similar to the annual average organic carbon flux measured in sediment trap at 1200 meters in the southwestern Black Sea [*Hay et al.*, 1990]. The simulated carbon burial on the shelf is higher than literature estimates, while much lower than literature estimates for the deep basin. This pattern might be explained by downslope transfer of organic matter by gravity currents responsible for the numerous turbidite deposits on the abyssal plain [*Canfield et al.*, 1996; *Konovalov et al.*, 2007; *Lyons and Berner*, 1992], a process not included in the model.

Table 6.3. Calculated Black Sea Nitrogen Fluxes (Units are kt N yr^{-1}, 1 kt = 10^9 g)

Parameter	Model	Literature Value[a]	Reference
Natural Atmospheric and Riverine Inputs (DIN)	200	140 (Danube, 1956) 200 (Danube, 1956) 756 (NW Shelf, 2007)	[*Almazov*, 1961] [*Behrendt et al.*, 2005] [*McCarthy et al.*, 2007]
Riverine Semi-Labile DON	95	84±40	[*Becquevort et al.*, 2002; *Ducklow et al.*, 2007]
Bosphorus Inflow (DIN) (Semi-Labile DON)	30.2 3.8	41.2	[*Tugrul and Polat*, 1995]
Bosphorus Outflow (DIN) (Semi-Labile DON)	13.3 155	15.2	[*Tugrul and Polat*, 1995]
N-Fixation	1935	462 1000-2100	[*McCarthy et al.*, 2007] [*Sorokin*, 2002]
Pelagic Denitrification	14.4	32 7	[*Ward and Kilpatrick*, 1991] [*McCarthy et al.*, 2007]
Pelagic Anammox	28.9	110 728	[*Kuypers et al.*, 2003] [*McCarthy et al.*, 2007]
Pelagic Thiodenitrification	1843	3160 (model)	[*Yakushev et al.*, 2007]
Benthic Denitrification	105.8	324 (NW Shelf)	[*Gregoire and Friedrich*, 2004]
Burial (<100 m)	99.4	81 57 (NW Shelf)	[*Teodoru et al.*, 2007] [*Gregoire and Friedrich*, 2004]
Burial (> 100 m)	4.2	60	[*Teodoru et al.*, 2007]

[a] When necessary, literature estimates were converted to standard units using the following assumptions: Mixed/Euphotic Zone Area, 4.1×10^{11} m^2; Mixed/Euphotic Zone Thickness, 50 m; Suboxic Layer Area, 3.1×10^{11} m^2; Suboxic Layer Thickness, 10 m; Density of Seawater, 1000 kg/m^3. All processes were assumed to occur year-round, except for nitrogen fixation, which was calculation assuming a 6 month period.

Simulated nitrogen inputs and phosphorus inputs to the Black Sea (Table 6.3. -Table 6.4) were chosen to be similar to the best estimates of background inputs, taken as1956 values [*Almazov*, 1961]. Inflow and outflow of nutrients through the Bosphorus are for the period from 1986-1992 [*Tugrul and Polat*, 1995], as there appear to be no earlier data. Simulated dissolved inorganic nitrogen (DIN) and phosphorus (DIP) outflow through the surface waters of the Bosphorus are in good agreement with observations. This further

Table 6.4. Calculated Black Sea Phosphorus Fluxes (kt P yr^{-1}, 1 kt = 10^9 g)

Parameter	Model	Literature Value	Reference
Natural Riverine and Atmospheric Inputs	17.1	12 18	[*Almazov*, 1961] [*Behrendt et al.*, 2005]
Bosphorus Input	10.7	8.9	[*Tugrul and Polat*, 1995]
Bosphorus Output	11.1	9.8	[*Tugrul and Polat*, 1995]
Burial (<100 m)	16.6	33	[*Teodoru et al.*, 2007]
C:P Burial (Aerobic)	132	41-71	[*Teodoru et al.*, 2007]
Burial (>100 m)	0.23	14	[*Teodoru et al.*, 2007]
C:P Burial (Euxinic)	400	86-474	[*Teodoru et al.*, 2007]

suggests that the simulated annual average primary productivity is a reasonable approximation of the real seasonal variations averaged over the course of the year. Simulated burial of N and P in the deep Black Sea (>100 meters) were both considerably lower than estimated by analysis of sediments cores [*Teodoru et al.*, 2007]. This is consistent with the importance of gravity currents for transporting shelf materials to the deep basin sediments. Simulated burial of reactive nitrogen in shelf sediments was slightly higher than other estimates, again consistent with the importance of off-shelf transport of sediments, but was not high enough to account for the total difference between simulated and observed deep water burial rates. The burial of phosphorus in shelf sediments was only half that found by *Teodoru et al.* [2007]. Because simulated P-burial is considerably lower than estimated by *Teodoru et al.* [2007] in both shelf and deep sediments, the model budget can only be reconciled with their observations if background P-inputs to the Black Sea were considerably higher than estimated here, or if *Teodoru et al.* [2007] overestimate basin wide rates of phosphorus burial. Simulated benthic denitrification was found to be much lower than estimated by *Grégoire and Friedrich*

[2004]. However, their estimate was made only from measurements on the Northwest Shelf during the warm summer months when sediment denitrification rates are likely to be highest. Moreover, the Northwest Shelf has recently experienced more than two decades of intense eutrophication [*Cociasu et al.*, 1996; *Yunev et al.*, 2007], so it is possible that the modern benthic denitrification rates are elevated higher than long term mean values.

The remaining terms in the Black Sea nitrogen cycle involve the balance of surface nitrogen fixation with various denitrification processes in the suboxic layer, including classical denitrification, anammox, and thiodenitrification. We estimate the total rate of all pelagic denitrification processes at 1886 kt N/yr and the total rate of nitrogen fixation at 1935 kt N/yr. Because the current model assumes that all N-reduction results in the production of N_2 instead of continuing to NH_4^+, these should be considered upper limits. The current version of the model predicts most of the majority of the denitrification to occur via thiodenitrification, with smaller contributions from anammox and classical denitrification. The simulated rate of anammox is about twice that of classical denitrification. However, results from field observations and models which include manganese cycling suggest that a significant fraction of the downward flux of nitrate is spent oxidizing dissolved Mn(II) [*Konovalov et al.*, 2006], a process not included in the current version of the model. Additionally, without manganese chemistry the model is unable to correctly represent the suboxic zone which likely suppresses predicted anammox rates. However, the overall rate of denitrification-like processes, and thus nitrogen fixation, should be less sensitive to these uncertainties since the rate of total denitrification is well constrained by the transport divergence.

The ICBM model budget for the Black Sea produces estimates of nitrogen fixation and total denitrification (classical denitrification, anammox, and thiodenitrification) which are roughly a factor of two higher than those proposed by *McCarthy et al* [2007], after

Table 6.5. Black Sea Sulfur Fluxes (Units are as indicated in the first column)

Parameter (Units)	Model	Literature Value	Reference
Pelagic Sulfate Reduction (nMol S d^{-1})	0.12-18.0	3-36 0.12-3.5	[*Jorgensen et al.*, 1991] [80-100 m] [*Albert et al.*, 1995][>100 meters]
Integrated Areal Pelagic Sulfate Reduction (mol S m^{-2} yr^{-1})	0.80	0.08-0.42 2.28-5.36 1.29-2.82	[*Albert et al.*, 1995] [*Sorokin*, 2002] [*Lein and Ivanov*, 1991]
Benthic Sulfate Reduction (Euxinic, mol S m^{-2} yr^{-1})	0.077–2.05	0.073-0.88	*[Weber et al., 2001] and therein*
Mean Benthic SO_4^{2-} Red. (Euxinic, mol S m^{-2} yr^{-1})	0.29	0.219 0.548	[*Lein and Ivanov*, 1991] [*Weber et al.*, 2001]
Sulfide Oxidation by O_2 (mol S m^{-2} yr^{-1})	0.86	0.26	[*Konovalov et al.*, 2006]
Sulfide Oxidation by NO_3^- (mol S m^{-2} yr^{-1})	0.27	0.03	[*Konovalov et al.*, 2006]

accounting for the difference in riverine inputs due to anthropogenic inputs. One possibility for the difference between the two budgets is that *McCarthy et al* [2007] does not consider the potential contribution from thiodenitrification, which both the ICBM model here and the ROLM model [*Yakushev et al.*, 2007] suggest might be a very large sink. However, I am unaware of any measurements of marine pelagic thiodenitrification in the Black Sea or elsewhere, which is certainly a potent criticism of this hypothesis. Moreover, the current parameterization of thiodenitrification is based entirely upon the aerobic oxidation of sulfide, since other kinetic data is not available. Since many of the numbers in Table 6.3. are based on as little as a single data point, it seems impossible to reconcile various Black Sea nitrogen budgets at this point without more observations.

Like the ICBM nitrogen cycle, the simulated sulfur budget (Table 6.5) may improperly state the relative importance several sulfide oxidation pathways. In particular, absence of Mn-cycling distorts the relative importance of various sulfide oxidation processes, though the overall rate of sulfide production and consumption is constrained by the transport and should be simulated more accurately. Simulated benthic and pelagic

sulfate reduction rates are in good agreement with observations. Simulated H_2S oxidation by O_2 and NO_3 at the oxic-anoxic interface account for 65% and 23% of total H_2S oxidation respectively. The remaining sulfide is oxidized by oxygen and nitrate in lateral intrusions of Bosphorus Plume waters below the anoxic-oxic interface, accounting for 11% and 2% of total sulfide oxidation. In contrast, *Konovalov et al.* [2006] finds that the lateral flux of oxygen accounts for 60% of total H_2S oxidation and that oxidation of H_2S by O_2 in the SOL accounts for less than 0.5% of total H_2S oxidation. These differences can be explained by a higher oxygen concentration in the entrained portion of the Bosphorus Plume in the *Konovalov et al.* [2006] simulations due to a deeper chemocline depth, and the mitigation of H_2S oxidation by MnO_2 in the SOL.

6.6 *Discussion*

The model can capture the major features of the Black Sea biogeochemistry provided with appropriate hypsometry and circulation, including rates of primary production, deep water concentrations of various species, and overall budgets of C, N, P, and S. Only slight modifications are required to adapt the model from the Global Ocean to the Black Sea. The most substantial change required consideration of the annual temperature range experienced in the basin, and adapting the nitrogen fixation representation accordingly. Overall, the ICBM biogeochemical model performs quite well in the Black Sea, demonstrating that the model has the basic capability to simulate the entire basin redox range from well-oxygenated to euxinic.

At present, the model captures only the first order details of the suboxic zone. Addition of simulated manganese- and iron-cycling is expected to improve the detailed structure of this region. The importance of Mn cycling in the Black Sea is driven by the high Mn(II) concentration which has accumulated in the euxinic deep water due to efficient recycling of $MnCO_3$ and $MnO(OH)_2$ from the sediments [*Konovalov et al.*, 2007]. This may be a bad analogy for open ocean paleooceanographic settings, where

manganese inputs could be substantially lower and high-latitude ventilation could result in oxic bottom waters underlying a euxinic OMZ. Under these conditions, maganese would probably undergo much more efficient burial in the deep oxic sediments. Mechanistic modeling of Mn precipitation and dissolution kinetics and sediment diagenesis will be required to further address these possibilities. The ability to improve the model of the ICBM nitrogen cycle for the Black Sea depends heavily on the availability of direct rate measurements for various competing processes and pathways at relatively dense temporal and spatial spacing. This suggests the need for a process cruise to the Black Sea similar in size and duration to the JGOFS Arabian Sea study.

APPENDIX A

ADDITIONAL KINETIC PARAMETERS

Table A.1. Addition Microbial Kinetic Parameters (Augments Parameters Found in the Text)

Parameter	Symbol	Value	Units	Reference
Primary Production				
Phytoplankton maximum growth rate	μ_{PP}	91.25	yr^{-1}	[*Tyrrell*, 1999]
Diazotroph phytoplankton maximum growth rate	μ_{NF}	87.6	yr^{-1}	[*Tyrrell*, 1999]
Half-saturation constant for phosphate uptake	K_P	0.03	$\mu mol\ kg^{-1}$	[*Tyrrell*, 1999]
Half-saturation constant for NO3- or NO2- uptake	K_{Nox}	0.75	$\mu mol\ kg^{-1}$	[*Gruber et al.*, 2006]
Half-saturation constant for NH4+ uptake	K_{Nred}	0.50	$\mu mol\ kg^{-1}$	[*Gruber et al.*, 2006]
Minimum [PO43-] for high-latitude uptake	$PO_4^{3-}{}_{min}$	1.5	$\mu mol\ kg^{-1}$	-
Heterotrophic Remineralization				
Bacterial growth efficiency (Yield)	Y	0.24	unitless	
Maximum growth rate using oxygen	μ_{max,O_2}	0.21	hr^{-1}	Derived from [*Bendtsen et al.*, 2002]
Maximum growth rate using nitrate	μ_{max,NO_3^-}	0.05	hr^{-1}	Scaled from [*Kornaros and Lyberatos*, 1998]
Maximum growth rate using nitrite	μ_{max,NO_2^-}	0.05	hr^{-1}	Scaled from [*Kornaros and Lyberatos*, 1998]
Maximum growth rate using sulfate	$\mu_{max,SO_4^{2-}}$	0.05	hr^{-1}	Scaled from [*Kornaros and Lyberatos*, 1998]
LDOC half-saturation constant using oxygen	K_{S,O_2}	45	$\mu mol\ kg^{-1}$	Derived from [*Bendtsen et al.*, 2002]
LDOC half-saturation constant using nitrate	K_{S,NO_3^-}	250	$\mu mol\ kg^{-1}$	Scaled from [*Kornaros and Lyberatos*, 1998]
LDOC half-saturation constant using nitrite	K_{S,NO_2^-}	185	$\mu mol\ kg^{-1}$	Scaled from [*Kornaros and Lyberatos*, 1998]
LDOC half-saturation constant using sulfate	$K_{S,SO_4^{2-}}$	185	$\mu mol\ kg^{-1}$	Scaled from [*Kornaros and Lyberatos*, 1998]
Oxygen half-saturation constant using oxygen	K_{O_2}	2	$\mu mol\ kg^{-1}$	-
Oxygen inhibition constant using nitrate	K_{I1,O_2}	2.75	$\mu mol\ kg^{-1}$	-

Oxygen inhibition constant using nitrite	K_{I2,O_2}	0.05	µmol kg^{-1}	-
Oxygen inhibition constant using sulfate	K_{I3,O_2}	0.001	µmol kg^{-1}	-
Nitrate half-saturation constant using nitrate	$K_{NO_3^-}$	10	µmol kg^{-1}	[*Christensen et al.*, 1989]
Nitrate inhibition constant using nitrite	K_{I1,NO_3^-}	625	µmol kg^{-1}	-
Nitrate inhibition constant using sulfate	K_{I2,NO_3^-}	10	µmol kg^{-1}	-
Nitrite half-saturation constant using nitrite	$K_{NO_2^-}$	20	µmol kg^{-1}	-
Nitrite inhibition constant using sulfate	K_{I1,NO_2^-}	20	µmol kg^{-1}	-
Sulfate half-saturation constant using sulfate	$K_{SO_4^{2-}}$	240	µmol kg^{-1}	-
Nitrification				
Maximum growth rate of AOB	μ_{AOB}	350	yr^{-1}	[*Jetten et al.*, 2001]
Maximum growth rate of NOB	μ_{NOB}	350	yr^{-1}	[similar to AOB, *Prosser*, 1989]
Ammonium half-saturation constant of AOB	$K^{AOB}_{NH_4^+}$	0.15	µmol kg^{-1}	[*Hashimoto et al.*, 1983]
Nitrite half-saturation constant of NOB	$K^{NOB}_{NO_2^-}$	0.07	µmol kg^{-1}	[*Olson*, 1981a]
Oxygen half-saturation constant of AOB	$K^{AOB}_{O_2}$	23	µmol kg^{-1}	[*Guisasola et al.*, 2005]
Oxygen half-saturation constant of NOB	$K^{NOB}_{O_2}$	55	µmol kg^{-1}	[*Guisasola et al.*, 2005]
Anammox (AMX)				
Maximum growth rate of AMX	μ_{AMX}	26	yr^{-1}	[*Jetten et al.*, 2001]
Ammonium half-saturation constant of AMX	$K^{AMX}_{NH_4}$	5	µmol kg^{-1}	[*Jetten et al.*, 2001]
Nitrite half-saturation constant of AMX	$K^{AMX}_{NO_2}$	3	µmol kg^{-1}	-
Oxygen inhibition constant of AMX	$K^{AMX}_{O_2}$	0.05	µmol kg^{-1}	-

APPENDIX B

CONSTRUCTION OF THE TRANSPORT MATRIX

This section provides a brief example demonstrating the construction of the transportation matrix for a five-reservoir test problem shown in Figure A.1.

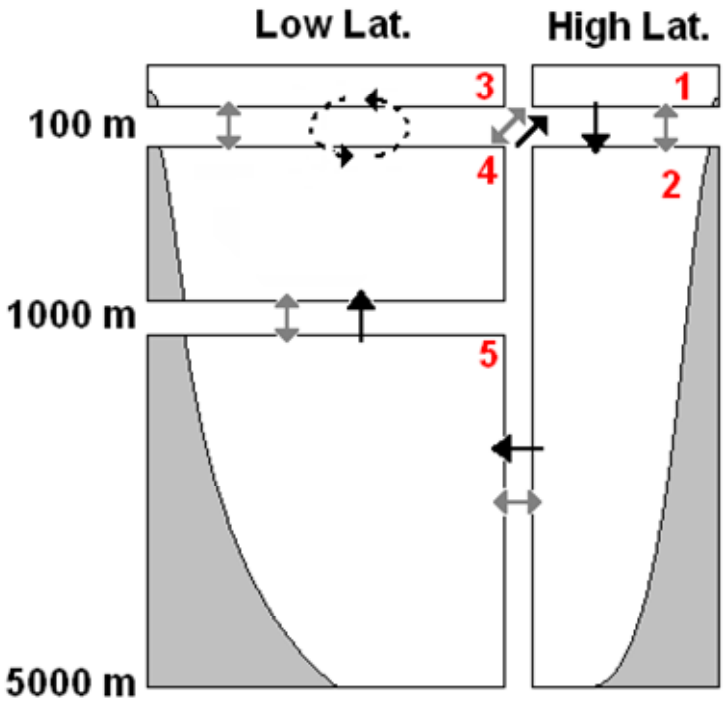

Figure B.1. Sample 5-box model used for this example. Black arrows represent advective processes. Gray arrows represent mixing processes.

The problem represents thermohaline ventilation of the deep ocean (dark unidirectional arrows), isopycnal and diapycnal mixing (gray arrows), and gyre thermocline ventilation by subduction (dotted arrows). I will denote the thermohaline flux magnitude F_{THC} (m^3/yr) and the subduction flux F_{SV} (m^3/yr). Isopycnal mixing is represented by K_H (m^2/yr) and diapycnal mixing, K_Z (m^2/yr), is given by:

$$K_Z = K_Z^{Surf} + \frac{\left(K_Z^{Deep} - K_Z^{Surf}\right)}{2}\left(1 + \tanh\frac{z-1000}{300}\right) \qquad \text{B-1}$$

which smoothly transitions from K_Z^{Surf} to K_Z^{Deep} at 1000 m depth. Vertical diffusion at 100m and 1000m will then be denoted K_Z^{100} and K_Z^{1000} respectively over the interface area, A_{ij}, the area of the surface between reservoir *i* and reservoir *j*. The entire transportation matrix is given by Equation A-2, the various elements of which are constructed below.

$$\mathbf{T} = \mathbf{T}_{advection} + \mathbf{T}_{Z-diffusion} + \mathbf{T}_{H-diffusion} + \mathbf{T}_{Non-local} \qquad \text{B-2}$$

$$\mathbf{T}_{advection} = \begin{bmatrix} -\frac{F_{THC}}{V_1} & 0 & 0 & \frac{F_{THC}}{V_1} & 0 \\ \frac{F_{THC}}{V_2} & -\frac{F_{THC}}{V_2} & 0 & 0 & 0 \\ 0 & 0 & 0 & 0 & 0 \\ 0 & 0 & 0 & -\frac{F_{THC}}{V_4} & \frac{F_{THC}}{V_4} \\ 0 & \frac{F_{THC}}{V_5} & 0 & 0 & -\frac{F_{THC}}{V_5} \end{bmatrix}$$

$$\mathbf{T}_{Z-diffusion}=$$

$$\begin{bmatrix} -\frac{2A_{12}K_Z^{100}}{V_1(100+4900)} & \frac{2A_{12}K_Z^{100}}{V_1(100+4900)} & 0 & 0 & 0 \\ \frac{2A_{12}K_Z^{100}}{V_2(100+4900)} & -\frac{2A_{12}K_Z^{100}}{V_2(100+4900)} & 0 & 0 & 0 \\ 0 & 0 & -\frac{2A_{34}K_Z^{100}}{V_3(100+900)} & \frac{2A_{34}K_Z^{100}}{V_3(100+900)} & 0 \\ 0 & 0 & \frac{2A_{34}K_Z^{100}}{V_4(100+900)} & -\frac{2A_{34}K_Z^{100}}{V_4(100+900)}-\frac{2A_{45}K_Z^{1000}}{V_4(900+4000)} & \frac{2A_{45}K_Z^{1000}}{V_4(900+4000)} \\ 0 & 0 & 0 & \frac{2A_{45}K_Z^{1000}}{V_5(900+4000)} & -\frac{2A_{45}K_Z^{1000}}{V_5(900+4000)} \end{bmatrix}$$

$$\mathbf{T}_{H-diffusion}=$$

$$\begin{bmatrix} -\frac{K_H(100+900)}{2V_1} & 0 & 0 & \frac{K_H(100+900)}{2V_1} & 0 \\ 0 & -\frac{K_H(4900+4000)}{2V_2} & 0 & 0 & \frac{K_H(4900+4000)}{2V_2} \\ 0 & 0 & 0 & 0 & 0 \\ \frac{K_H(100+900)}{2V_4} & 0 & 0 & -\frac{K_H(100+900)}{2V_4} & 0 \\ 0 & \frac{K_H(4900+4000)}{2V_5} & 0 & 0 & -\frac{K_H(4900+4000)}{2V_5} \end{bmatrix}$$

$$\mathbf{T}_{Non-local}=$$

$$\begin{bmatrix} 0 & 0 & 0 & 0 & 0 \\ 0 & 0 & 0 & 0 & 0 \\ 0 & 0 & -\frac{F_{NL}}{V_3} & \frac{F_{NL}}{V_3} & 0 \\ 0 & 0 & \frac{F_{NL}}{V_4} & -\frac{F_{NL}}{V_4} & 0 \\ 0 & 0 & 0 & 0 & 0 \end{bmatrix}$$

Note that in this simple case, the non-local mixing is equivalent to additional isopycnal mixing. One can envision the general case by further subdividing reservoir 4, which would result in fluxes between the surface and non-adjacent deeper reservoirs to simulated ventilation along outcropping isopycnal surfaces.

APPENDIX C

NUMERICAL INTEGRATION EXAMPLE

This section provides a brief example demonstrating the integration of two coupled linear differential equations using the first order backwards differentiation formula. This method is conceptually quite similar to the solution of the ICBM model using the variable-order solver ode15s which is based on the numerical differentiation formulas.

Consider the well-posed initial value problem find $\mathbf{y}(t)$ subject to:

$$\mathbf{F}(t, y) = \frac{\partial \mathbf{y}}{\partial t} = \begin{bmatrix} -\frac{1}{2} y(1) \\ \\ \frac{1}{2} y(1) \end{bmatrix} \qquad \mathbf{y}(0) = \begin{bmatrix} 1 \\ \\ 0 \end{bmatrix} \qquad \text{C-1}$$

The first-order backwards differentiation formula (BDF1) can be used to solve this problem by breaking the $\mathsf{interval}(0,t)$ into one or more time steps of duration τ and iterating once for each step. Inserting appropriate constants for BDF1 (Ashino et al, 2000) into Equation 4-8 yields the formula:

$$\frac{\mathbf{y}_{n+1} - \mathbf{y}_n}{\tau} = \mathbf{F}(t_{n+1}, \mathbf{y}_{n+1}) \qquad \text{C-2}$$

The problem then is reduced to solving Equation B-2 for y_{n+1} at each time step. In the simple case posed by this example, the solution can be found by trivial algebraic manipulation:

$$\mathbf{y}_{n+1} = \begin{bmatrix} \frac{2}{2+\tau} y_n(1) \\ \\ \frac{\tau}{2+\tau} y_n(1) + y_n(2) \end{bmatrix} \qquad \text{C-3}$$

but such an approach will not be possible for general $\mathbf{F}(t, y)$, which may be nonlinear. Instead we require an iterative solution to the problem. Equation 4-12 provides a formula for an initial estimate of $\mathbf{y}_{n+1}$, denoted $\mathbf{y}_{n+1}^{(0)}$, based only on the previous time steps. However, for the initial iteration no previous results are available. In this case, one can estimate $\mathbf{y}_{n+1}^{(0)}$ via one or more forward Euler steps:

$$\mathbf{y}_{n+1}^{(0)} = \mathbf{y}_0 + \tau \cdot \mathbf{F}(0, \mathbf{y}_0) \qquad \text{C-4}$$

Given a sufficiently accurate initial estimate, the Newton-Raphson method can then be used to improve the estimate via a series of corrections, denoted $\Delta^{(i)}$:

$$\mathbf{y}_{n+1}^{(i+1)} = \mathbf{y}_{n+1}^{(i)} + \Delta^{(i)} \qquad \text{C-5}$$

The unknown corrections can be found by solving:

$$0 = \tau\, \mathbf{F}\left(t_{n+1}, \mathbf{y}_{n+1}^{(i)}\right) - \mathbf{y}_{n+1}^{(i)} + \mathbf{y}_n + \left[\tau\, \mathbf{J}\left(t_{n+1}, \mathbf{y}_{n+1}^{(i)}\right) - \mathbf{I}\right]\Delta^{(i)} \qquad \text{C-6}$$

where $\mathbf{J}$ is the Jacobian matrix of $\mathbf{F}(t, y)$ or a close approximation, and $\mathbf{I}$ is the identity matrix. The algorithm proceeds by iterating on Equation B-2, performing an internal Newton-Raphson iteration (B-5 and B-6) during each time-stepping iterate, until the end of the integration is reached.

Note that production quality implementations of these methods are considerably more sophisticated than indicated in this example, allowing for absolute and relative error control, variable-sized time steps and variable method order, optimized initialization sequences. Extensive details pertaining to ode15s are provided by [*Ashino et al.*, 2000; *Shampine*, 1994; *Shampine and Reichelt*, 1997; *Shampine*, 2005; *Shampine et al.*, 2005b].

WORKS CITED

Albert, D. B., et al. (1995), Sulfate reduction rates and low molecular weight fatty acid concentrations in the water column and surficial sediments of the Black Sea, *Deep-Sea Research Part I-Oceanographic Research Papers*, *42*(7), 1239-1260.

Almazov, N. M. (1961), Discharge of dissolved nutrients by rivers of the USSR to the Black Sea, *Naukovi Zapiski Odesskoy Biologicheskoy Stantsii (Scientific Notes of the Odessa Biological Observatory)*, *3*, 99-107 (in Russian).

Anbar, A. D., and A. H. Knoll (2002), Proterozoic ocean chemistry and evolution: a bioinorganic bridge?, *Science*, *297*, 1137-1142.

Anderson, L. D., et al. (2001), Carbon to phosphorus ratios in sediments: Implications for nutrient cycling, *Global Biogeochemical Cycles*, *15*(1), 65-79.

Archer, D., et al. (2000), What caused the glacial/interglacial atmospheric pCO(2) cycles?, *Reviews of Geophysics*, *38*(2), 159-189.

Arens, S., and A. Kleidon (2007), Modelling the biospheric influence on the weathering rate of silicate rocks in an EMIC, *Geochimica Et Cosmochimica Acta*, *71*(15), A34-A34.

Arnold, G. L., et al. (2004), Molybdenum isotope evidence for widespread anoxia in mid-Proterozoic oceans, *Science*, *304*, 87-90.

Ashino, R., et al. (2000), Behind and beyond the MATLAB ODE suite, *Comput. Math. Appl.*, *40*(4-5), 491-512.

Aumont, O., et al. (2003), An ecosystem model of the global ocean including Fe, Si, P colimitations, *Global Biogeochemical Cycles*, *17*(2), 26.

Azam, F., and D. Smith (2001), "Bacteria abundance, Thymidine and Leucine incorporation." United States JGOFS Data Server. Woods Hole Oceanographic Institution, USA: U.S. JGOFS Data Management Office, iPub: 9 July 2001. Accessed: 4 April 2008. http://usjgofs.whoi.edu/jg/dir/jgofs/arabian/.

Bacastow, R. B. (1996), The effect of temperature, change of the warm surface waters of the oceans on atmospheric CO2, *Global Biogeochemical Cycles*, *10*(2), 319-333.

Baines, W. D., et al. (1993), Turbulent fountains in a closed chamber, *J. Fluid Mech.*, *255*, 621-646.

Bartley, J. K., and L. C. Kah (2004), Marine carbon reservoir, C-org-C-carb coupling, and the evolution of the Proterozoic carbon cycle, *Geology*, *32*, 129-132.

Basturk, O., et al. (1994), Vertical variations in the principle chemical properties of the Black Sea in the autumn of 1991, *Marine Chemistry*, *45*(1-2), 149-165.

Becquevort, S., et al. (2002), The seasonal modulation of organic matter utilization by bacteria in the Danube-Black Sea mixing zone, *Estuar. Coast. Shelf Sci.*, *54*(3), 337-354.

Behrendt, H., et al. (2005), Point and diffuse nutrient emissions and loads in the transboundary Danube River Basin - II. Long-term challenges, *Archiv fur Hydrobiologie Suppl.*, *158*(1-2), 221-247.

Bendtsen, J., et al. (2002), Influence of bacterial uptake on deep-ocean dissolved organic carbon, *Global Biogeochemical Cycles*, *16*(4), 1127.

Benitez-Nelson, C. R. (2000), The biogeochemical cycling of phosphorus in marine systems, *Earth-Science Reviews*, *51*(1-4), 109-135.

Berner, E. K., and R. A. Berner (1996a), *Global Environment*, Prentice Hall, Upper Sadler River, NJ. Table 5.7. pg. 190.

Berner, E. K., and R. A. Berner (1996b), *Global Environment*, 376 pp., Prentice Hall, Englewood Cliffs, New Jersey.

Bjerrum, C. J., and D. E. Canfield (2004), New insights into the burial history of organic carbon on the early Earth, *Geochem. Geophys. Geosyst.*, *5*, 9.

Bjerrum, C. J., et al. (2006), Modeling organic carbon burial during sea level rise with reference to the Cretaceous, *Geochem. Geophys. Geosyst.*, *7*, 24.

Blanke, B., et al. (1999), Warm water paths in the equatorial Atlantic as diagnosed with a general circulation model, *Journal of Physical Oceanography*, *29*(11), 2753-2768.

Bloomfield, L. J., and R. C. Kerr (1999), Turbulent fountains in a confined stratified environment, *J. Fluid Mech.*, *389*, 27-54.

Brandes, J. A., and A. H. Devol (2002), A global marine-fixed nitrogen isotopic budget: Implications for Holocene nitrogen cycling, *Global Biogeochemical Cycles*, *16*(4), 14.

Brass, G. W., et al. (1982), Warm saline bottom water in the ancient ocean, *Nature*, *296*(5858), 620-623.

Breitbarth, E., et al. (2007), Physiological constraints on the global distribution of Trichodesmium - effect of temperature on diazotrophy, *Biogeosciences*, *4*(1), 53-61.

Brettar, I., and G. Rheinheimer (1991), Denitrification in the central Baltic - evidence for H2S-oxidation as motor of denitrification at the oxic-anoxic interface, *Marine Ecology-Progress Series*, *77*(2-3), 157-169.

Brink, K. H., et al. (1995), Group report: How do coastal upwelling systems operate as integrated physical, chemical, and biological systems and influence the geological record? The role of physical processes in defining the spatial structures of biological and chemical variables., in *Upwelling in the Ocean: Modern Processes and Ancient Records*, edited by C. P. Summerhayes, et al., pp. 103-124, J. Wiley & Sons, New York.

Brion, N., and G. Billen (1998), A reassessment of the H14CO3- incorporation method for measuring autotrophic nitrification and its use to estimate the biomass of nitrifying bacteria, *Rev. Sci. Eau*, *11*(2), 283-302.

Brocks, J. J., et al. (2005), Biomarker evidence for green and purple sulfur bacteria in a stratified Paleoproterozoic sea, *Nature*, *437*, 866-870.

Brocks, J. J., and P. Schaeffer (2008), Okenane, a biomarker for purple sulfur bacteria (Chromatiaceae), and other new carotenoid derivatives from the 1640 Ma Barney Creek Formation, *Geochimica Et Cosmochimica Acta*, *72*(5), 1396-1414.

Broecker, W., et al. (1999), How strong is the Harvardton-Bear constraint?, *Global Biogeochemical Cycles*, *13*(4), 817-820.

Broecker, W. S. (1971), A kinetic model for the chemical composition of sea water, *Quaternary Research (Orlando)*, *1*(2), 188-207.

Broecker, W. S., et al. (1978), Estimate of the upwelling rate in the equatorial atlantic based on the distribution of bomb radiocarbon, *Journal of Geophysical Research-Oceans and Atmospheres*, *83*(NC12), 6179-6186.

Broecker, W. S., and T. H. Peng (1986), Carbon cycle - 1985 glacial to interglacial changes in the operation of the global carbon cycle, *Radiocarbon*, *28*(2A), 309-327.

Broecker, W. S. (1991), The great ocean conveyor, *Oceanography*, *4*(2), 79-89.

Broecker, W. S., et al. (1998), How much deep water is formed in the Southern Ocean?, *Journal of Geophysical Research-Oceans*, *103*(C8), 15833-15843.

Bryan, K., and L. J. Lewis (1979), Water mass model of the world ocean, *Journal of Geophysical Research-Oceans and Atmospheres*, *84*(NC5), 2503-2517.

Burchuladze, A. A., et al. (1989), Anthropogenic C-14 variations in atmospheric CO2 and wines, *Radiocarbon*, *31*(3), 771-776.

Burlalova, Z. P., et al. (1997), Particulate organic matter of Black Sea euphotic zone: Seasonal and long-term variation of spatial distribution and composition, in *Sensitivity to Change: Black Sea, Baltic Sea and North Sea*, edited by E. Ozsoy and A. Mikaelyan, pp. 223-238, Kluwer Academic Publishing, Dordrecht.

Canfield, D. E., et al. (1996), A model for iron deposition to euxinic Black Sea sediments, *Am. J. Sci.*, *296*(7), 818-834.

Canfield, D. E., and A. Teske (1996), Late Proterozoic rise in atmospheric oxygen concentration inferred from phylogenetic and sulphur-isotope studies, *Nature*, *382*(6587), 127.

Canfield, D. E. (1998), A new model for Proterozoic ocean chemistry *Nature*, *396*, 450-453.

Canfield, D. E., and R. Raiswell (1999), The evolution of the sulfur cycle, *Am. J. Sci.*, *299*(7-9), 697-723.

Canfield, D. E., et al. (2000), The Archean sulfur cycle and the early history of atmospheric oxygen, *Science*, *288*(5466), 658-661.

Canfield, D. E. (2005), The early history of atmospheric oxygen: Homage to Robert A. Garrels, *Annu. Rev. Earth Planet. Sci.*, *33*, 1-36.

Canfield, D. E. (2006), Models of oxic respiration, denitrification and sulfate reduction in zones of coastal upwelling, *Geochimica Et Cosmochimica Acta*, *70*(23), 5753-5765.

Canfield, D. E., et al. (2007), Late-Neoproterozoic deep-ocean oxygenation and the rise of animal life, *Science*, *315*(5808), 92-95.

Carlson, C. A., and H. W. Ducklow (1995), Dissolved organic carbon in the upper ocean of the central equatorial Pacific Ocean, 1992: Daily and finescale vertical variations, *Deep-Sea Research Part II-Topical Studies in Oceanography*, *42*(2-3), 639-656.

Carr, M. E., et al. (2006), A comparison of global estimates of marine primary production from ocean color, *Deep-Sea Research Part Ii-Topical Studies in Oceanography*, *53*(5-7), 741-770.

Catling, D. C., and M. W. Claire (2005), How Earth's atmosphere evolved to an oxic state: A status report, *Earth Planet. Sci. Lett.*, *237*(1-2), 1-20.

Chavez, F. P., et al. (1989), The potential primary production of the Peruvian upwelling ecosystem, 1953-1984, in *The Peruvian Upwelling Ecosystem: Dynamics and Interactions*, edited by D. Pauly, et al., ICLARM, Manila.

Chavez, F. P., and J. R. Toggweiler (1995), Physical estimates of global new production: the upwelling contribution, in *Upwelling in the Ocean: Modern Processes*

and Ancient Records, edited by C. P. Summerhayes, et al., pp. 313-320, J. Wiley & Sons, New York.

Christensen, P. B., et al. (1989), Microzonation of denitrification activity in stream sediments as studied with a combined oxygen and nitrous oxide microsensor, *Applied and Environmental Microbiology*, *55*(5), 1234-1241.

Chu, P. C., et al. (2005), Seasonal variability of the Black Sea chlorophyll-a concentration, *Journal of Marine Systems*, *56*(3-4), 243-261.

Claussen, M., et al. (2002), Earth system models of intermediate complexity: closing the gap in the spectrum of climate system models, *Climate Dynamics*, *18*(7), 579-586.

Coban-Yildiz, Y., et al. (2006), Analytical pyrolysis of suspended particulate organic matter from the Black Sea water column, *Deep-Sea Research Part Ii-Topical Studies in Oceanography*, *53*(17-19), 1856-1874.

Cociasu, A., et al. (1996), Long-term ecological changes in Romanian coastal waters of the Black Sea, *Mar. Pollut. Bull.*, *32*(1), 32-38.

Codispoti, L. (2000a), "Hydrographic data, incl. temperature, salinity, nutrients from Niskin bottles." United States JGOFS Data Server. Woods Hole Oceanographic Institution, USA: U.S. JGOFS Data Management Office, iPub: 11 Oct 2000. Accessed: 4 April 2008. http://usjgofs.whoi.edu/jg/dir/jgofs/southern/.

Codispoti, L. (2000b), "Hydrographic data (temp, salinity and nutrients)." United States JGOFS Data Server. Woods Hole Oceanographic Institution, USA: U.S. JGOFS Data Management Office, iPub: 8 May 2000. Accessed: 4 April 2008. http://usjgofs.whoi.edu/jg/dir/jgofs/arabian/.

Codispoti, L. A., et al. (2001), The oceanic fixed nitrogen and nitrous oxide budgets: Moving targets as we enter the anthropocene?, *Scientia Marina*, *65*, 85-105.

Compton, J., et al. (2000), Variations in the global phosphorus cycle, in *Marine Authigenesis: From Global to Microbial*, edited by C. R. Glenn, et al., pp. 21-34, Society for Sedimentary Geology, Tulsa, Oklahoma.

Dalsgaard, T., et al. (2003), N-2 production by the anammox reaction in the anoxic water column of Golfo Dulce, Costa Rica, *Nature*, *422*(6932), 606-608.

Dalsgaard, T., et al. (2005), Anaerobic ammonium oxidation (anammox) in the marine environment, *Research in Microbiology*, *156*(4), 457-464.

Davis, J., and R. Benner (2007), Quantitative estimates of labile and semi-labile dissolved organic carbon in the western Arctic Ocean: A molecular approach, *Limnology and Oceanography*, *52*, 2434-2444.

del Giorgio, P. A., and C. M. Duarte (2002), Respiration in the open ocean, *Nature*, *420*(6914), 379-384.

Derry, L. A., et al. (1992), Sedimentary cycling and environmental change in the Late Proterozic: evidence from stable and radiogenic isotopes, *Geochimica et Cosmochimica Acta*, *56*, 1317-1329.

Deutsch, C., et al. (2001), Denitrification and N-2 fixation in the Pacific Ocean, *Global Biogeochemical Cycles*, *15*(2), 483-506.

Deutsch, C., et al. (2004), Isotopic constraints on glacial/interglacial changes in the oceanic nitrogen budget, *Global Biogeochemical Cycles*, *18*(4), 25.

Deutsch, C., et al. (2007), Spatial coupling of nitrogen inputs and losses in the ocean, *Nature*, *445*(7124), 163-167.

Doney, S. C., and W. J. Jenkins (1988), The effect of boundary conditions on tracer estimates of thermocline ventilation rates, *Journal of Marine Research*, *46*(4), 947-965.

Ducklow, H. (2002a), "Bacteria abundance, Thymidine and Leucine incorporation." United States JGOFS Data Server. Woods Hole Oceanographic Institution, USA: U.S. JGOFS Data Management Office, iPub: 27 Feb 2002. Accessed: 4 April 2008. http://usjgofs.whoi.edu/jg/dir/jgofs/arabian/.

Ducklow, H. (2002b), "Bacterial abundance, cell volume and activity." United States JGOFS Data Server. Woods Hole Oceanographic Institution, USA: U.S. JGOFS Data

Management Office, iPub: 27 Feb 2002. Accessed: 4 April 2008. http://usjgofs.whoi.edu/jg/dir/jgofs/southern/.

Ducklow, H. W., et al. (2007), Dissolved organic carbon and nitrogen in the Western Black Sea, *Marine Chemistry*, *105*(1-2), 140-150.

Dufour, P. H., and J. P. Torreton (1996), Bottom-up and top-down control of bacterioplankton from eutrophic to oligotrophic sites in the tropical northeastern Atlantic Ocean, *Deep-Sea Research Part I-Oceanographic Research Papers*, *43*(8), 1305-1320.

Dunne, J. P., et al. (2007), A synthesis of global particle export from the surface ocean and cycling through the ocean interior and on the seafloor, *Global Biogeochemical Cycles*, *21*(4), 16.

Eppley, R. W., and B. J. Peterson (1979), Particulate Organic-Matter Flux and Planktonic New Production in the Deep Ocean, *Nature*, *282*(5740), 677.

Eremeev, V. N., Ivanov, L. I., Samodurov, A. S., Duman, M. (1998) . (1998), The near-bottom boundary layer in the Black Sea: hydrological structure and modeling, *Physical Oceanography*, *9*, 79-101.

Etheridge, D. M., et al. (1996), Natural and anthropogenic changes in atmospheric CO2 over the last 1000 years from air in Antarctic ice and firn, *Journal of Geophysical Research-Atmospheres*, *101*(D2), 4115-4128.

Falkowski, P. G. (1997), Evolution of the nitrogen cycle and its influence on the biological sequestration of CO2 in the ocean, *Nature*, *387*, 272-275.

Farooq, A., and D. Smith (2001), "Bacteria abundance, Thymidine and Leucine incorporation." United States JGOFS Data Server. Woods Hole Oceanographic Institution, USA: U.S. JGOFS Data Management Office, iPub: 9 July 2001. Accessed: 4 April 2008. http://usjgofs.whoi.edu/jg/dir/jgofs/arabian/.

Fennel, K., et al. (2005), The co-evolution of the nitrogen, carbon and oxygen cycles in the Proterozoic ocean, *Am. J. Sci.*, *305*(6-8), 526-545.

Fike, D. A., et al. (2006), Oxidation of the Ediacaran Ocean, *Nature*, *444*(7120), 744-747.

Filippelli, G. M., and M. L. Delaney (1996), Phosphorus geochemistry of equatorial Pacific sediments, *Geochimica Et Cosmochimica Acta*, *60*(9), 1479-1495.

Filippov, D. M. (1965), The cold intermediate layer in the Black Sea, *Oceanology*, *5*, 47-52.

Fine, R. A., et al. (2001), Circulation and ventilation flux of the Pacific Ocean, *Journal of Geophysical Research-Oceans*, *106*(C10), 22159-22178.

Follmi, K. B. (1996), The phosphorus cycle, phosphogenesis and marine phosphate-rich deposits, *Earth-Science Reviews*, *40*(1-2), 55-124.

Forth, S. A. (2006), An efficient overloaded implementation of forward mode automatic differentiation in MATLAB, *ACM Transactions on Mathematical Software*, *32*(2), 195-222.

Forth, S. A., and M. M. Edvall (2007), *User Guide for MAD - a Matlab Automatic Differentiation Toolbox, TOMLAB /MAD, Version 1.4.*, Tomlab Optimization Inc., San Diego.

Froelich, P. N., et al. (1982), The marine phosphorus cycle, *Am. J. Sci.*, *282*(4), 474-511.

Froelich, P. N. (1988), Kinetic control of dissolved phosphate in natural rivers and estuaries: a primer on the phosphate buffer mechanism, *Limnology and Oceanography*, *33*(4), 649-668.

Galloway, J. N., et al. (2004), Nitrogen cycles: past, present, and future, *Biogeochemistry*, *70*(2), 153-226.

Ganachaud, A., and C. Wunsch (2000), Improved estimates of global ocean circulation, heat transport and mixing from hydrographic data, *Nature*, *408*(6811), 453.

Ganachaud, A., and C. Wunsch (2002), Oceanic nutrient and oxygen transports and bounds on export production during the World Ocean Circulation Experiment, *Global Biogeochemical Cycles*, *16*(4), 14.

Ganachaud, A. (2003), Large-scale mass transports, water mass formation, and diffusivities estimated from World Ocean Circulation Experiment (WOCE) hydrographic data, *Journal of Geophysical Research-Oceans*, *108*(C7), 24.

Garabato, A. C. N., et al. (2004a), Turbulent diapycnal mixing in the Nordic seas, *Journal of Geophysical Research-Oceans*, *109*(C12), 9.

Garabato, A. C. N., et al. (2004b), Widespread intense turbulent mixing in the Southern Ocean, *Science*, *303*(5655), 210-213.

Garcia, H. E., et al. (2006a), World Ocean Atlas 2005, Volume 3: Dissolved Oxygen, Apparent Oxygen Utilization, and Oxygen Saturation, edited by S. Levitus, NOAA Atlas NESDIS 63, U.S. Government Printing Office, Washington, D.C., 342 pp.

Garcia, H. E., et al. (2006b), World Ocean Atlas 2005, Volume 4: Nutrient (phosphate, nitrate, silicate). edited by S. Levitus, NOAA Atlas NESDIS 64, U.S. Government Printing Office, Washington, D.C., 396 pp.

Gent, P. R., and J. C. McWilliams (1990), Isopycnal mixing in ocean circulation models, *Journal of Physical Oceanography*, *20*(1), 150-155.

Glover, H. E. (1985), The relationship between inorganic nitrogen oxidation and organic carbon production in batch and chemostat cultures of marine nitrifying bacteria, *Archives of Microbiology*, *142*(1), 45-50.

Gnanadesikan, A., et al. (2004), Oceanic ventilation and biogeochemical cycling: Understanding the physical mechanisms that produce realistic distributions of tracers and productivity, *Global Biogeochemical Cycles*, *18*(4), 23.

Godfrey, J. S., and J. V. Mansbridge (2000), Ekman transports, tidal mixing, and the control of temperature structure in Australia's northwest waters, *Journal of Geophysical Research-Oceans*, *105*(C10), 24021-24044.

Gregg, M. C. (1987), Diapycnal mixing in the thermocline - a review, *Journal of Geophysical Research-Oceans*, *92*(C5), 5249-5286.

Gregg, M. C., and E. Yakushev (2005), Surface ventilation of the Black Sea's cold intermediate layer in the middle of the western gyre, *Geophys. Res. Lett.*, *32*(3), 4.

Gregoire, M., and J. Friedrich (2004), Nitrogen budget of the northwestern Black Sea shelf inferred from modeling studies and in situ benthic measurements, *Marine Ecology-Progress Series*, *270*, 15-39.

Grice, K., et al. (2005), Photic zone euxinia during the Permian-Triassic superanoxic event, *Science*, *307*(5710), 706-709.

Gruber, N., and J. L. Sarmiento (1997), Global patterns of marine nitrogen fixation and denitrification, *Global Biogeochemical Cycles*, *11*(2), 235-266.

Gruber, N. (2004), The dynamics of the marine nitrogen cycle and its influence on atmospheric CO2, in *The Ocean Carbon Cycle and Climate*, edited by M. Follows and T. Oguz, pp. 97-148, Kluwer Academic, Dordrecht.

Gruber, N., et al. (2006), Eddy-resolving simulation of plankton ecosystem dynamics in the California Current System, *Deep-Sea Research Part I-Oceanographic Research Papers*, *53*, 1483-1516.

Guerrero, M. A., and R. D. Jones (1996a), Photoinhibition of marine nitrifying bacteria .1. Wavelength-dependent response, *Marine Ecology-Progress Series*, *141*(1-3), 183-192.

Guerrero, M. A., and R. D. Jones (1996b), Photoinhibition of marine nitrifying bacteria .2. Dark recovery after monochromatic or polychromatic irradiation, *Marine Ecology-Progress Series*, *141*(1-3), 193-198.

Guisasola, A., et al. (2005), Respirometric estimation of the oxygen affinity constants for biological ammonium and nitrite oxidation, *Journal of Chemical Technology and Biotechnology*, *80*(4), 388-396.

Halverson, G. P., et al. (2005), Toward a Neoproterozoic composite carbon-isotope record, *Bulletin of the Geological Society of America*, *117*, 1181-1207.

Hamersley, M. R., et al. (2007), Anaerobic ammonium oxidation in the Peruvian oxygen minimum zone, *Limnology and Oceanography*, *52*(3), 923-933.

Handoh, I. C., and T. M. Lenton (2003), Periodic mid-Cretaceous oceanic anoxic events linked by oscillations of the phosphorus and oxygen biogeochemical cycles, *Global Biogeochemical Cycles*, *17*(4), 11.

Hansell, D., and C. Carlson (1998), "Dissolved Organic Carbon (DOC) from CTD casts." United States JGOFS Data Server. Woods Hole Oceanographic Institution, USA: U.S. JGOFS Data Management Office, iPub: 24 Arpil 1998. Accessed: 4 April 2008. http://usjgofs.whoi.edu/jg/dir/jgofs/southern/.

Hashimoto, L. K., et al. (1983), Transformations of fixed nitrogen and N2O in the Cariaco Trench, *Deep-Sea Research Part A-Oceanographic Research Papers*, *30*(6), 575-590.

Hay, B. J., et al. (1990), Interannual variability in particle flux in the southwestern Black Sea, *Deep-Sea Research Part A-Oceanographic Research Papers*, *37*(6), 911-928.

Hayes, J. M., et al. (1999), The abundance of C-13 in marine organic matter and isotopic fractionation in the global biogeochemical cycle of carbon during the past 800 Ma, *Chemical Geology*, *161*(1-3), 103.

Hazeleger, W., and S. Drijfhout (2006), Subtropical cells and meridional overturning circulation pathways in the tropical Atlantic, *Journal of Geophysical Research-Oceans*, *111*(C3), 13.

Hedges, J. I., et al. (1999), Sedimentary organic matter preservation: A test for selective degradation under oxic conditions, *Am. J. Sci.*, *299*(7-9), 529-555.

Heinze, C., et al. (2003), Sensitivity of the marine biospheric Si cycle for biogeochemical parameter variations, *Global Biogeochemical Cycles*, *17*(3), 23.

Hiscock, W. T., and F. J. Millero (2006), Alkalinity of the anoxic waters in the Western Black Sea, *Deep-Sea Research Part Ii-Topical Studies in Oceanography*, *53*(17-19), 1787-1801.

Holland, H. D. (2006), The oxygenation of the atmosphere and oceans, *Philos. Trans. R. Soc. B-Biol. Sci.*, *361*(1470), 903-915.

Hooper, A. B., and K. R. Terry (1974), Photoinactivation of ammonia oxidation in nitrosomonas, *Journal of Bacteriology*, *119*(3), 899-906.

Horrigan, S. G., et al. (1981), Light inhibition of nitrification in sea surface films, *Journal of Marine Research*, *39*(3), 557-565.

Horrigan, S. G., and A. L. Springer (1990), Oceanic and estuarine ammonium oxidation - effects of light, *Limnology and Oceanography*, *35*(2), 479-482.

Hotinski, R. M., et al. (2000), Opening Pandora's box: The impact of open system modeling on interpretations of anoxia, *Paleoceanography*, *15*(3), 267-279.

Hundsdorfer, W., and I. G. Verwer (2007), *Numerical Solutions of Time-Dependent Advection-Diffusion-Reaction Equations*, 500 pp., Springer, Berlin.

Hurtgen, M. T., et al. (2002), The sulfur isotopic composition of Neoproterozoic seawater sulfate: implications for a snowball Earth?, *Earth Planet. Sci. Lett.*, *203*, 413-429.

Hurtgen, M. T., et al. (2005), Neoproterozoic sulfur isotopes, the evolution of microbial sulfur species, and the burial efficiency of sulfide as sedimentary pyrite, *Geology*, *33*, 41-44.

Ingall, E., and R. Jahnke (1997), Influence of water-column anoxia on the elemental fractionation of carbon and phosphorus during sediment diagenesis, *Marine Geology*, *139*(1-4), 219-229.

Ingall, E. D., and P. Vancappellen (1990), Relation between sedimentation rate and burial of organic phosphorus and organic carbon in marine sediments, *Geochimica Et Cosmochimica Acta*, *54*(2), 373-386.

Ingalls, A. E., et al. (2006), Quantifying archaeal community autotrophy in the mesopelagic ocean using natural radiocarbon, *Proceedings of the National Academy of Sciences of the United States of America*, *103*(17), 6442-6447.

Isley, A. E., and D. H. Abbott (1999), Plume-related mafic volcanism and the deposition of banded iron formation, *J. Geophys. Res.-Solid Earth*, *104*(B7), 15461-15477.

Ivanov, L. I., et al. (2000), Ventilation of the Black Sea pycnocline on seasonal and interannual time scales, *Mediterranean Marine Science*, *1/2*, 61-74.

Ivanov, L. I., et al. (2001), Convection in the Black Sea during cold winters, *Journal of Marine Systems*, *31*(1-3), 65-76.

Ivanov, L. I., and A. S. Samodurov (2001), The role of lateral fluxes in ventilation of the Black Sea, *Journal of Marine Systems*, *31*(1-3), 159.

Jahnke, R. A. (1996), The global ocean flux of particulate organic carbon: Areal distribution and magnitude, *Global Biogeochemical Cycles*, *10*(1), 71-88.

Jaoshvili, S. (2002), The rivers of the Black Sea, European Environment Agency, Copenhagen <http://reports.eea.europa.eu/technical_report_2002_71/en>.

Jetten, M. S. M., et al. (2001), Microbiology and application of the anaerobic ammonium oxidation ('anammox') process, *Current opinion in biotechnology*, *12*(3), 283.

Jickells, T. D., et al. (2005), Global iron connections between desert dust, ocean biogeochemistry, and climate, *Science*, *308*(5718), 67-71.

Johnson, G. C., et al. (2001), Equatorial Pacific ocean horizontal velocity, divergence, and upwelling, *Journal of Physical Oceanography*, *31*(3), 839-849.

Jorgensen, B. B., et al. (1991), Sulfide oxidation in the anoxic Black Sea chemocline, *Deep-Sea Research Part A-Oceanographic Research Papers*, *38*, S1083-S1103.

Kahana, R., et al. (2004), Global ocean circulation modes derived from a multiple box model, *Journal of Physical Oceanography*, *34*(8), 1811-1823.

Kamp, A., et al. (2006), Anaerobic sulfide oxidation with nitrate by a freshwater Beggiatoa enrichment culture, *Applied and Environmental Microbiology*, *72*(7), 4755-4760.

Kara, A. B., et al. (2005), Black sea mixed layer sensitivity to various wind and thermal forcing products on climatological time scales, *J. Clim.*, *18*(24), 5266-5293.

Karl, D. (2008), "HOT Bottle Data." HOT-DOGS Data Server. U. Hawaii. iPub: 18 Nov 2007. Accessed: 4 Apr 2008. ftp://ftp.bios.edu/BATS/bottle/bats_bottle.txt.

Karl, D. M., and G. A. Knauer (1991), Microbial production and particle flux in the upper 350 m of the Black Sea, *Deep-Sea Research Part A-Oceanographic Research Papers*, *38*, S921-S942.

Karner, M. B., et al. (2001), Archaeal dominance in the mesopelagic zone of the Pacific Ocean, *Nature*, *409*(6819), 507-510.

Kartal, B., et al. (2007), Anammox bacteria disguised as denitrifiers: nitrate reduction to dinitrogen gas via nitrite and ammonium, *Environ. Microbiol.*, *9*(3), 635-642.

Kasting, J. F. (1987), Theoretical constraints on oxygen and carbon dioxide concentrations in the Precambrian atmosphere, *Precambrian Research*, *34*.

Keeling, C. D., and T. P. Whorf (2005), Atmospheric CO2 records from sites in the SIO air sampling network., in *Trends: A Compendium of Data on Global Change.* , edited, Carbon Dioxide Information Analysis Center. Oak Ridge National Laboratory, U.S. Department of Energy, Oak Ridge, Tenn., U.S.A.

Keeling, R. F., et al. (1998), Seasonal variations in the atmospheric O-2/N-2 ratio in relation to the kinetics of air-sea gas exchange, *Global Biogeochemical Cycles*, *12*(1), 141-163.

Keir, R. S. (1988), On the late Pleistocene ocean geochemistry and circulation, *Paleoceanography*, *3*(4), 413-445.

Kessler, W. S. (2002), Mean three-dimensional circulation in the northeast tropical Pacific, *Journal of Physical Oceanography*, *32*(9), 2457-2471.

Kessler, W. S. (2006), The circulation of the eastern tropical Pacific: A review, *Prog. Oceanogr.*, *69*(2-4), 181-217.

Kideys, A. E. (2002), Fall and rise of the Black Sea ecosystem, *Science*, *297*(5586), 1482-1484.

Knap, A., et al. (2008), "BATS Bottle Data." BATS FTP Data Server. Bermuda Institute of Ocean Sciences. iPub: 16 Mar 2008. Accessed: 4 Apr 2008. ftp://ftp.bios.edu/BATS/bottle/bats_bottle.txt.

Knox, F., and M. B. McElroy (1984), CHANGES IN ATMOSPHERIC CO2 - INFLUENCE OF THE MARINE BIOTA AT HIGH-LATITUDE, *Journal of Geophysical Research-Atmospheres*, *89*(ND3), 4629-4637.

Koch, G., et al. (2000), Mathematical modeling of autotrophic denitrification in a nitrifying biofilm of a rotating biological contactor, *Water Science and Technology*, *41*(4-5), 191-198.

Konneke, M., et al. (2005), Isolation of an autotrophic ammonia-oxidizing marine archaeon, *Nature*, *437*(7058), 543-546.

Konovalov, S., et al. (2004), Parameterization of iron and manganese cycling in the Black Sea suboxic and anoxic environment, *Deep-Sea Research Part I-Oceanographic Research Papers*, *51*(12), 2027-2045.

Konovalov, S. K., et al. (2000), Oxygen nitrogen and sulphide fluxes in the Black Sea, *Mediterranean Marine Science*, *1/2*, 41-59.

Konovalov, S. K., and J. W. Murray (2001), Variations in the chemistry of the Black Sea on a time scale of decades (1960-1995), *Journal of Marine Systems*, *31*(1-3), 217.

Konovalov, S. K., et al. (2005), Basic processes of Black Sea biogeochemistry, *Oceanography*, *18*(2), 24-35.

Konovalov, S. K., et al. (2006), Processes controlling the redox budget for the oxic/anoxic water column of the Black Sea, *Deep-Sea Research Part Ii-Topical Studies in Oceanography*, *53*(17-19), 1817-1841.

Konovalov, S. K., et al. (2007), Porewater redox species and processes in the Black Sea sediments, *Chemical Geology*, *245*(3-4), 254-274.

Kornaros, M., and G. Lyberatos (1998), Kinetic modeling of Pseudomonas denitrificans growth and denitrification under aerobic, anoxic, and transient operating conditions, *Water Research*, *32*, 1912-1922.

Krishnakumar, B., and V. B. Manilal (1999), Bacterial oxidation of sulphide under denitrifying conditions, *Biotechnol. Lett.*, *21*(5), 437-440.

Kunze, E., et al. (2006), Global abyssal mixing inferred from lowered ADCP shear and CTD strain profiles, *Journal of Physical Oceanography*, *36*(8), 1553-1576.

Kuypers, M. M. M., et al. (2003), Anaerobic ammonium oxidation by anammox bacteria in the Black Sea, *Nature*, *422*(6932), 608.

Kuypers, M. M. M., et al. (2005), Massive nitrogen loss from the Benguela upwelling system through anaerobic ammonium oxidation, *Proceedings of the National Academy of Sciences of the United States of America*, *102*(18), 6478-6483.

Landing, W. M., and B. L. Lewis (1991), Thermodynamic modeling of trace metal speciation in the Black Sea, in *Black Sea Oceanography*, edited by E. Izdar and J. W. Murray, pp. 125–160, Kluwer Academic Publishers, Dordrecht, The Netherlands.

Lane, E., et al. (2006), A dynamic-flow carbon-cycle box model and high-latitude sensitivity, *Tellus Series B-Chemical and Physical Meteorology*, *58*(4), 257-278.

Latif, M. A., et al. (1991), Observations of the Mediterranean inflow into the Black Sea, *Deep-Sea Research Part A-Oceanographic Research Papers*, *38*, S711-S723.

Lavik, G., et al. (2006), Anaerobic oxidation of hydrogen sulfide coupled to nitrate reduction in Namibian Coastal waters., *Geophysical Research Abstracts*, *8*, 10937.

Laws, E. A., et al. (2000), Temperature effects on export production in the open ocean, *Global Biogeochemical Cycles*, *14*(4), 1231-1246.

Ledwell, J. R., et al. (1998), Mixing of a tracer in the pycnocline, *Journal of Geophysical Research-Oceans*, *103*(C10), 21499-21529.

Lee, B. S., et al. (2002), Anthropogenic chlorofluorocarbons in the Black Sea and the Sea of Marmara, *Deep-Sea Research Part I-Oceanographic Research Papers*, *49*(5), 895-913.

Lein, A. Y., and M. V. Ivanov (1991), On the sulfur and carbon balances in the Black Sea, in *Black Sea Oceanography*, edited by E. Izdar and J. W. Murray, pp. 307-318, Kluwer Academic Publishers, Dordrecht, The Netherlands.

Lenton, T. M., and A. J. Watson (2000a), Redfield revisited 1. Regulation of nitrate, phosphate, and oxygen in the ocean, *Global Biogeochemical Cycles*, *14*(1), 225-248.

Lenton, T. M., and A. J. Watson (2000b), Redfield revisited 1. Regulation of nitrate, phosphate and oxygen in the ocean, *Global Biogeochemical Cycles*, *14*(1), 225-248.

Lenton, T. M., and C. A. Klausmeier (2007), Biotic stoichiometric controls on the deep ocean N : P ratio, *Biogeosciences*, *4*(3), 353-367.

Lenton, T. M., et al. (2007), Effects of atmospheric dynamics and ocean resolution on bi-stability of the thermohaline circulation examined using the Grid ENabled Integrated Earth system modelling (GENIE) framework, *Climate Dynamics*, *29*, 591-613.

Levin, I., et al. (1994), δ14CO2 record from Vermunt., in *Trends: A Compendium of Data on Global Change.* , edited, Carbon Dioxide Information Analysis Center. Oak Ridge National Laboratory, U.S. Department of Energy, Oak Ridge, Tenn., U.S.A.

Lewis, B. L., and W. M. Landing (1991), The biogeochemistry of manganese and iron in the Black Sea, *Deep-Sea Research Part A-Oceanographic Research Papers*, *38*, S773-S803.

Lipschultz, F. (2001), A time-series assessment of the nitrogen cycle at BATS, *Deep-Sea Research Part Ii-Topical Studies in Oceanography*, *48*(8-9), 1897-1924.

Liss, P. S., and L. Merlivat (1986), Air-sea gas exchange rates: Introduction and synthesis, in *The Role of Air-Sea Exchange in Geochemical Cycling*, edited by P. Buat-Menard, pp. 113-127, D. Reidel, Dordrecht, Netherlands.

Locarnini, R. A., et al. (2006), World Ocean Atlas 2005, Volume 1: Temperature, edited by S. Levitus, NOAA Atlas NESDIS 61, U.S. Government Printing Office, Washington, D.C., 182 pp.

Logan, G. A., et al. (1995), Terminal Proterozoic reorganization of biogeochemical cycles, *Nature*, *376*(6535), 53-56.

Lomas, M. W., and F. Lipschultz (2006), Forming the primary nitrite maximum: Nitrifiers or phytoplankton?, *Limnology and Oceanography*, *51*(5), 2453-2467.

Lumpkin, R., and K. Speer (2003), Large-scale vertical and horizontal circulation in the North Atlantic Ocean, *Journal of Physical Oceanography*, *33*(9), 1902-1920.

Luo, S. D., and T. L. Ku (2003), Constraints on deep-water formation from the oceanic distributions of Be-10, *Journal of Geophysical Research-Oceans*, *108*(C5), 7.

Lutjeharms, J. R. E., et al. (1991), Observations of extreme upwelling filaments in the southeast Atlantic Ocean, *Science*, *253*(5021), 774-776.

Lyons, T. W., and R. A. Berner (1992), Carbon sulfur iron systematics of the uppermost deep water sediments of the Black Sea, *Chemical Geology*, *99*(1-3), 1-27.

Manning, M. R., and W. H. Melhuish (1994), Atmospheric δ14C record from Wellington., in *Trends: A Compendium of Data on Global Change.* , edited, Carbon Dioxide Information Analysis Center. Oak Ridge National Laboratory, U.S. Department of Energy, Oak Ridge, Tenn., U.S.A.

Martin, J. H., et al. (1987), VERTEX - carbon cycling in the northeast Pacific, *Deep-Sea Research Part A-Oceanographic Research Papers*, *34*(2), 267-285.

McCarthy, J. J., et al. (2007), Nitrogen cycling in the offshore waters of the Black Sea, *Estuar. Coast. Shelf Sci.*, *74*(3), 493-514.

McPhaden, M. J., and D. X. Zhang (2002), Slowdown of the meridional overturning circulation in the upper Pacific Ocean, *Nature*, *415*(6872), 603-608.

Mee, L. D. (1992), The Black Sea in crisis - a need for concerted international action, *Ambio*, *21*(4), 278-286.

Meijers, A. J., et al. (2007), On the total, mean, and eddy heat and freshwater transports in the southern hemisphere of a 1/8 degrees 1/8 degrees global ocean model, *Journal of Physical Oceanography*, *37*(2), 277-295.

Michel, E., et al. (1995), Could deep sub-antarctic convection feed the world deep basins during the last glacial maximum, *Paleoceanography*, *10*(5), 927-941.

Middelburg, J. J., et al. (1996), Denitrification in marine sediments: A model study, *Global Biogeochemical Cycles*, *10*(4), 661-673.

Millero, F. J. (1991), The oxidation of H2S in Black Sea waters, *Deep-Sea Research Part A-Oceanographic Research Papers*, *38*, S1139-S1150.

Millero, F. J. (1995), Thermodynamics of the carbon dioxide system in the oceans, *Geochimica Et Cosmochimica Acta*, *59*(4), 661-677.

Moore, J. K., et al. (2004), Upper ocean ecosystem dynamics and iron cycling in a global three-dimensional model, *Global Biogeochemical Cycles*, *18*(4), 21.

Moore, J. K., and S. C. Doney (2007a), Iron availability limits the ocean nitrogen inventory stabilizing feedbacks between marine denitrification and nitrogen fixation, *Global Biogeochemical Cycles*, *21*.

Moore, J. K., and S. C. Doney (2007b), Iron availability limits the ocean nitrogen inventory stabilizing feedbacks between marine denitrification and nitrogen fixation, *Global Biogeochemical Cycles*, *21*(2), 12.

Morel, F. M. M., and N. M. Price (2003), The biogeochemical cycles of trace metals in the oceans, *Science*, *300*(5621), 944-947.

Morse, J. W., and R. A. Berner (1995), What determines sedimentary C-S ratios, *Geochimica Et Cosmochimica Acta*, *59*(6), 1073-1077.

Mulder, A., et al. (1995), Anaerobic ammonium oxidation discovered in a denitrifying fluidized-bed reactor, *Fems Microbiology Ecology*, *16*(3), 177-183.

Muller-Karger, F. E., et al. (2005), The importance of continental margins in the global carbon cycle, *Geophys. Res. Lett.*, *32*(1), 4.

Munk, W., and C. Wunsch (1998), Abyssal recipes II: energetics of tidal and wind mixing, *Deep-Sea Research Part I-Oceanographic Research Papers*, *45*(12), 1977-2010.

Munk, W. H. (1966), Abyssal recipes, *Deep-Sea Research*, *13*, 701-730.

Murray, J. W., and E. Izdar (1989), The 1988 Black Sea oceanographic expedition: Overview and new discoveries, *Oceanography*, *2*, 15-21.

Murray, J. W., et al. (1991), Hydrographic properties and ventilation of the Black Sea, *Deep-Sea Research Part A-Oceanographic Research Papers*, *38*, S663-S689.

Murray, J. W., et al. (1995), Oxidation-reduction environments: The suboxic zone in the Black Sea, in *Aquatic Chemistry: Interfacial and Interspecies Processes*, edited by C. P. Huang, et al., pp. 157-176, American Chemical Society, Washington, DC.

Murray, J. W. (2006), Introduction - Recent US research cruises to the Black Sea, *Deep-Sea Research Part Ii-Topical Studies in Oceanography*, *53*(17-19), 1737-1739.

Nagata, T., et al. (2000), Bacterioplankton distribution and production in deep Pacific waters: Large-scale geographic variations and possible coupling with sinking particle fluxes, *Limnology and Oceanography*, *45*(2), 426.

Oguz, T., et al. (1991), On the dynamics of the southern Black Sea, in *Black Sea Oceanography*, edited by E. Izdar and J. W. Murray, pp. 43-63, Kluwer Academic Publishers, Boston.

Oguz, T., et al. (2001), Modeling redox cycling across the suboxic-anoxic interface zone in the Black Sea, *Deep-Sea Research Part I-Oceanographic Research Papers*, *48*(3), 761-787.

Oguz, T., et al. (2003), Climatic warming and accompanying changes in the ecological regime of the Black Sea during 1990s, *Global Biogeochemical Cycles*, *17*(3), 11.

Oguz, T., and D. Ediger (2006), Comparision of in situ and satellite-derived chlorophyll pigment concentrations, and impact of phytoplankton bloom on the suboxic layer structure in the western Black Sea during May-June 2001, *Deep-Sea Research Part Ii-Topical Studies in Oceanography*, *53*(17-19), 1923-1933.

Okubo, A. (1971), Oceanic diffusion diagrams, *Deep-Sea Research*, *18*(8), 789-&.

Olson, R. J. (1981a), 15N tracer studies of the primary nitrite maximum, *Journal of Marine Research*, *39*(2), 203-226.

Olson, R. J. (1981b), Differential photoinhibition of marine nitrifying bacteria - A possible mechanism for the formation of the primary nitrite maximum, *Journal of Marine Research*, *39*(2), 227-238.

Orsi, A. H., et al. (2001), Cooling and ventilating the abyssal ocean, *Geophys. Res. Lett.*, *28*(15), 2923-2926.

Orsi, A. H., et al. (2002), On the total input of Antarctic waters to the deep ocean: A preliminary estimate from chlorofluorocarbon measurements, *Journal of Geophysical Research-Oceans*, *107*(C8), 17.

Osborn, T., and C. Cox (1972), Oceanic fine structure, *Geophysical and Astrophysical Fluid Dynamics*, *3*, 321-345.

Östlund, G. H. (1974), Expedition "Odysseus 65": radiocarbon age of Black Sea deep water, in *The Black Sea-Geology, Chemistry, and Biology*, edited by E. T. Degens and D. A. Ross, pp. 127-132, AAPG, Tulsa, OK.

Otte, S., et al. (1999), Nitrogen, carbon, and sulfur metabolism in natural Thioploca samples, *Applied and Environmental Microbiology*, *65*(7), 3148-3157.

Ovchinnikov, I. M., and Y. I. Popov (1987), Evolution of the cold intermediate layer in the Black Sea, *Oceanology*, *27*, 555-560.

Ozsoy, E., et al. (1993), The evolution of Mediterranean water in the Black Sea - Interior mixing and material transport by double-diffusive intrusions, *Prog. Oceanogr.*, *31*(3), 275-320.

Ozsoy, E., and U. Unluata (1997), Oceanography of the Black Sea: a review of some recent results, *Earth-Science Reviews*, *42*(4), 231-272.

Pancost, R. D., et al. (2002), Molecular evidence for basin-scale photic zone euxinia in the Permian Zechstein Sea, *Chemical Geology*, *188*(3-4), 217-227.

Pancost, R. D., et al. (2004), Further evidence for the development of photic-zone euxinic conditions during Mesozoic oceanic anoxic events, *Journal of the Geological Society*, *161*, 353-364.

Papineau, D., et al. (2005), Nitrogen isotopic composition of ammoniated phyllosilicates: case studies from Precambrian metamorphosed sedimentary rocks, *Chemical Geology*, *216*(1-2), 37-58.

Parker, R. A. (1993), Dynamic models for ammonium inhibition of nitrate uptake by phytoplankton, *Ecological Modelling*, *66*(1-2), 113-120.

Paytan, A., and K. McLaughlin (2007), The oceanic phosphorus cycle, *Chem. Rev.*, *107*(2), 563-576.

Pelios, A., and R. W. Klopfens (1972), Minimal error constant numerical differentiation (ND) formulas, *Mathematics of Computation*, *26*(118), 467-&.

Peltzer, E., and D. Hansell (2001), "Total organic carbon profile data." United States JGOFS Data Server. Woods Hole Oceanographic Institution, USA: U.S. JGOFS Data Management Office, iPub: 8 May 2001. Accessed: 4 April 2008. http://usjgofs.whoi.edu/jg/dir/jgofs/arabian/.

Peltzer, E. (2002), "Total organic carbon profile data." United States JGOFS Data Server. Woods Hole Oceanographic Institution, USA: U.S. JGOFS Data Management

Office, iPub: 3 Sep 2002. Accessed: 4 April 2008. http://usjgofs.whoi.edu/jg/dir/jgofs/southern/.

Petoukhov, V., et al. (2005), EMIC Intercomparison Project (EMIP-CO2): comparative analysis of EMIC simulations of climate, and of equilibrium and transient responses to atmospheric CO2 doubling, *Climate Dynamics*, *25*(4), 363-385.

Pollard, R., et al. (2006), Quantifying nutrient supply to the Southern Ocean, *Journal of Geophysical Research-Oceans*, *111*(C5), 9.

Polzin, K. L., et al. (1997), Spatial variability of turbulent mixing in the abyssal ocean, *Science*, *276*(5309), 93-96.

Popova, E. E., et al. (2000), Biological pump and vertical mixing in the Southern Ocean: Their impact on atmospheric CO2, *Global Biogeochemical Cycles*, *14*(1), 477-498.

Prosser, J. I. (1989), Autotrophic nitrification in bacteria, *Advances in Microbial Physiology*, *30*, 125-181.

Raimbault, P., et al. (1999), Carbon and nitrogen uptake and export in the equatorial Pacific at 150 degrees W: Evidence of an efficient regenerated production cycle, *Journal of Geophysical Research-Oceans*, *104*(C2), 3341-3356.

Redfield, A. C. (1958), The biological control of chemical factors in the environment, *American Scientist*, *46*(3), 205.

Richards, F. A. (1965), Anoxic basins and fjords, in *Chemical Oceanography, vol. 1*, edited by J. P. Riley and G. Skirrow, pp. 611–645, Academic Press, London.

Ridgwell, A., et al. (2007), Marine geochemical data assimilation in an efficient Earth System Model of global biogeochemical cycling, *Biogeosciences*, *4*(1), 87-104.

Risien, C. M., and D. B. Chelton (2008), A global climatology of surface wind and wind stress fields from 8 years of QuikSCAT scatterometer data, *Journal of Physical Oceanography*, *submitted*.

Rothman, D. H., et al. (2003), Dynamics of the Neoproterozoic carbon cycle, *Proceedings of the National Academy of Sciences of the United States of America*, *100*(14), 8124-8129.

Rouxel, O. J., et al. (2005), Iron isotope constraints on the Archean and Paleoproterozoic ocean redox state, *Science*, *307*(5712), 1088-1091.

Rubin, S. I., and R. M. Key (2002), Separating natural and bomb-produced radiocarbon in the ocean: The potential alkalinity method, *Global Biogeochemical Cycles*, *16*(4).

Runnegar, B. (1982), Oxygen requirements, biology and phylogenetic significance of the Late Precambrian worm Dickinsonia, and the evolution of the burrowing habit, *Alcheringa*, *3-4*, 223-230.

Ruttenberg, K. C. (1993), Reassessment of the oceanic redidence time of phosphorus, *Chemical Geology*, *107*(3-4), 405-409.

Sabine, C. L., et al. (2005), Global Ocean Data Analysis Project: Results and Data. ORNL/CDIAC-145, NDP-083, 110 pp, Carbon Dioxide Information Analysis Center, Oak Ridge National Laboratory, U.S. Department of Energy, Oak Ridge, Tennessee.

Samodurov, A. S., and L. I. Ivanov (1998), Processes of ventilation of the Black Sea related to water exchange through the Bosporus, in *Ecosystem Modeling as a Management Tool for the Black Sea. NATO ASI Series, Vol. 47, No. 2.*, edited by L. I. Ivanov and T. Oguz, pp. 221–236, Kluwer, Dordrecht.

Sancak, S., et al. (2005), Evaluation of SeaWiFS chlorophyll-a in the Black and Mediterranean seas, *Int. J. Remote Sens.*, *26*(10), 2045-2060.

Sarmiento, J. L. (1983a), A tritium box model of the North-Atlantic thermocline, *Journal of Physical Oceanography*, *13*(7), 1269-1274.

Sarmiento, J. L. (1983b), A tritium box model of the North Atlantic thermocline, *Journal of Physical Oceanography*, *13*(7), 1269-1274.

Sarmiento, J. L., and J. R. Toggweiler (1984a), A new model for the role of the oceans in determining atmospheric Pco2, *Nature*, *308*(5960), 621.

Sarmiento, J. L., and J. R. Toggweiler (1984b), A new model for the role of the oceans in determining atmospheric PCO2, *Nature*, *308*(5960), 621-624.

Sarmiento, J. L., et al. (1988a), Causes of anoxia in the World Ocean, *Global Biogeochemical Cycles*, *2*, 115-128.

Sarmiento, J. L., et al. (1988b), Mediterranean nutrient balance and episodes of anoxia, *Global Biogeochemical Cycles*, *2*(4), 427-444.

Sarmiento, J. L., and J. C. Orr (1991), 3-dimensional simulations of the impact of Southern Ocean nutrient depletion on atmospheric CO2 and ocean chemistry, *Limnology and Oceanography*, *36*(8), 1928-1950.

Sarmiento, J. L., and N. Gruber (2006), *Ocean Biogeochemical Dynamics*, Princeton University Press, Princeton, NJ.

Schlitzer, R. (2004), Export production in the equatorial and North Pacific derived from dissolved oxygen, nutrient and carbon data, *J. Oceanogr.*, *60*(1), 53-62.

Schlitzer, R. (2007), Assimilation of radiocarbon and chlorofluorocarbon data to constrain deep and bottom water transports in the world ocean, *Journal of Physical Oceanography*, *37*(2), 259-276.

Schmitz, W. J., and M. S. McCartney (1993), On the North Atlantic circulation, *Reviews of Geophysics*, *31*(1), 29-49.

Schott, F. A., et al. (2002), The shallow overturning circulation of the Indian Ocean, *Prog. Oceanogr.*, *53*(1), 57-103.

Schreiber, H., et al. (2005), Nutrient emissions from diffuse and point sources into the River Danube and its main tributaries for the period of 1998-2000 - results and problems, *Water Science and Technology*, *51*(3-4), 283-290.

Schulz, H. N., et al. (1999), Dense populations of a giant sulfur bacterium in Namibian shelf sediments, *Science*, *284*(5413), 493-495.

Scott, C., et al. (2008), Tracing the stepwise oxygenation of the Proterozoic ocean, *Nature*, *452*(7186), 456-U455.

Shaffer, G. (1986), Phosphate pumps and shuttles in the Black Sea, *Nature*, *321*(6069), 515-517.

Shaffer, G. (1989), A model of biogeochemical cycling of phosphorus, nitrogen, oxygen, and sulfur in the ocean: one step toward a global climate model, *Journal of Geophysical Research-Oceans*, *94*(C2), 1979-2004.

Shaffer, G., and J. L. Sarmiento (1995), Biogeochemical cycling in the global ocean.1. A new, analytical model with continuous vertical resolution and high latitude dynamics, *Journal of Geophysical Research-Oceans*, *100*(C2), 2659-2672.

Shampine, L. F. (1994), *Numerical Solution of Ordinary Differential Equations*, 632 pp., Chapman & Hall, New York.

Shampine, L. F., and M. W. Reichelt (1997), The MATLAB ODE suite, *SIAM Journal on Scientific Computing*, *18*(1), 1.

Shampine, L. F. (2005), Error estimation and control for ODEs, *J. Sci. Comput.*, *25*(1), 3-16.

Shampine, L. F., et al. (2005a), Using AD to solve BVPs in MATLAB, *ACM Transactions on Mathematical Software*, *31*(1), 79.

Shampine, L. F., et al. (2005b), Non-negative solutions of ODEs, *Appl. Math. Comput.*, *170*(1), 556-569.

Shen, Y., et al. (2003), Evidence for low sulphate and anoxia in a mid-Proterozoic marine basin, *Nature*, *423*, 632-635.

Shields, G. A., et al. (1999), Sulphur isotope compositions of sedimentary phosphorites from the basal Cambrian of China: implications for Neoproterozoic-Cambrian biogeochemical cycling, *Journal of the Geological Society*, *156*, 943-955.

Shields, G. A., and J. Veizer (2002), Precambrian marine carbonate isotope database: Version 1.1, *Geochem. Geophys. Geosyst.*, *6*(3), 1-12.

Siani, G., et al. (2000), Radiocarbon reservoir ages in the Mediterranean Sea and Black Sea, *Radiocarbon*, *42*(2), 271-280.

Siegenthaler, U., and T. Wenk (1984a), Rapid atmospheric CO2 variations and ocean circulation, *Nature*, *308*(5960), 624.

Siegenthaler, U., and T. Wenk (1984b), Rapid atmospheric CO2 variations and ocean circulation, *Nature*, *308*(5960), 624-626.

Siegenthaler, U., and F. Joos (1992), Use of a simple model for studying oceanic tracer distributions and the global carbon cycle, *Tellus Series B-Chemical and Physical Meteorology*, *44*(3), 186-207.

Simon, M., and F. Azam (1989), Protein content and protein synthesis rates of planktonic marine bacteria, *Marine Ecology-Progress Series*, *51*(3), 201-213.

Skogen, M. D. (2004), A direct estimate of the Namibian upwelling flux, in *Ecological, economical and social aspects of Namibian fisheries*, edited by U. R. SUMAILA, et al., pp. 11-27, Eburon Publishers, Delft.

Slomp, C. P., and P. Van Cappellen (2007), The global marine phosphorus cycle: sensitivity to oceanic circulation, *Biogeosciences*, *4*(2), 155-171.

Sloyan, B. M., and S. R. Rintoul (2001), Circulation, renewal, and modification of Antarctic mode and intermediate water, *Journal of Physical Oceanography*, *31*(4), 1005-1030.

Sloyan, B. M. (2005), Spatial variability of mixing in the Southern Ocean, *Geophys. Res. Lett.*, *32*(18), 5.

Smethie, W. M., and R. A. Fine (2001), Rates of North Atlantic Deep Water formation calculated from chlorofluorocarbon inventories, *Deep-Sea Research Part I-Oceanographic Research Papers*, *48*(1), 189-215.

Soetaert, K., et al. (1996), A model of early diagenetic processes from the shelf to abyssal depths, *Geochimica et Cosmochimica Acta*, *60*(6), 1019.

Sorokin, Y. I. (2002), *The Black Sea: ecology and oceanography*, Backhuys, Leiden, Netherlands.

Spencer, D. W., and P. G. Brewer (1971), Vertical advection diffusion and redox potentials as controls on distribution of manganese and other trace metals dissolved in waters of Black Sea, *Journal of Geophysical Research*, *76*(24), 5877-&.

Stanev, E. V., et al. (2003), Control of Black Sea intermediate water mass formation by dynamics and topography: Comparison of numerical simulations, surveys and satellite data, *Journal of Marine Research*, *61*(1), 59-99.

Staneva, J., and E. Stanev (1997), Cold Intermediate Water formation in the Black Sea: Analysis on numerical simulations, in *Sensitivity to Change: Black Sea, Baltic Sea and North Sea*, edited by E. Ozsoy and A. Mikaelyan, pp. 375-394, Kluwer Academic Publishers, Boston.

Strauss, H., and T. B. Moore (1992), Abundances and isotopic compositions of carbon and sulfur species in whole rock and kerogen samples, in *The Proterozoic Biosphere*, edited by J. W. Schopf and C. Klein, pp. 709-798, Cambridge University Press, Cambridge.

Strous, M., et al. (1999), Missing lithotroph identified as new planctomycete, *Nature*, *400*(6743), 446-449.

Strous, M., and M. S. M. Jetten (2004), Anaerobic oxidation of methane and ammonium, *Annual Review of Microbiology*, *58*, 99.

Strous, M., et al. (2006), Deciphering the evolution and metabolism of an anammox bacterium from a community genome, *Nature*, *440*(7085), 790-794.

Stuiver, M., and H. A. Polach (1977), Reporting of C-14 data: Discussion, *Radiocarbon*, *19*(3), 355-363.

Suetin, V. S., et al. (2002), Analysis of the variability of the optical properties of water in the Black Sea in summer 1998 according to the data of a SeaWiFS satellite instrument *Physical Oceanography*, *12*(6), 331-340.

Suetin, V. S., et al. (2004), Manifestation of specific features of the optical properties of atmospheric aerosol over the
Black Sea in the interpretation of SeaWiFS data, *Physical Oceanography*, *14*(1), 57-65.

Sweerts, J., et al. (1990), Dentrification by sulfur oxidizing Beggiatoa spp mats on freshwater sediments, *Nature*, *344*(6268), 762-763.

Tanaka, T., and F. Rassoulzadegan (2004), Vertical and seasonal variations of bacterial abundance and production in the mesopelagic layer of the NW Mediterranean Sea: bottom-up and top-down controls, *Deep-Sea Research Part I-Oceanographic Research Papers*, *51*(4), 531-544.

Teodoru, C. R., et al. (2007), Spatial distribution and recent changes in carbon, nitrogen and phosphorus accumulation in sediments of the Black Sea, *Marine Chemistry*, *105*(1-2), 52-69.

Thamdrup, B., and T. Dalsgaard (2000), The fate of ammonium in anoxic manganese oxide-rich marine sediment, *Geochimica Et Cosmochimica Acta*, *64*(24), 4157-4164.

Thamdrup, B., et al. (2006), Anaerobic ammonium oxidation in the oxygen-deficient waters off northern Chile, *Limnology and Oceanography*, *51*(5), 2145-2156.

Thompson, A. F., et al. (2007), Spatial and temporal patterns of small-scale mixing in Drake Passage, *Journal of Physical Oceanography*, *37*(3), 572-592.

Tian, R. C. C. (2006), Toward standard parameterizations in marine biological modeling, *Ecological Modelling*, *193*(3-4), 363-386.

Tolmazin, D. (1985), Changing coastal oceanography of the Black Sea. 1. Northwestern Shelf, *Prog. Oceanogr.*, *15*(4), 217-276.

Trouwborst, R. E., et al. (2006), Soluble Mn(III) in suboxic zones, *Science*, *313*(5795), 1955-1957.

Tugrul, S., and C. Polat (1995), Quantitative comparison of the influxes of nutrients and organic carbon into the Sea of Marmara both from anthropogenic sources and from the Black Sea, *Water Science and Technology*, *32*(2), 115-121.

Turner, J. W. (1973), *Buoyancy effects in fluids*, 367 pp., Cambridge University Press, New York.

Tuttle, J. H., and H. W. Jannasch (1973), Sulfide and thiosulfate oxidizing bacteria in anoxic marine basins, *Mar. Biol.*, *20*(1), 64-70.

Tyrrell, T. (1999), The relative influences of nitrogen and phosphorus on oceanic primary production, *Nature*, *400*, 525-531.

U.S. Department of Commerce, N. O. a. A. A., National Geophysical Data Center (2006), 2-minute Gridded Global Relief Data (ETOPO2v2).

Unluata, U., et al. (1990), On the physical oceanography of the Turkish Straits, in *The Physical Oceanography of Sea Straits, NATO AS1 Ser., Ser. C*, edited by G. Pratt, pp. 25-60, Kluwer Academic, Norwell, Mass.

Van Cappellen, P., and E. D. Ingall (1994), Benthic phosphorus regeneration, net primary production, and ocean anoxia - a model of the coupled marine biogeochemical cycles of carbon and phosphorus, *Paleoceanography*, *9*(5), 677.

Van Cappellen, P., and E. D. Ingall (1996), Redox stabilization of the atmosphere and oceans by phosphorus-limited marine productivity, *Science*, *271*(5248), 493.

van de Graaf, A., et al. (1990), Anoxic ammonium oxidation,, in *Proceedings of the Fifth European Congress on Biotechnology, vol. 1*, edited by C. Christiansen, et al., pp. 388–391, Munksgaard, Copenhagen.

van de Graaf, A., et al. (1996), Autotrophic growth of anaerobic ammonium-oxidizing micro-organisms in a fluidized bed reactor, *Microbiology-(UK)*, *142*, 2187-2196.

van de Graaf, A. A., et al. (1995), Anaerobic oxidation of ammonium is a biologically mediated process, *Applied and Environmental Microbiology*, *61*(4), 1246-1251.

Visbeck, M., and M. Rhein (2000), Is bottom boundary layer mixing slowly ventilating Greenland sea deep water?, *Journal of Physical Oceanography*, *30*(1), 215-224.

Walker, S. J., et al. (2000), Reconstructed histories of the annual mean atmospheric mole fractions for the halocarbons CFC-11, CFC-12, CFC-113, and carbon tetrachloride, *Journal of Geophysical Research-Oceans*, *105*(C6), 14285-14296.

Wallmann, K. (2003), Feedbacks between oceanic redox states and marine productivity: A model perspective focused on benthic phosphorus cycling, *Global Biogeochemical Cycles*, *17*(3).

Walsh, J. J. (1991), Importance of continental margins in the marine biogeochemical cycling of carbon and nitrogen, *Nature*, *350*(6313), 53-55.

Wanninkhof, R. (1992), Relationship between wind speed and gas exchange over the ocean, *Journal of Geophysical Research-Oceans*, *97*(C5), 7373-7382.

Ward, B. B., et al. (1982), Microbial nitrification rates in the primary nitrite maximum off southern California, *Deep-Sea Research Part A-Oceanographic Research Papers*, *29*(2), 247-255.

Ward, B. B. (1987), Nitrogen transformations in the Southern California Bight, *Deep-Sea Research Part A-Oceanographic Research Papers*, *34*(5-6), 785-805.

Ward, B. B., et al. (1989), Biological nitrogen cycling in the nitracline, *Limnology and Oceanography*, *34*(3), 493-513.

Ward, B. B., and K. A. Kilpatrick (1991), Nitrogen transformations in the oxic layer of permanent anoxic basins: The Black Sea and the Cariaco Trench, in *Black Sea Oceanography*, edited by E. Izdar and J. W. Murray, pp. 111-124, Kluwer Academic Publishers, The Netherlands.

Ward, B. B. (2000), Nitrification and the marine nitrogen cycle, in *Microbial Ecology of the Oceans*, edited by D. L. Kirchman, pp. 427-453, Wiley-Liss, Inc., New York.

Watson, A. J., et al. (1999), Mixing and convection in the Greenland Sea from a tracer-release experiment, *Nature*, *401*(6756), 902-904.

Weber, A., et al. (2001), Sulfate reduction in Black Sea sediments: in situ and laboratory radiotracer measurements from the shelf to 2000m depth, *Deep-Sea Research Part I-Oceanographic Research Papers*, *48*(9), 2073-2096.

Weiss, R. F. (1970), Solubility of nitrogen, oxygen and argon in water and seawater, *Deep-Sea Research*, *17*(4), 721-&.

Weiss, R. F., and B. A. Price (1980), Nitrous oxide solubility in water and seawater, *Marine Chemistry*, *8*(4), 347-359.

Wheat, C. G., et al. (1996), Phosphate removal by oceanic hydrothermal processes: An update of the phosphorus budget in the oceans, *Geochimica Et Cosmochimica Acta*, *60*(19), 3593-3608.

Winguth, A. M. E., and E. Maier-Reimer (2005), Causes of the marine productivity and oxygen changes associated with the Permian-Triassic boundary: A reevaluation with ocean general circulation models, *Marine Geology*, *217*(3-4), 283-304.

Wuchter, C., et al. (2006), Archaeal nitrification in the ocean, *Proceedings of the National Academy of Sciences of the United States of America*, *103*(33), 12317-12322.

Wunsch, C., and R. Ferrari (2004), Vertical mixing, energy and the general circulation of the oceans, *Annual Review of Fluid Mechanics*, *36*, 281.

Wyrtki, K. (1963), The horizontal and vertical field of motion in the Peru Current, *Bulletin Scripps Institution of Oceanography*, *8*(4), 313-346.

Wyrtki, K. (1981), An estimate of equatorial upwelling in the Pacific, *Journal of Physical Oceanography*, *11*(9), 1205-1214.

Yakushev, E. V., et al. (2007), Analysis of the water column oxic/anoxic interface in the Black and Baltic seas with a numerical model, *Marine Chemistry*, *107*(3), 388-410.

Yang, W., et al. (2005), Anoxic sulfide oxidation in wastewater of sewer networks, *Water Science and Technology*, *52*(3), 191-199.

Yemenicioglu, S., et al. (2006), Distribution of dissolved forms of iron and manganese in the Black Sea, *Deep-Sea Research Part Ii-Topical Studies in Oceanography*, *53*(17-19), 1842-1855.

Yilmaz, A., et al. (1998), On the production, elemental composition (C, N, P) and distribution of photosynthetic organic matter in the Southern Black Sea, *Hydrobiologia*, *363*, 141-156.

Yilmaz, A., et al. (2006), Surface and mid-water sources of organic carbon by photoautotrophic and chemoautotrophic production in the Black Sea, *Deep-Sea Research Part Ii-Topical Studies in Oceanography*, *53*(17-19), 1988-2004.

Yunev, O. A., et al. (2002), Long-term variations of surface chlorophyll a and primary production in the open Black Sea, *Marine Ecology-Progress Series*, *230*, 11-28.

Yunev, O. A., et al. (2007), Nutrient and phytoplankton trends on the western Black Sea shelf in response to cultural eutrophication and climate changes, *Estuar. Coast. Shelf Sci.*, *74*(1-2), 63-76.

Zhang, D. X., et al. (2003), Observational evidence for flow between the subtropical and tropical Atlantic: The Atlantic subtropical cells, *Journal of Physical Oceanography*, *33*(8), 1783-1797.

Zumft, W. G. (1997), Cell biology and molecular basis of denitrification, *Microbiol. Mol. Biol. Rev.*, *61*(4), 533-616.